

# Planetary-Scale Shear Trajectories and Their Expression in Global Geological Geometry

Craig Stone

26 December 2025

## Plain Language Summary

Many large geological features on Earth—such as sweeping mountain arcs, curved continental margins, rift systems, ocean-floor ridges, and sedimentary belts—share recurring geometric patterns that appear across regional, continental, and sometimes near-hemispheric scales. These features are normally interpreted in terms of local processes such as plate convergence, mantle flow, erosion, or rifting. In this study, we ask a broader question: whether some aspects of this large-scale curvature and directional organisation may also reflect an underlying, planet-scale stress framework that interacts with—but does not replace—conventional tectonic processes.

To explore this idea, we compare observed stress orientations from the World Stress Map with a mathematically defined global shear field derived from an idealised, true-polar-wander-like rotational geometry. Rather than asking only whether the model reduces global average misfit between predicted and observed stress directions, we examine whether the *pattern* of agreement and disagreement is spatially organised in a meaningful way.

Using permutation-based spatial statistics, we find that misfit values are not randomly distributed. Instead, they form coherent geographic clusters across multiple spatial scales, from regional domains hundreds of kilometres across to broad, near-hemispheric regions spanning several thousand kilometres. This organisation persists even though the model does not outperform randomly rotated alternatives in terms of global mean misfit. The result shows that spatial organisation and global alignment are distinct diagnostic signals, and that a model may capture physically meaningful structure even when it does not minimise average misfit.

We also show that the same shear geometry is expressed qualitatively in a wide range of geological and geomorphic settings, including passive-margin sediment belts, arcuate mountain systems, curved rift segments, ocean-floor bathymetric arcs, and glacially sculpted landscapes. These expressions occur across different tectonic regimes and geological ages, suggesting that local processes may operate within, and be subtly conditioned by, a longer-wavelength stress architecture.

A key limitation of this study is that demonstrating spatial organisation is easier than demonstrating its cause. The results do not prove that true polar wander—or any specific mechanism—is

responsible for the observed patterns. Instead, they support a more cautious interpretation: that a global-scale shear framework produces testable geometric signals that are detectable in present-day stress orientations and in the long-term curvature of major geological features. In this sense, the work should be viewed as a hypothesis-driven investigation rather than a causal reconstruction.

Overall, the findings suggest that regional tectonics and plate processes do not operate in isolation, but may be influenced by a persistent, planet-scale stress topology that shapes where and how large-scale curvature develops. Later sections of the paper outline how this hypothesis can be tested further using independent datasets, alternative stress models, and additional quantitative metrics.

### Abstract

Large arcuate geological features occur across Earth’s surface in sedimentary, tectonic, glacial, and oceanic environments. Most examples are interpreted primarily in terms of local or regional processes such as plate convergence, rifting, mantle flow, or differential erosion. However, the recurrence of smooth, large-radius curvature across contrasting geological provinces raises the question of whether some aspects of Earth’s surface geometry may also reflect an underlying, long-wavelength stress organisation that interacts with—but does not replace—conventional tectonic mechanisms.

In this study, we compare global geological and geophysical patterns with an analytically derived surface shear field associated with a prescribed class of true-polar-wander-like rotational geometries. Using a Vening Meinesz-style formulation, two conjugate families of shear trajectories (Net 1 and Net 2), together with invariant contours, are computed analytically on the sphere without tuning to observations. These trajectories are then evaluated against present-day stress orientations from the World Stress Map (WSM) and against the large-scale curvature of geological and geomorphic features.

Quantitative comparison shows that, although the modeled shear field does not outperform randomly rotated Euler-field ensembles in terms of global mean angular misfit, the spatial distribution of misfit exhibits statistically robust, scale-dependent geographic organisation. Permutation-based spatial autocorrelation analysis yields consistently positive and highly significant Moran’s  $I$  values from regional ( $\sim 250$  km) through continental to near-hemispheric ( $\sim 3000$ – $4000$  km) scales, with smoothly decreasing magnitude at increasing wavelength. This demonstrates that spatial organisation and global alignment constitute distinct diagnostic signals, and that physically meaningful structure can be present even when average misfit metrics remain non-diagnostic.

Qualitative comparison further shows recurring geometric congruence between the modeled shear trajectories and a wide range of Earth-surface features, including passive-margin sediment belts, arcuate orogenic systems, rift curvature, oceanic bathymetric arcs, and glacially sculpted landscapes. These correspondences persist across differing tectonic settings and geological ages, suggesting that regional processes may operate within a persistent, long-wavelength stress framework.

A key limitation of this work is that demonstrating spatial organisation is inherently easier than demonstrating causation. The results do not establish a unique physical mechanism for



the inferred shear topology, nor do they imply that true polar wander is the sole or necessary driver. Rather, they support the interpretation that a global-scale shear framework produces testable geometric and statistical signals that warrant further investigation.

Taken together, the results indicate that Earth's deformation and surface geometry may be influenced by a persistent, planet-scale stress topology that interacts with, and subtly conditions, plate-tectonic and regional geological processes. The framework developed here provides a basis for future tests using independent datasets, alternative stress models, and forward geodynamic simulations.

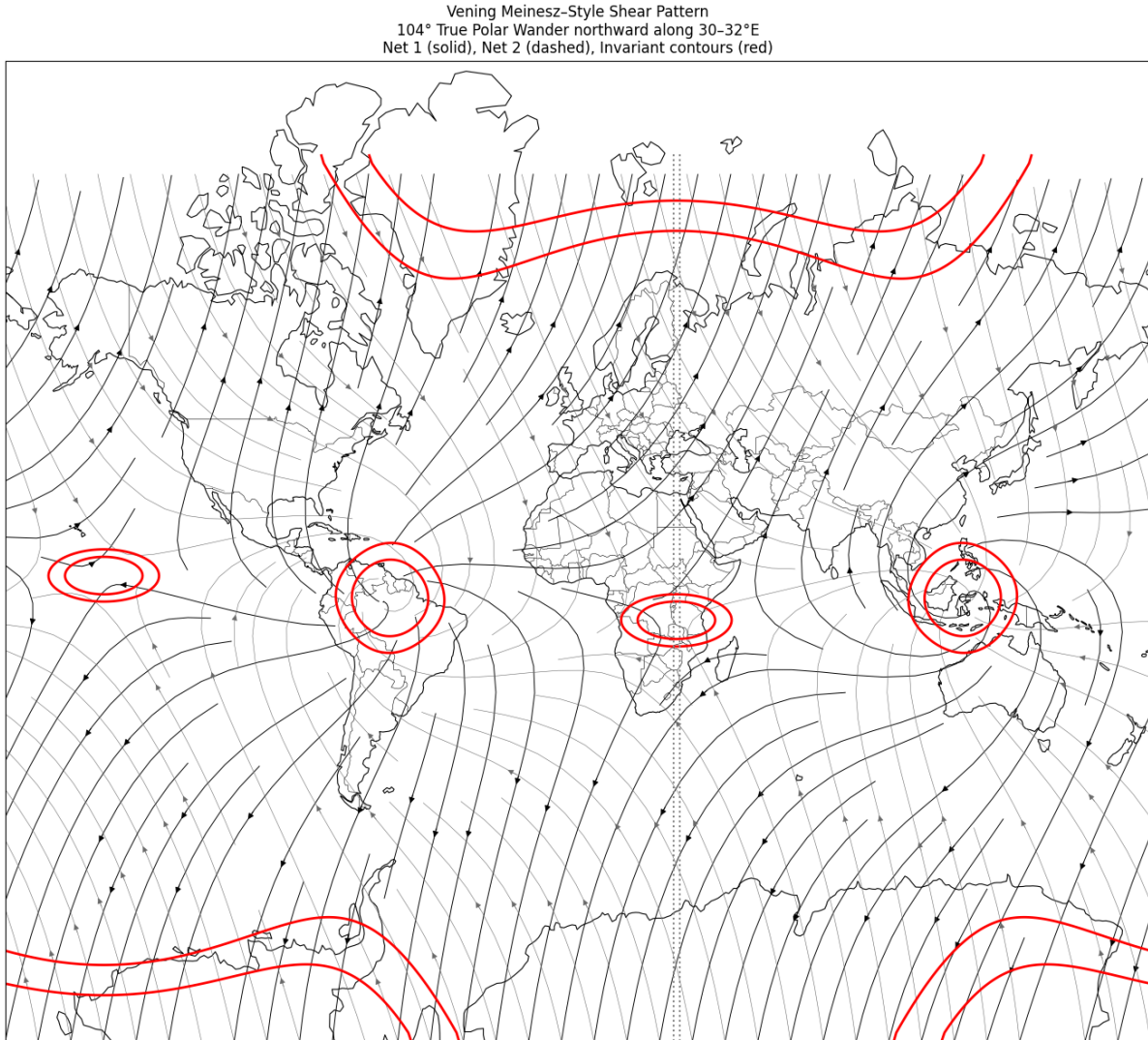


Figure 1: Vening Meinesz-style global shear pattern for a prescribed 104° northward true polar wander along the 31°E meridian. Solid curves indicate Net 1 shear trajectories, dashed curves Net 2 trajectories, and red curves invariant contours.

# 1 Introduction

Earth’s lithosphere exhibits pervasive curvature at regional, continental, and planetary scales. Arcuate sedimentary belts, sweeping mountain chains, curved passive margins, bathymetric arcs, rift systems, and coherent basin chains occur across diverse tectonic environments and geological ages. These features are conventionally interpreted in terms of local or regional boundary conditions, including plate convergence, rift propagation, mantle flow, differential erosion, and structural inheritance (e.g. Zoback, 1992; Heidbach et al., 2018; Stephan, 2023). While such processes explain many aspects of individual systems, some of the largest arcuate structures cross multiple geological provinces and persist across contrasting lithospheric ages, exhibiting smooth, large-radius curvature that is not always readily reconciled with short-wavelength forcing or segmented tectonic histories.

These observations motivate a broader question: whether certain aspects of Earth’s surface geometry and stress orientation may also reflect long-wavelength, planet-scale stress organisation that interacts with—but does not replace—plate-tectonic and regional processes. Previous studies have characterised large-scale coherence in observed stress orientations and have compared numerical or geodynamic stress models to the World Stress Map (WSM) primarily using scalar misfit metrics or regional smoothing approaches (e.g. Heidbach et al., 2018; Cao et al., 2021; Stephan, 2023). However, relatively little work has examined whether the *geographic organisation* of misfit between a prescribed global stress geometry and observed stress orientations contains additional diagnostic information beyond global mean alignment.

The present study evaluates whether a mathematically prescribed global shear field, derived from a simple class of true-polar-wander-like (TPW-like) rotational geometries, exhibits meaningful correspondence with both observed stress orientations and the recurring curvature of large-scale geological and geomorphic features. The approach does not attempt to reconstruct a specific geodynamic mechanism or geological event. Instead, it treats the shear topology as a *geometric hypothesis* and asks whether its predicted structure is detectable in (i) the spatial organisation of stress-orientation misfit and (ii) the geometry of large-scale surface curvature.

A central methodological distinction in this work is the separation of two diagnostic questions. First, we assess whether the modeled shear field reduces global mean angular misfit relative to randomly rotated reference fields. Second—and more critically—we evaluate whether the geographic distribution of misfit values is spatially organised rather than randomly dispersed. These quantities diagnose different aspects of model behaviour: a geometry may fail to minimise global misfit yet still express coherent long-wavelength spatial structure. Distinguishing between global alignment and spatial organisation is therefore essential for correct interpretation (cf. Stephan, 2023; Cao et al., 2021).

To address these questions, we compute analytically derived shear trajectories and invariant contours on the sphere using a Vening Meinesz-style kinematic formulation and compare these trajectories with observed stress orientations from the WSM (Heidbach et al., 2018). Spatial

organisation is evaluated using permutation-based Moran’s  $I$  statistics across multiple spatial scales, in parallel with Euler-rotation null ensembles that preserve internal geometry while removing Earth-fixed alignment. Expanded mathematical development of the shear-field computation and statistical testing workflow is presented in Section 2.

## 2 Methods

### 2.1 Methodological Context

The objective of this study is to test whether a mathematically prescribed, planet-scale shear topology produces spatially organised correspondence with independently observed stress orientations and large-scale geological curvature. Prior work has documented regional to continental organisation in the observed stress field and has evaluated numerical or geodynamic stress models against the WSM using scalar misfit metrics, smoothing radii, or regional averaging approaches (e.g. Zoback, 1992; Heidbach et al., 2018; Cao et al., 2021; Stephan, 2023). The present approach extends this literature by (i) deriving an analytically closed-form global shear field on the sphere and (ii) explicitly evaluating the *spatial organisation* of the resulting misfit field using permutation-based Moran’s  $I$  across multiple wavelengths, interpreted jointly with Euler-rotation null ensembles.

### 2.2 Rotation Geometry

The shear field is derived from a rigid-body reorientation of the lithosphere through a prescribed TPW-like rotation of magnitude  $\Theta = 104^\circ$  about an axis along the  $31^\circ\text{E}$  meridian. The transformation is purely geometric and Earth-fixed; no assumptions are made regarding the timing, forcing, or physical plausibility of the rotation pathway. The Euler-pole formulation follows standard spherical kinematics (e.g. Turcotte and Schubert, 2014, and the rotation operator is written

$$\mathbf{x}' = \mathbf{R}(\hat{\mathbf{p}}, \Theta) \mathbf{x}, \quad (1)$$

where  $\hat{\mathbf{p}}$  is the unit vector normal to the rotation axis.

### 2.3 Kinematic Shear Formulation

Following a Vening Meinesz-style treatment of rotational strain on the sphere (e.g. ??, surface points are embedded as unit vectors  $\mathbf{x}$  on  $S^2$ . The angular velocity vector

$$\boldsymbol{\Omega} = \dot{\Theta} \hat{\mathbf{p}} \quad (2)$$

induces the surface velocity field

$$\mathbf{v}(\mathbf{x}) = \boldsymbol{\Omega} \times \mathbf{x}. \quad (3)$$

The velocity gradient is decomposed into symmetric and antisymmetric components,

$$\nabla \mathbf{v} = \mathbf{E} + \mathbf{W}, \quad (4)$$

where  $\mathbf{E}$  defines the local strain-rate tensor. Its eigenvectors  $\mathbf{e}_1, \mathbf{e}_2$  define the orthogonal conjugate shear directions (*Net 1* and *Net 2*), and the magnitude of differential shear is

$$\Delta\sigma = |\lambda_1 - \lambda_2|. \quad (5)$$

## 2.4 Trajectory Integration and Invariant Contours

Shear trajectories are computed as integral curves of the principal-direction fields,

$$\frac{d\mathbf{x}}{ds} = \mathbf{e}_i(\mathbf{x}), \quad i \in \{1, 2\}, \quad (6)$$

subject to  $\|\mathbf{x}\| = 1$ . Invariant contours are defined as loci of locally minimal differential shear (cf. ?). All fields are generated analytically from the prescribed geometry without tuning to geological observations.

## 2.5 Observed Stress Data and Misfit Computation

Observed stress orientations are taken from the 2025 World Stress Map database (Heidbach et al., 2018), using standard quality weighting and axial (180°-periodic) orientation treatment. Misfit is defined as

$$\delta = \min(|\alpha_{\text{model}} - \alpha_{\text{obs}}|, 90^\circ - |\alpha_{\text{model}} - \alpha_{\text{obs}}|), \quad (7)$$

with the better-fitting of Net 1 / Net 2 retained at each site.

## 2.6 Statistical Testing Framework

Two complementary statistical tests are applied.

**Global-Mean Alignment (Euler-Rotation Null).** Random Euler rotations preserve internal geometry while destroying Earth-fixed alignment; the observed global mean misfit is compared against the empirical null distribution (approach consistent with Cao et al., 2021).

**Spatial Organisation (Permutation Moran’s  $I$ ).** Angular misfit values are permuted among observation locations while preserving sampling geometry and distribution, and Moran’s  $I$  is computed across 250–4000 km neighbourhoods following standard spatial-statistics practice (e.g. Cliff and Ord, 1981. This test evaluates whether misfit values exhibit significant geographic clustering independent of global-mean alignment.

## 2.7 Scale Definitions

Spatial scales are reported using the following conventions: regional ( $\sim 250$ – $500$  km), continental to transcontinental ( $\sim 500$ – $1500$  km), and planetary to near-hemispheric ( $\sim 1500$ – $4000$  km). “Spatial organisation” refers specifically to statistically resolvable geographic structure in the misfit field as quantified by Moran’s  $I$ ; “global alignment” denotes scalar reductions in mean angular misfit.

## 3 Results: Regional Case Studies

The following case studies illustrate how the modeled shear framework is expressed across contrasting tectonic, geomorphic, and depositional environments. In each example, geometric correspondence is evaluated in terms of (i) alignment with Net 1 and Net 2 shear trajectories or invariant contours, (ii) independence from purely local boundary conditions, and (iii) coherence across scale transitions. These regional observations complement the quantitative spatial-statistical results and provide contextual evidence for a persistent, long-wavelength shear topology that interacts with, rather than replaces, plate-tectonic and surface processes.

### 3.1 Southeastern United States Sediment Arc

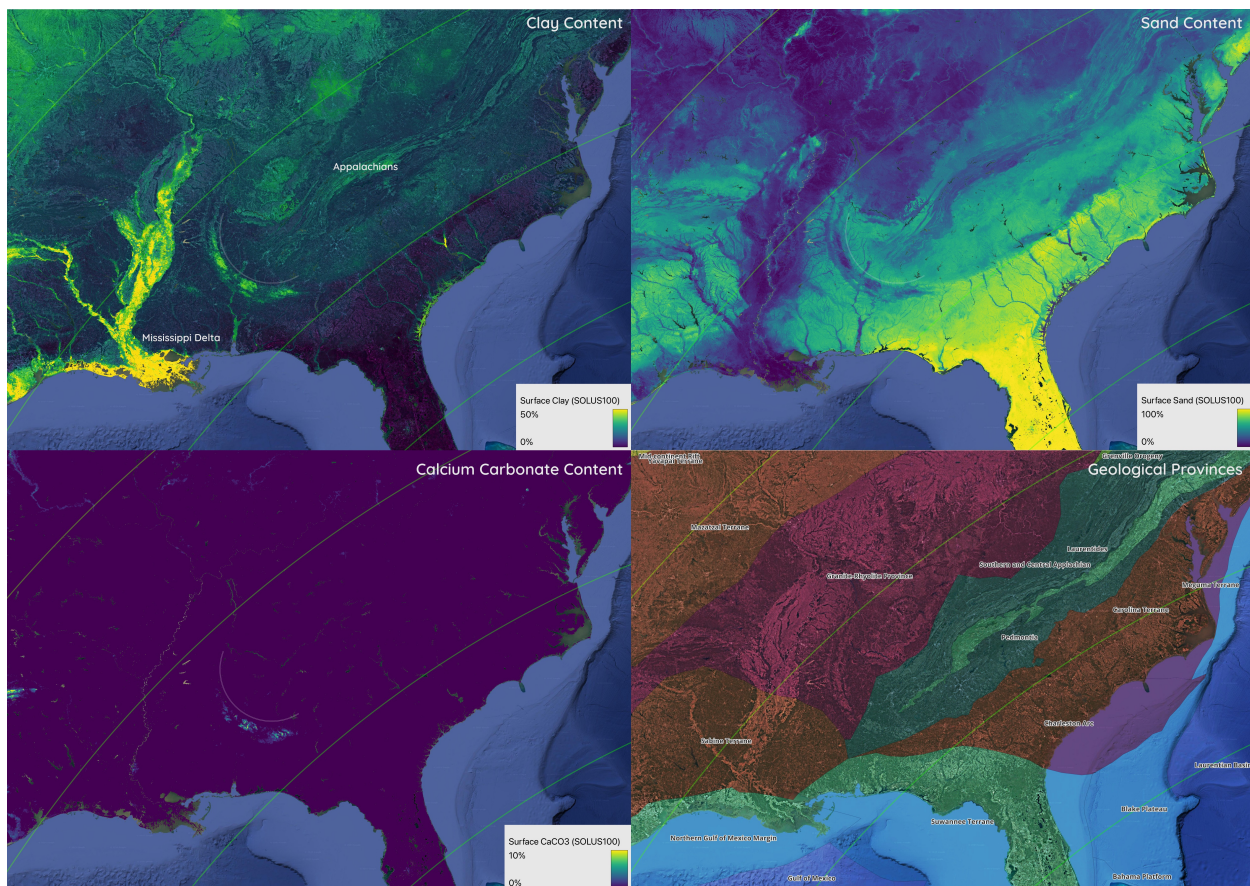


Figure 2: Four-panel comparison of clay,  $\text{CaCO}_3$ , sand, and geological provinces in the southeastern United States. A continent-scale arcuate belt aligns with invariant shear contours and crosses multiple geological provinces.

The arcuate sedimentary belt spanning the southeastern United States (Figure 2) represents one of the clearest expressions of the modeled global shear framework acting within a passive-margin setting. Conventional interpretations emphasise Appalachian orogenic inheritance, differential erosion, fluvial routing, and marine sediment redistribution. While these processes are important contributors, they do not readily explain the remarkable geometric continuity, large radius of curvature, and cross-provincial coherence of the arc across multiple sediment classes and lithospheric domains.

When examined in the context of the modeled shear field, the sediment arc aligns closely with invariant shear contours rather than with present-day drainage basins, coastline geometry, or individual tectonostratigraphic boundaries. The arc persists across terranes of differing lithology and age, including Paleozoic orogenic belts, Mesozoic rifted margins, and Cenozoic sedimentary platforms, indicating control by a stress geometry that transcends local structural segmentation.

Notably, the correspondence is expressed simultaneously in clay-rich sediments, carbonate dis-

tributions, and sandy deposits, each characterised by distinct transport pathways and depositional mechanisms. The convergence of these independent sedimentary signals along the same arcuate trajectory argues against coincidental alignment and instead points to a shared, long-wavelength controlling framework. Within the shear-net interpretation, the arc occupies a zone of minimal differential shear, a setting expected to favour long-term sediment accumulation and curvature stability while suppressing disruptive deformation.

Through repeated episodes of erosion, sea-level fluctuation, and sediment reworking, this inherited stress architecture appears to have been progressively amplified rather than erased. The southeastern sediment arc therefore functions as a geomorphic and sedimentological recorder of the broader shear topology, consistent with the cross-scale organisational behaviour demonstrated statistically in Section 6.

This interpretation does not displace established Appalachian or passive-margin models; instead, it situates them within a hierarchical framework in which local processes operate within, and are subtly conditioned by, a persistent planet-scale stress organization. In this sense, the southeastern United States sediment arc is not an isolated regional anomaly, but a continental-scale manifestation of the same shear geometry expressed in other tectonic and depositional systems worldwide.



### 3.2 The Himalayan Arc

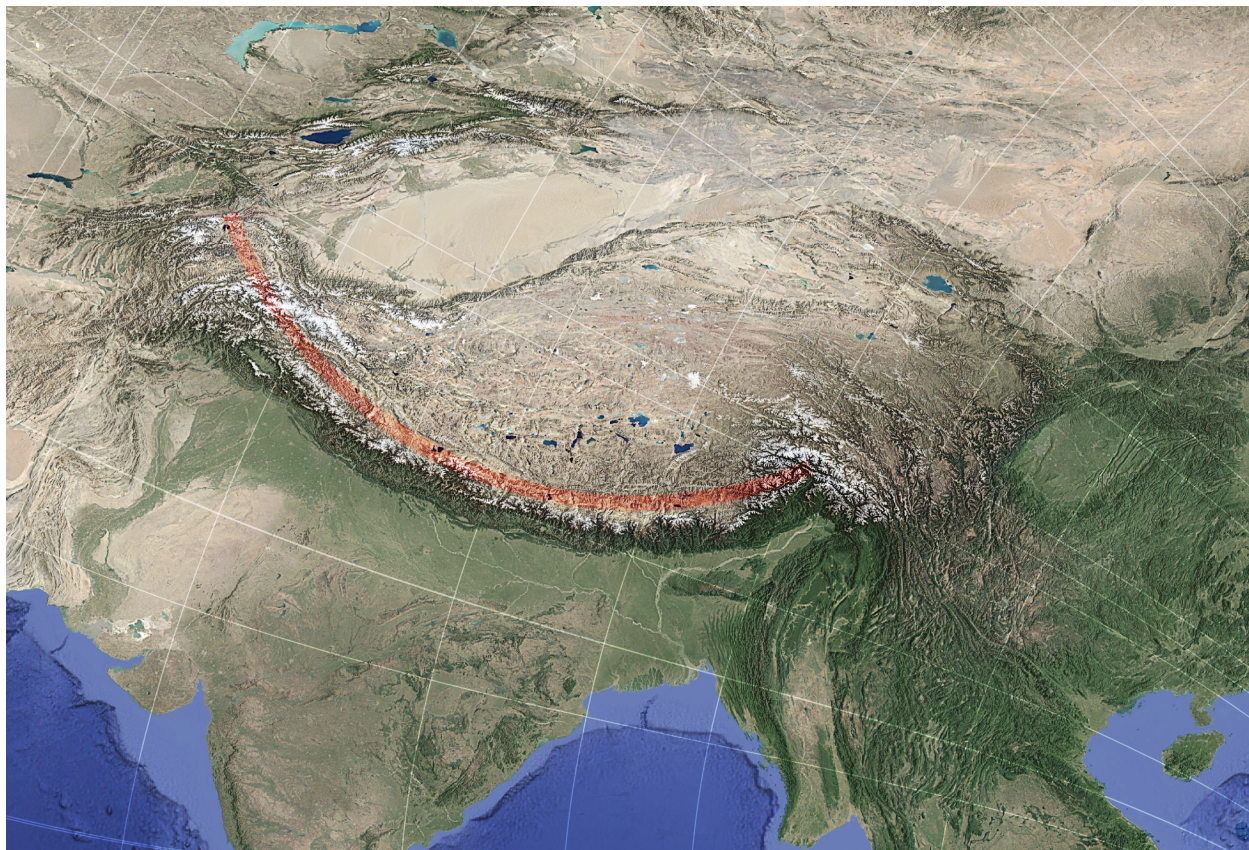


Figure 3: The Himalayan mountain belt forms a geometrically smooth arc that lies parallel to one shear family and orthogonal to the conjugate family.

The Himalayan mountain belt is widely interpreted as the product of continent–continent collision between India and Eurasia, leading to crustal shortening, uplift, and thrust-belt development (e.g. ??). This tectonic framework explains the kinematics and deformation style of the orogen, but it does not, by itself, account for the remarkable geometric regularity and large-radius curvature of the Himalayan arc over more than 2500 km.

Within the modeled global shear framework, the Himalayan arc lies within a transition zone where the two conjugate shear families rotate smoothly along strike. The arc exhibits near-orthogonality to one family and approximate parallelism to the other, producing a mechanically coherent curvature geometry. In such a configuration, collision-driven shortening is predisposed to organise into laterally continuous curvature rather than into segmented salients or irregular thrust corridors, consistent with observations of arc-scale continuity in major Himalayan structures (e.g. ?).

This interpretation does not replace plate-tectonic explanations for Himalayan evolution. Instead, it frames the arc as a case in which strong collisional forcing operates within a long-wavelength



geometric environment that biases curvature development. The behaviour is consistent with the broader pattern observed across other arcuate systems in this study, in which large-radius curvature aligns with regions of predicted shear stability while remaining dependent on local tectonic drivers.

### 3.3 The Caribbean Plate Margin and Intra-Arc Curvature

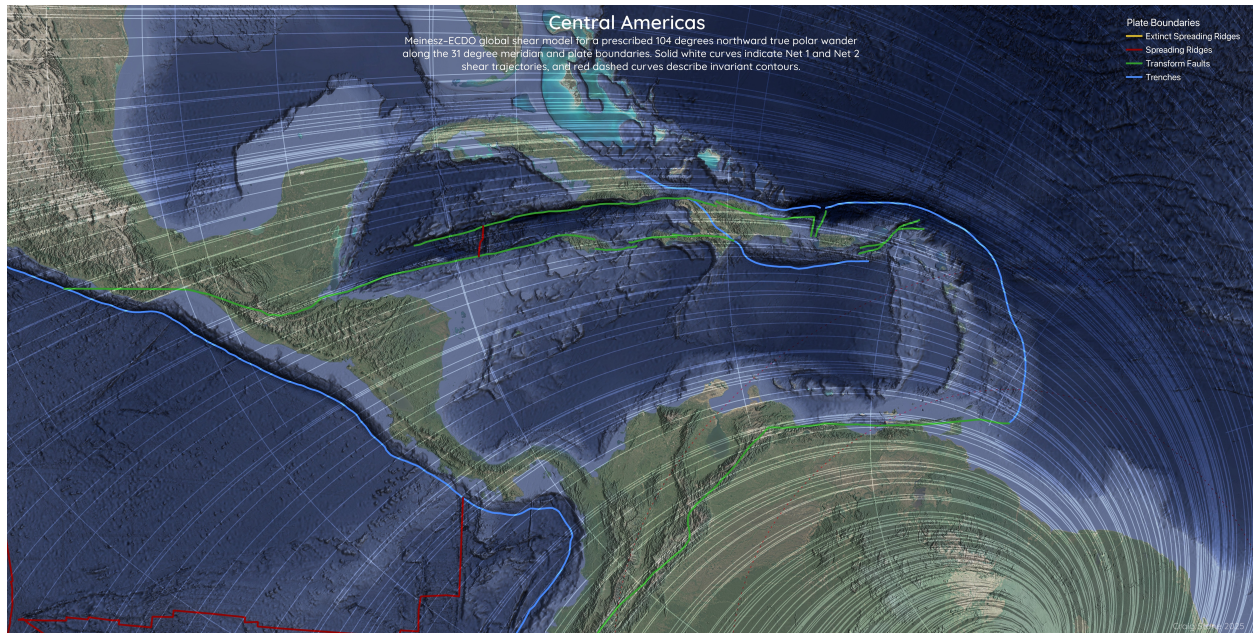


Figure 4: Central America and the Caribbean showing strong geometric congruence between plate boundaries and the modeled global shear field.

The Caribbean region is shaped by a combination of subduction, strike-slip motion, slab fragmentation, and arc-continent interaction along the boundaries of the Caribbean Plate (e.g. ??). Arc geometry and forearc curvature vary along strike, reflecting regional changes in plate coupling, trench kinematics, and crustal inheritance (Rosencrantz et al., 1990).

Within the modeled shear framework, several major Caribbean arc segments occupy domains where one shear family remains locally stable over 1000–1500 km while the conjugate family rotates across the plate margin. Curved forearc and intra-arc basins develop preferentially in regions where shear trajectories converge or change orientation gradually rather than abruptly. In contrast, highly oblique or transform-dominated sectors coincide with domains of rapidly rotating shear geometry and correspondingly larger stress-orientation misfit.

This behaviour is interpreted as consistent with the idea that plate-boundary deformation is primarily controlled by subduction and strike-slip processes, while the long-wavelength shear topology influences the geometric form through which curvature and segmentation are expressed along the margin.

### 3.4 South Indian Ocean Tectonic Arc

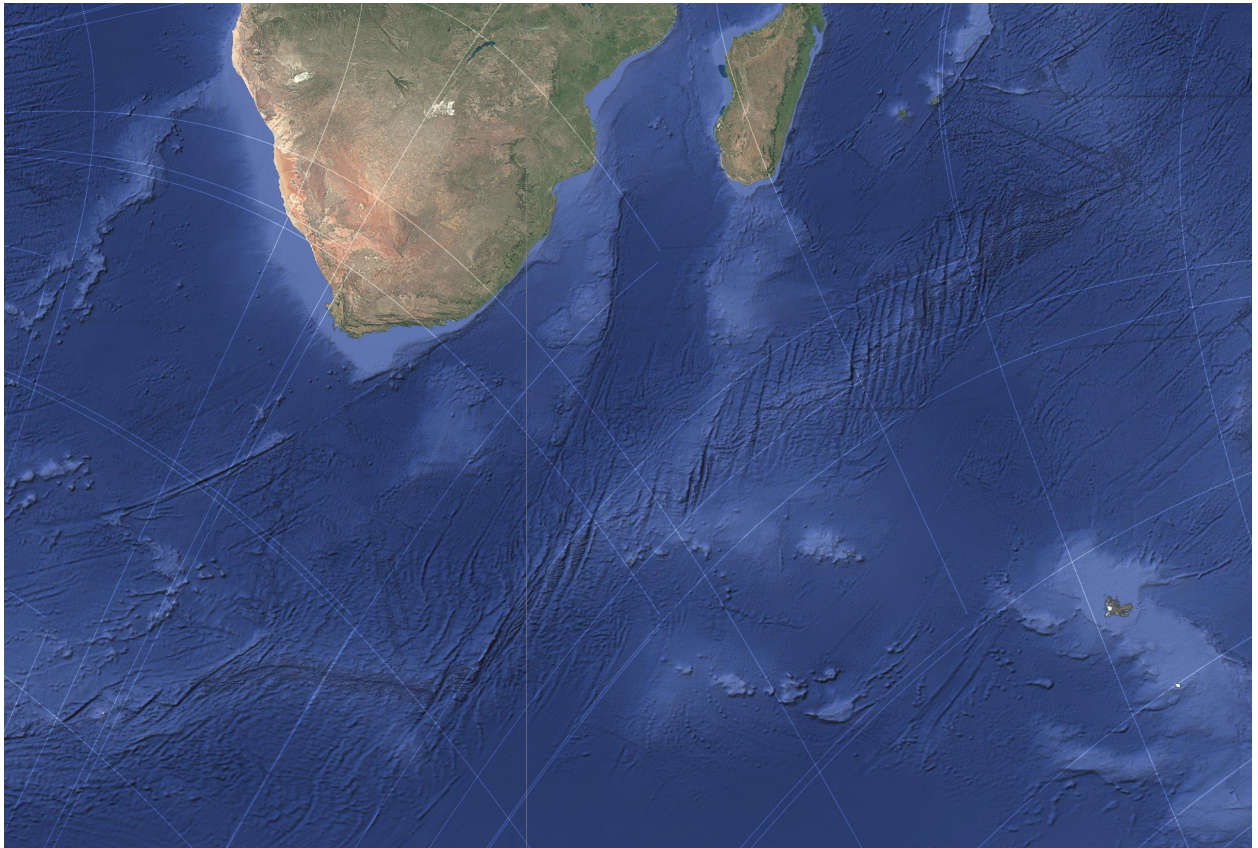


Figure 5: A vast tectonic arc in the southern Indian Ocean displaying strong congruence with modeled shear trajectories.

The southern Indian Ocean hosts one of the least discussed yet most geometrically coherent arcuate tectonic features identified in this study. Extending across abyssal plains and intersecting multiple spreading systems, the arc is commonly attributed to combinations of ridge propagation, transform segmentation, and inherited mantle structure. While these processes contribute to its development, they do not, on their own, account for the smooth, large-radius curvature and persistence of the feature across regions with markedly different spreading histories.

Within the modeled global shear framework, the South Indian Ocean arc aligns closely with invariant shear contours, occupying a domain of minimal differential shear under the prescribed rotational geometry. This alignment is particularly significant because oceanic lithosphere is continuously generated. The preservation of coherent curvature in such a setting implies that the organizing stress geometry is both long-wavelength and repeatedly imposed through successive episodes of lithospheric accretion.

Bathymetric and gravity data indicate that ridge segments, fracture zones, and subtle topographic highs preferentially conform to the modeled curvature rather than to local spreading directions alone. In several regions, ridge axes rotate smoothly to remain approximately orthogonal

to nearby shear trajectories, while transform offsets tend to align parallel to one of the two shear families. This behaviour mirrors that observed along the Mid-Atlantic Ridge and supports the interpretation that ridge segmentation and propagation are biased by an externally imposed shear topology rather than emerging solely from local kinematic constraints.

The diagnostic value of this feature lies in its predominantly oceanic context, largely free from continental inheritance. Its morphology must therefore arise from interactions among mantle flow, lithospheric accretion, and a persistent, planet-scale stress organization. In this setting, the global shear field provides a parsimonious explanation for the spatial coherence of ridge initiation, abandonment, and segmentation through time.

Even as spreading centres migrate and plate configurations evolve, the invariant shear geometry remains fixed relative to the global frame, enabling successive generations of oceanic crust to inherit similar curvature. The resulting composite bathymetric signature integrates the cumulative effect of long-wavelength shear organisation over tens of millions of years—behaviour that is consistent with the scale-persistent spatial structure demonstrated statistically in Section 6.

In summary, the South Indian Ocean tectonic arc represents a compelling oceanic manifestation of the global shear framework. Its correspondence with invariant contours strengthens the inference that the modeled shear field reflects a real and long-lived component of Earth’s stress architecture, influencing both continental and oceanic tectonics across multiple spatial and temporal scales.



### 3.5 The Banda–Sulawesi Arc System

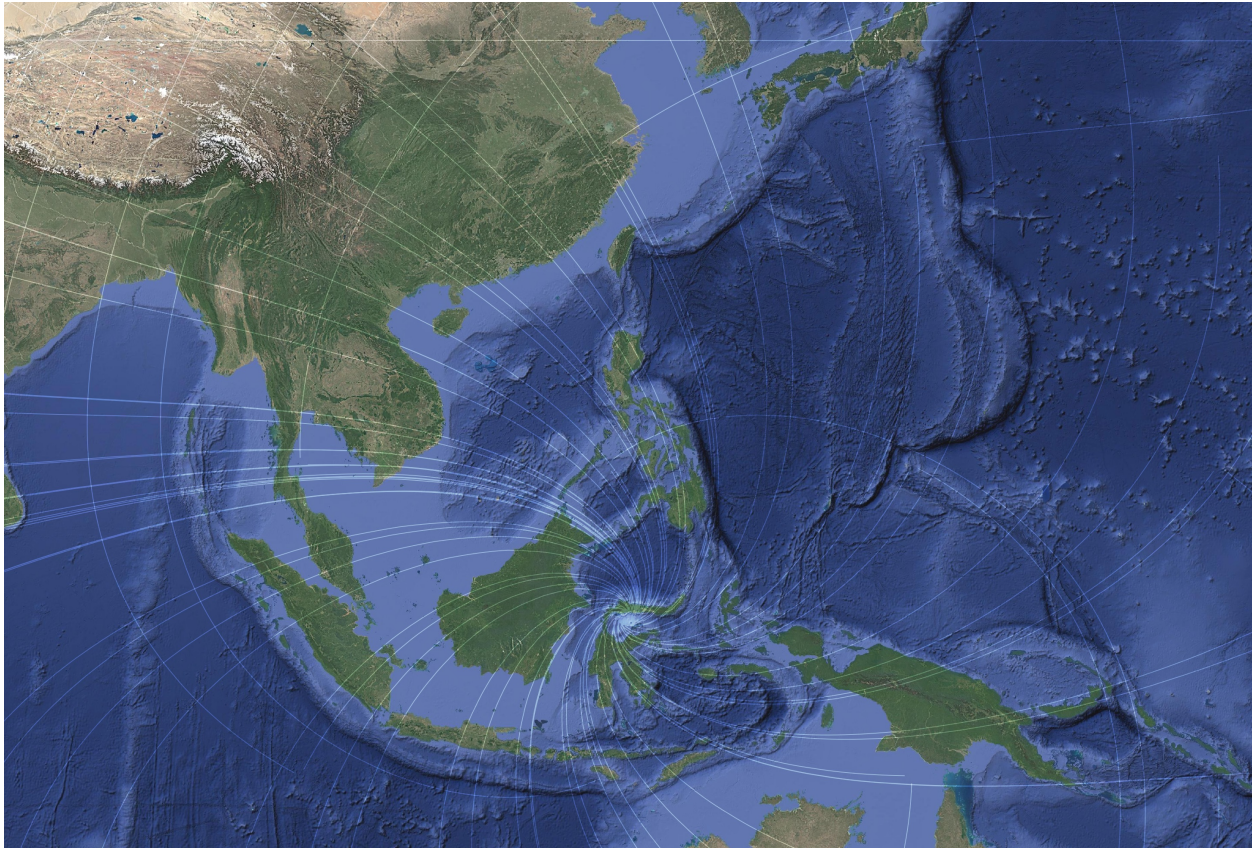


Figure 6: Primary and secondary bathymetric arcs near Sulawesi aligned with predicted shear trajectories.

The Banda–Sulawesi region is characterised by complex arc–continent collision, microplate rotation, slab roll-back, and highly curved orogenic belts (e.g. Hamilton, 1979; Hall, 2012). Numerous studies attribute arcuate geometry in this region to progressive rotation of lithospheric blocks and trench-rollback processes in a convergent–collisional setting (Hall, 2012).

In the context of the modeled shear field, the Banda Arc occupies a domain in which the two shear families rotate through nearly orthogonal orientations over relatively short distances. The arc follows a curvature envelope that remains close to one of the shear trajectories, while lateral structural terminations approach invariant-contour zones associated with low differential shear. This configuration is consistent with the persistence of sweeping arc curvature through multiple stages of collision and rotation.

The present interpretation does not replace rotation-based or rollback-driven models of Banda evolution. Instead, it suggests that the persistence and smoothness of the arc geometry may be favoured where long-wavelength shear trajectories provide a kinematic pathway that supports sustained curvature development during otherwise complex plate interactions.

### 3.6 Mid-Atlantic Ridge

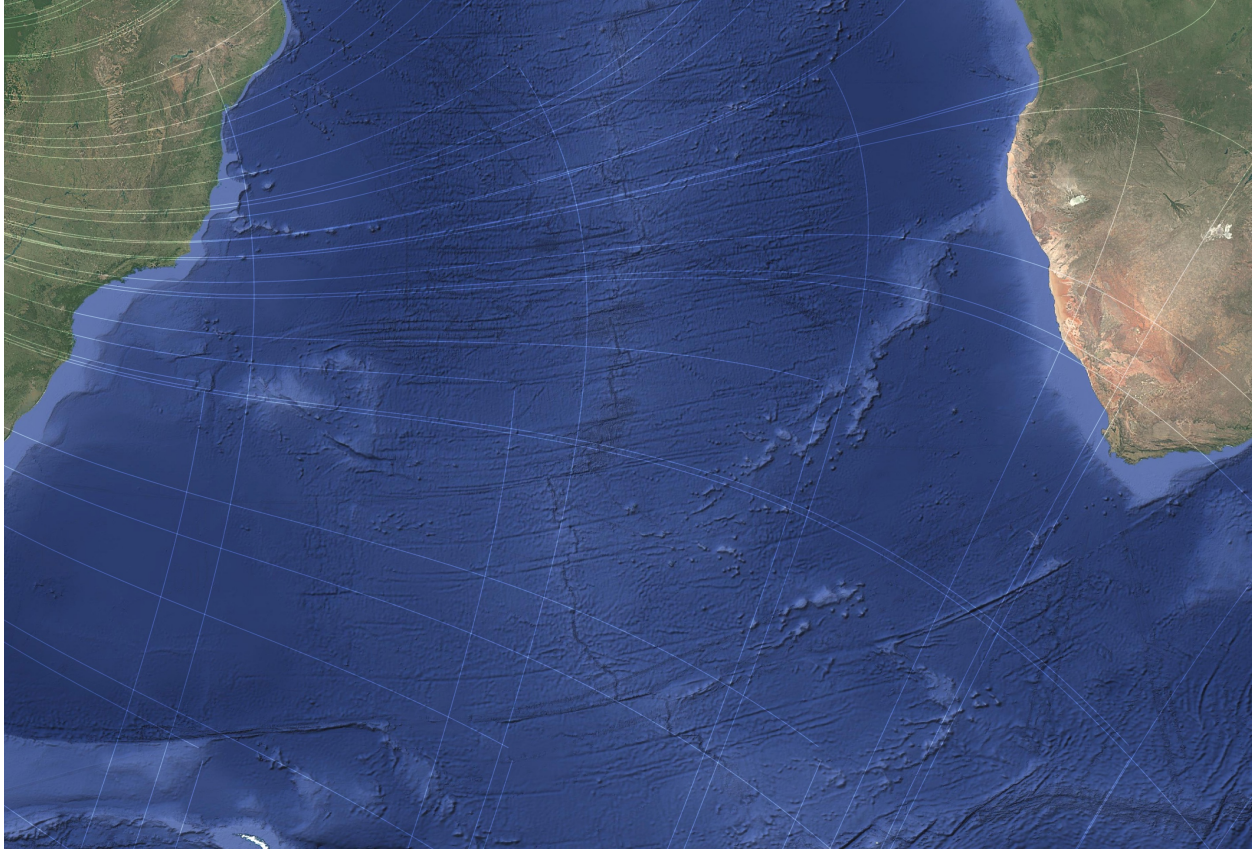


Figure 7: The Mid-Atlantic Ridge exhibits alternating alignment with Net 1 and Net 2 shear families along strike.

The morphology of the Mid-Atlantic Ridge (MAR) reflects the interaction of plate divergence, mantle upwelling, and transform segmentation (e.g. Macdonald, 1984; Parsons and Sclater, 1977). Along-strike alternation in ridge-segment orientation and curvature has been attributed to variations in spreading kinematics and thermal structure (?).

When viewed in the context of the modeled shear framework, MAR segments exhibit recurring alternation between orientations approximately orthogonal to one shear family and parallel to the conjugate family. This pattern is expressed at multiple wavelengths and persists across both hemispheres. The correspondence is interpreted not as evidence that the shear field controls ridge dynamics, but as an indication that spreading-related segmentation may preferentially exploit orientations that are geometrically consistent with a long-wavelength stress topology.

This behaviour parallels that observed in several continental rift systems, where rift curvature and segmentation occur preferentially within predicted shear-trajectory domains. In both cases, local geodynamic processes remain primary, while the modeled shear geometry appears to bias the form through which segmentation is expressed.



### 3.7 North American Intracontinental Basins and Lake Systems

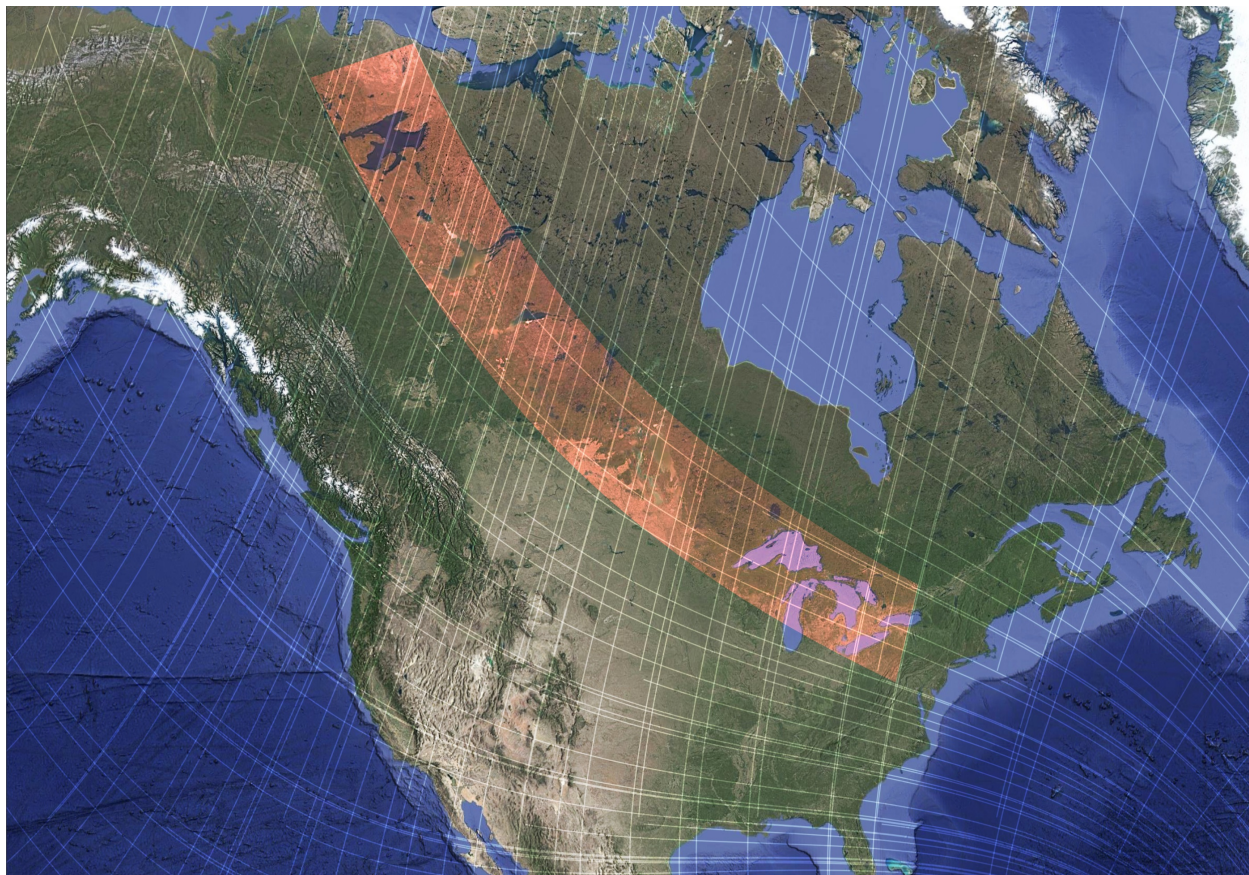


Figure 8: A continental-scale arc of large lakes across North America aligned with invariant shear contours.

Several large intracontinental basins and lake systems of North America, including the Hudson Bay depression, the Great Lakes region, and adjacent basin chains, have histories linked to lithospheric flexure, glacial loading and unloading, sedimentary subsidence, and inherited structural fabrics (e.g. Andrews and Peltier, 1970; ?). These processes explain basin formation mechanisms, but the large-radius curvature and directional coherence of basin chains extend beyond individual structural blocks.

When evaluated against the modeled shear framework, basin margins and lake basins display preferential alignment with one or both of the shear families, with directional alternation expressed at multiple wavelengths. Regions of curvature stability coincide with predicted low-shear or invariant-contour domains, while zones of strong curvature change tend to occur where the two shear families rotate rapidly or intersect.

In this interpretation, glacial excavation, flexural rebound, and sedimentary loading provide the dominant mechanical processes, while the long-wavelength shear topology biases which orientations persist and accumulate over geological time. The behaviour is consistent with the broader cross-

continental pattern in which geomorphic and tectonic curvature appears preferentially where the modeled framework predicts coherent shear geometry.

### 3.8 British–Irish Geomorphic and Structural Bimodality



Figure 9: Bimodal geomorphic orientation in the United Kingdom, particularly Scotland, aligned with both shear families.

Across Britain and Ireland, large-scale landscape and structural patterns exhibit a pronounced bimodality in orientation and curvature, expressed in drainage networks, valley alignments, structural lineaments, and morphotectonic grain (e.g. Ballantyne, 2002; Woodcock and Strachan, 2014. Many of these features reflect the interaction of glacial modification, inherited basement structure, and later tectonic reactivation (Phillips et al., 2016).

When evaluated in the context of the modeled shear field, the dominant directional sets correspond closely to the two conjugate shear families, with alternation between them expressed at regional to trans-regional scales. Curvature stability and valley persistence are concentrated within predicted low-shear domains, while abrupt directional switching occurs near regions of rapid shear-trajectory rotation.

In this setting, glacial erosion, fluvial incision, and structural reactivation provide the princi-



pal geomorphic and tectonic processes. The long-wavelength shear framework is interpreted as a geometric environment that biases which orientations are preferentially preserved, re-excavated, or reactivated through successive climatic and tectonic cycles, consistent with observations of repeated lineament reuse in the British–Irish region (e.g. Woodcock and Strachan, 2014; Johnson, 1997).

### 3.9 East African Rift System

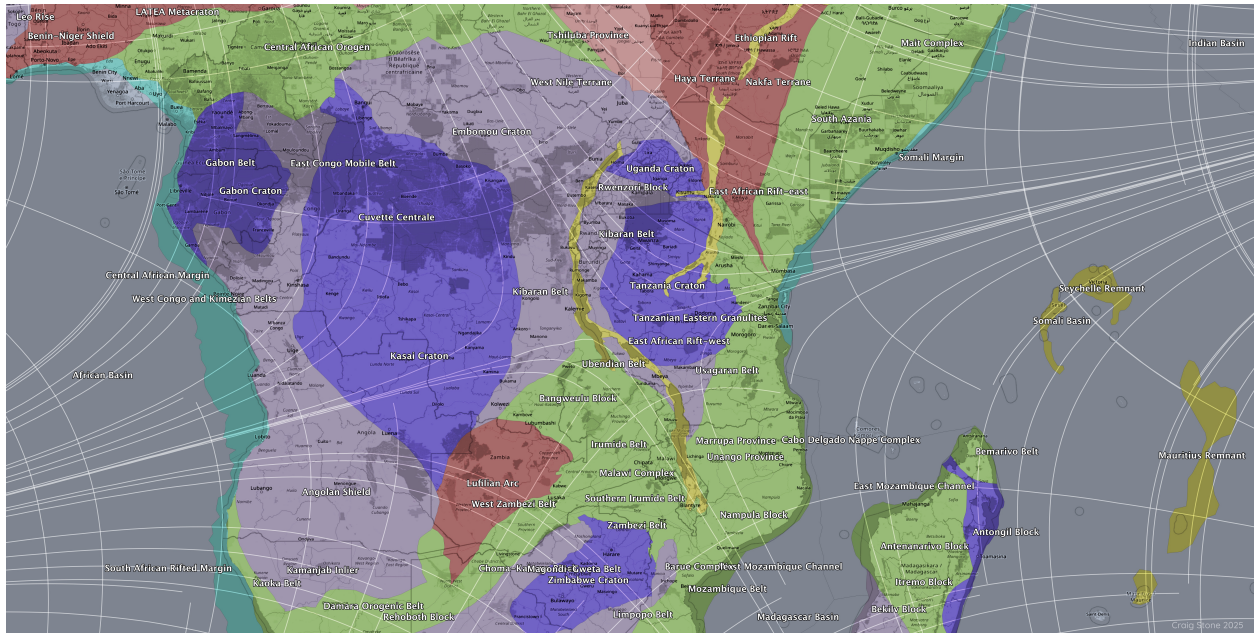


Figure 10: Double-arc geometry of the western East African Rift coincident with convergence of Net 1 and Net 2 near 14°S, 31°E.

### 3.10 The East African Rift System

The East African Rift System (EARS) represents an active zone of continental extension associated with lithospheric thinning, magmatism, and rift-segment development from the Afar triple junction to Mozambique (e.g. Ebinger, 1989; Taylor et al., 2013; Corti, 2009). Rift geometry varies along strike, with alternating straight and arcuate segments and systematic changes in rift-basin orientation through time (Corti, 2009).

Within the modeled shear framework, the principal rift corridors lie within domains where one shear family remains approximately parallel to the rift axis while the conjugate family rotates across the rift margin. Arcuate rift curvature and segment bifurcation occur preferentially in regions where the two shear families converge or rotate rapidly along strike. In these zones, local extensional processes may be predisposed to organise into sweeping curvature rather than linear fault segments.

This interpretation is consistent with observations that rift propagation and transfer-zone development are strongly influenced by pre-existing anisotropy and stress-field orientation (e.g. Corti,



2009; Philippon and Corti, 2015.

### 3.11 The Greenland–Hudson Bay Region

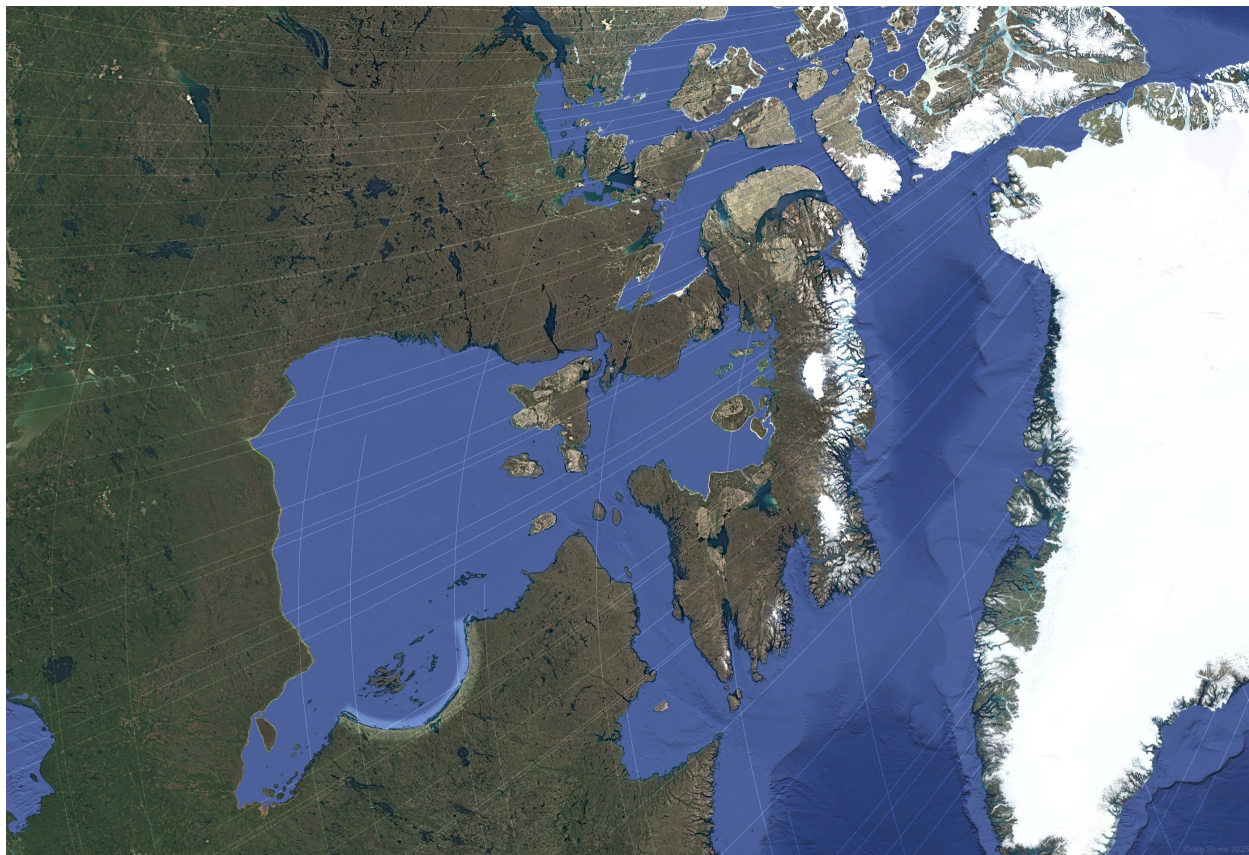


Figure 11: Greenland and Hudson Bay in polar stereographic projection showing bimodal agreement with shear nets and the arcuate Nastapoka structure.

The Greenland–Hudson Bay sector records a long history of Precambrian craton assembly, lithospheric stabilization, glacial loading and unloading, and intracontinental basin development (e.g. Philippon and Corti, 2015; Corti, 2009). The Hudson Bay depression and surrounding structural corridors display large-radius curvature and concentric basin geometry that have been linked primarily to glacial isostatic adjustment and crustal flexure (Andrews and Peltier, 1970).

When compared with the modeled shear framework, major basin margins, reactivated structural corridors, and regional lineament sets occur preferentially along one or both shear-trajectory families, with alternating alignment expressed at regional to continental scales. Domains of curvature stability coincide with predicted low-shear regions, whereas directional switching and structural dispersion occur near zones of rapid shear-trajectory rotation.

In this interpretation, glacial and flexural processes remain the dominant mechanisms responsible for basin formation and landscape modification. The long-wavelength shear framework is

treated as an organising geometry that helps explain the persistence and directional coherence of curvature across structurally heterogeneous crustal provinces, consistent with evidence for repeated structural reactivation in the Canadian Shield and adjacent regions (e.g. Percival et al., 2012).

### 3.12 Northwestern Canada and the Fort Simpson Arc

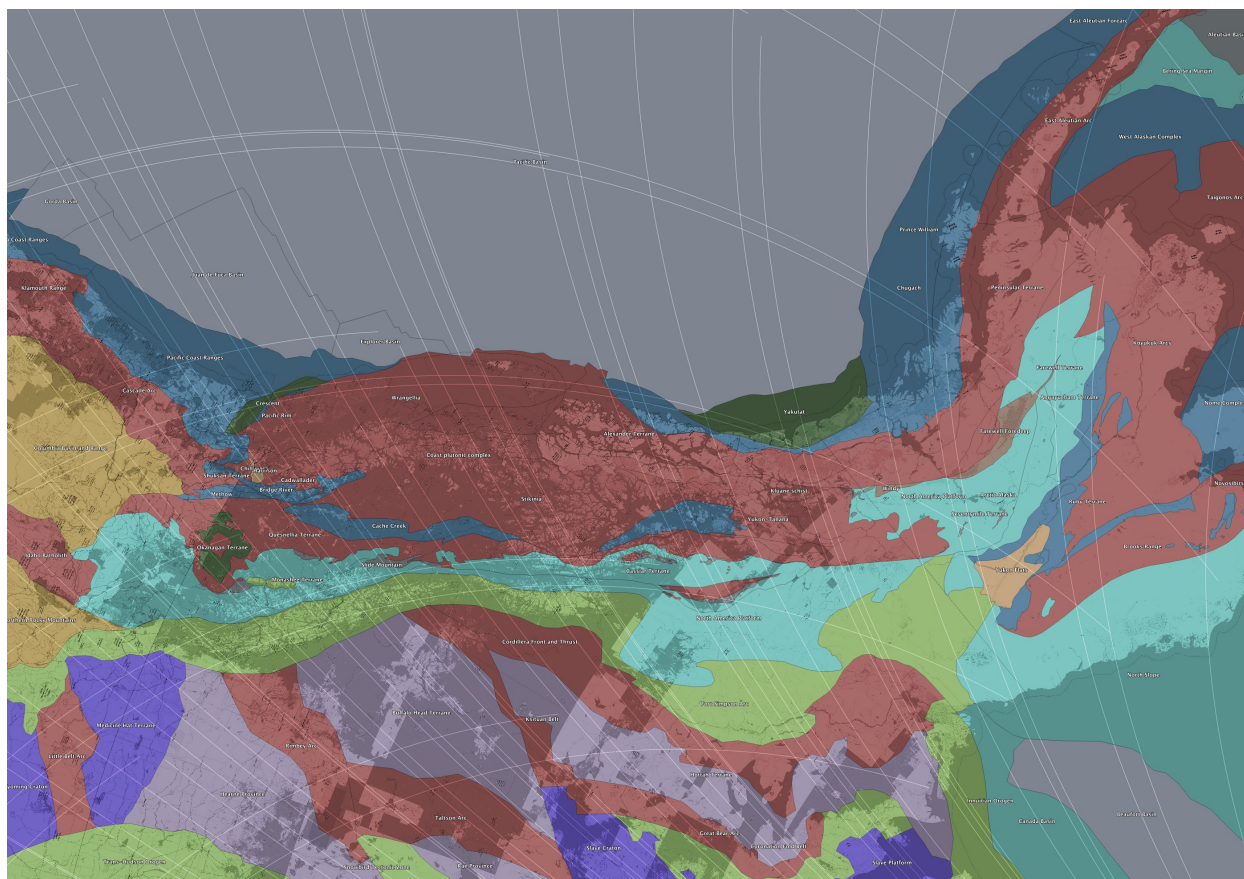


Figure 12: Northwestern Canada showing multiple agreements with shear nets, including the Fort Simpson Arc and transition from the Coast Plutonic Complex to the East Aleutian Arc.

The Fort Simpson Arc anomaly (FSA) of northwestern Canada has traditionally been interpreted as an Early Proterozoic magmatic arc, based on its curvilinear aeromagnetic signature, associated positive gravity anomalies, and U–Pb zircon ages clustering near  $\sim 1.85$  Ga from granitoid basement exposures. This interpretation, while well supported by geochronological and petrological evidence, encounters several persistent geometric and tectonic ambiguities that warrant re-examination in light of the global shear-net framework developed here.

Previous syntheses note that the Fort Simpson anomaly is not a simple linear feature, but instead broadens and curves westward into large elliptical magnetic highs near Great Bear Lake, among the most extensive aeromagnetic features in North America. Even within conventional interpretations, these western highs are acknowledged as potentially distinct basement elements that appear unified

only through filtered geophysical datasets. Moreover, the Fort Simpson domain exhibits a long history of reactivation, influencing later extensional basins, dyke swarms, hydrothermal systems, and lithospheric segmentation over a time span exceeding one billion years.

When examined in polar and Arctic projections, the Fort Simpson Arc displays a close geometric correspondence with one of the principal branches of the modeled global shear net. In particular, the curvature, bifurcation, and apparent bimodality of the Fort Simpson structure coincide with zones of net convergence and rotation in the shear trajectories. This correspondence is independent of stratigraphic boundaries, terrane affinities, or magmatic age constraints, suggesting a kinematic control that predates and outlasts any single tectono-magmatic episode.

Within this framework, Early Proterozoic arc magmatism is reinterpreted not as the origin of the Fort Simpson structure, but as one expression of a pre-existing lithospheric shear corridor. Such corridors are expected to localize mantle upwelling, magma ascent, and crustal underplating during periods of favorable stress orientation, while remaining mechanically weak and prone to reactivation under subsequent stress regimes. The coincidence of the Fort Simpson anomaly with positive gravity signatures is consistent with shear-focused lower-crustal densification or mafic underplating, rather than requiring a uniquely arc-related mechanism.

This reinterpretation resolves several longstanding difficulties associated with an arc-only model. The pronounced curvature and elliptical geometry of the Fort Simpson anomaly, its apparent continuity despite internal geological heterogeneity, and its repeated reactivation through Proterozoic and Phanerozoic time are all natural consequences of long-lived lithospheric shear structures, but are atypical of transient subduction-related arcs. Importantly, this perspective does not negate the arc-related geochemical and geochronological evidence documented in earlier studies; rather, it reframes arc magmatism as a secondary response to an inherited stress architecture.

In this view, the Fort Simpson Arc anomaly represents a lithospheric-scale shear feature that has acted as a persistent organizer of deformation and magmatism since at least the Paleoproterozoic. Its alignment with the global shear net supports the broader hypothesis that certain first-order continental geological features are governed by planet-scale kinematic patterns associated with large-amplitude true polar wander, rather than by isolated plate-boundary processes alone.

### **3.13 The North Atlantic–Arctic Sector**

The North Atlantic–Arctic region records a complex history of rifting, continental breakup, seafloor spreading, and passive-margin evolution associated with opening of the North Atlantic and Arctic basins (e.g. Doré et al., 2002; Eagles and Scott, 2004; Buck, 2015). Large-radius curvature is present in rifted margins, shelf escarpments, and offshore basin chains extending from the Labrador Sea through Greenland and into the Eurasian Arctic.

Comparison with the modeled shear field shows that many of these arcuate margin and basin geometries align with one or both shear-trajectory families, with directional alternation expressed over scales of several thousand kilometres. Regions of reduced curvature variability and long-



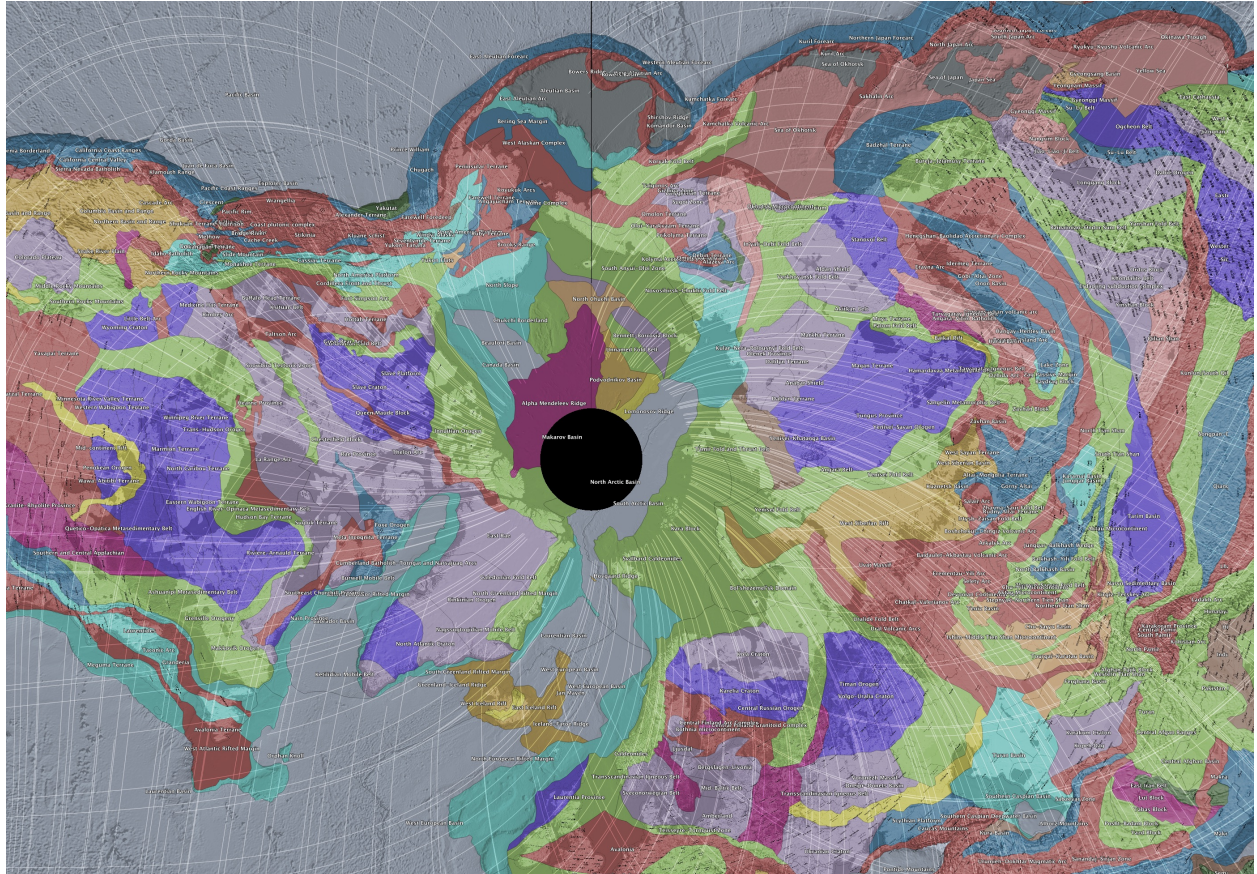


Figure 13: Arctic polar projection showing analytically derived shear trajectories overlaid on a global tectonic and geological province compilation. The shear lines exhibit strong geometric correspondence with the curvature, orientation, and boundaries of major circum-Arctic geological provinces across North America, Greenland, and Eurasia.



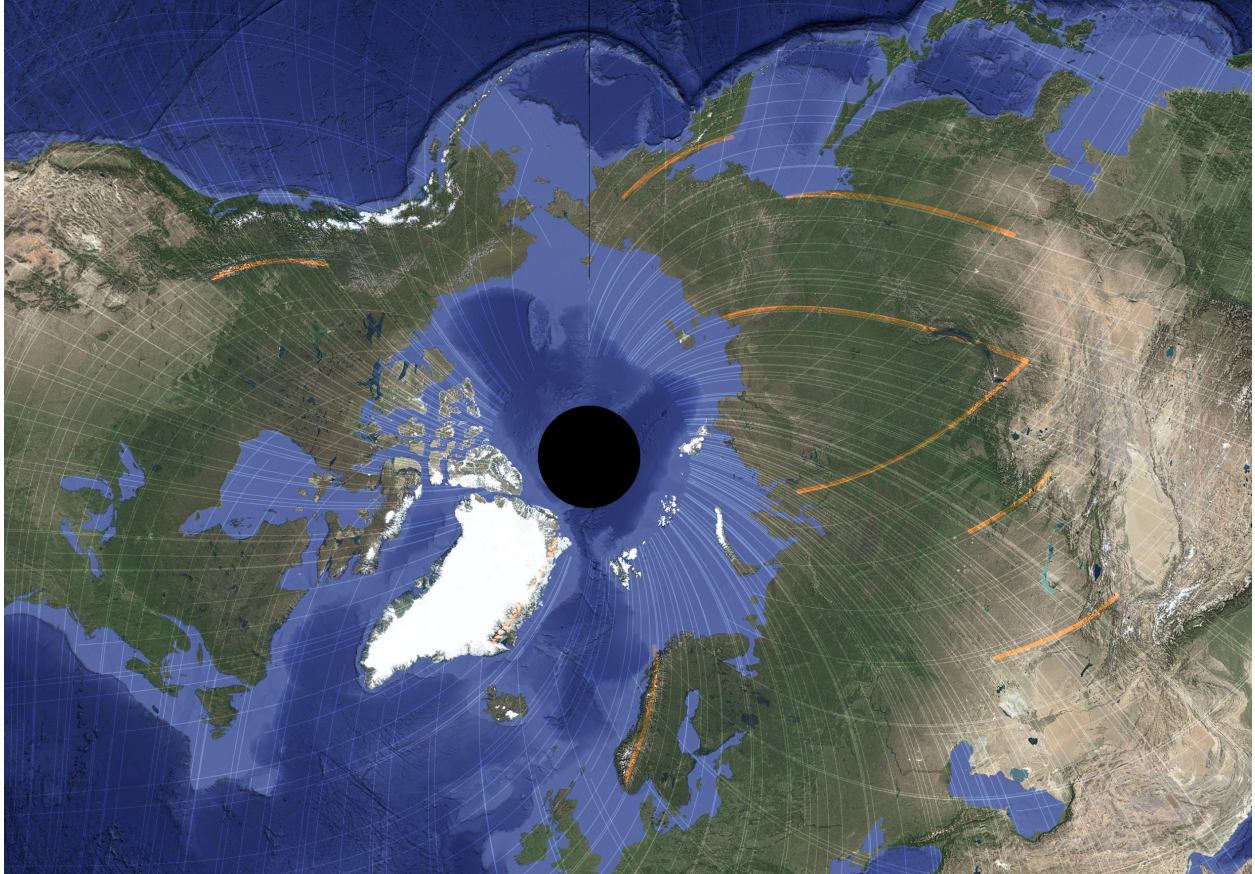


Figure 14: Arctic polar projection of shear trajectories over satellite imagery and bathymetry. Large-scale coastal arcs, continental shelf edges, submarine ridges, and basin margins frequently align with the modeled shear field, highlighting coherence across both continental and oceanic domains.

wavelength morphological continuity occur preferentially within predicted low-shear or invariant-contour domains, whereas irregular segmentation tends to coincide with areas where the two shear families rotate rapidly along strike.

These correspondences are not taken to imply that the shear field generated margin architecture. Rifting, magmatism, and plate rupture remain the primary drivers of North Atlantic–Arctic evolution. In the present interpretation, the modeled framework instead helps explain why curvature and segmentation recur with similar spatial organisation across multiple passive-margin systems of differing age and tectonic history.

### **3.14 Mid- to High-Latitude Glacial Morphology and Shear-Guided Landscape Expression**

Across numerous mid- and high-latitude regions, glacially sculpted terrains exhibit recurring directional coherence that aligns with the modeled global shear framework. These expressions occur in settings ranging from formerly glaciated continental interiors to high-relief fjord systems and tectonic margins, where Pleistocene and earlier glacial activity has repeatedly interacted with inherited structural anisotropy.

In many such regions, valley networks, fjord orientations, drumlin fields, and basin alignments display systematic alternation between the two modeled shear families, or preferential occupation of invariant-contour domains. This behaviour is observed in Scandinavia, the Canadian Shield, Greenland, coastal Patagonia, and segments of the Scottish Highlands, where glacial erosion has preferentially exploited shear-aligned weakness zones and curvature-stable domains.

These relationships are not readily explained by ice-flow dynamics alone. While ice-sheet geometry and basal processes strongly influence erosion patterns, they do not by themselves account for the persistence of large-radius curvature, repeated directional bimodality, or coherence across lithologically and tectonically contrasting terranes. Instead, the observed morphology is more consistent with selective enhancement of pre-existing, shear-guided structural fabrics through repeated cycles of glacial occupation and unloading.

Invariant-contour regions in particular tend to coincide with broad, low-strain basins and gently curving depressions that act as long-term sediment traps or loci of glacial lake development. Conversely, shear-trajectory corridors correspond to linear to curvilinear zones of enhanced incision, fjord development, and valley deepening, where stress-aligned structures provide mechanically favourable pathways for focused erosion.

This behaviour parallels that documented in the North American arcuate lake chain and in parts of Greenland and Scandinavia, where landscape anisotropy and curvature stability persist across multiple glacial cycles. The coherence of these relationships across continents and hemispheres supports interpretation of glacial morphology as an amplifying and revealing agent acting upon a longer-lived, planet-scale shear organisation rather than as an independent generator of curvature.

Taken together, these glacially expressed examples reinforce a broader pattern evident through-

out the case studies: regions of persistent curvature, directional bimodality, and organised anisotropy tend to occur where the modeled field predicts stable stress geometry across scales. This behaviour is consistent with the statistically significant spatial organisation of misfit demonstrated in Section 6, further linking geomorphic expression to the same long-wavelength stress topology inferred from the stress-orientation analyses.

### **3.15 Large-Radius Ocean-Basin Curvature Provinces**

Beyond plate-boundary systems, large-radius curvature is also expressed in bathymetric arcs, abyssal fabric trends, and basin-scale morphological sweeps across several ocean basins, including sectors of the South Atlantic, Indian Ocean, and southwest Pacific. These features arise from a combination of spreading-ridge segmentation, transform-fault organisation, sedimentary infill, and thermal subsidence (e.g. Parsons and Sclater, 1977; Macdonald, 1984).

Across these regions, the orientation of basin-scale curvature frequently alternates between the two modeled shear families, and long-wavelength continuity is most pronounced within predicted low-shear domains. Where shear-trajectory rotation is rapid, curvature becomes segmented or irregular, paralleling the behaviour observed in continental and passive-margin examples.

As in the other case studies, the interpretation advanced here is geometric rather than causal: spreading and sedimentary processes remain primary, while the modeled shear topology provides a potential explanation for the recurrence and spatial organisation of curvature across ocean-basin scales.

### **3.16 Continental Margin Curvature, Passive-Margin Arcs, and Long-Wavelength Structural Guidance**

Curved passive margins and continental-shelf arcs occur along several major continental outlines, including segments of the West African margin, northern South America, the western Australian shelf, and portions of the Antarctic and Arctic continental rims. These features are commonly attributed to variations in rift propagation, diachronous breakup, sediment loading, or flexural response to differential margin subsidence. While these processes play important roles in shaping margin architecture, they do not fully account for the persistence of smooth, large-radius curvature that transcends basin boundaries, stratigraphic transitions, and breakup histories.

When examined within the modeled global shear framework, many of these passive-margin arcs coincide with invariant-contour domains or trace trajectories that are parallel to one of the two shear families over distances of hundreds to thousands of kilometres. The congruence is particularly evident where margin curvature remains coherent across multiple rift episodes or across transitions from volcanic to non-volcanic margin segments, implying control by an organising stress geometry rather than by locally restricted breakup kinematics alone.

Several major continental shelves display gently sweeping curvature in shelf-edge trajectories and sediment-wedge outlines that follow shear-aligned pathways despite contrasts in sediment sup-

ply, basin subsidence history, or margin thermal state. In these cases, depositional architecture appears to have evolved within a preconditioned stress topology that favoured curvature stability and long-term geometric persistence, with stratigraphic processes amplifying rather than generating the underlying planform geometry.

Where transform-bounded margin segments intersect shear-trajectory corridors, margin curvature commonly tightens and structural segmentation becomes more pronounced. Conversely, margins coincident with invariant-contour regions exhibit broad, laterally continuous curvature with reduced structural partitioning. This systematic variability is consistent with deformation and margin evolution being conditioned by spatial gradients in the long-wavelength shear field.

These relationships parallel behaviours documented in passive-margin sediment belts, arcuate rifts, and ocean-basin curvature systems elsewhere in this study. In each case, large-radius curvature and directional stability are most clearly expressed where the modeled field predicts low-variance or convergent shear geometry across scales. The recurrence of this pattern suggests that passive-margin curvature is not solely the by-product of breakup mechanics, but reflects interaction between plate separation, sedimentation, and a persistent, planet-scale stress organisation.

In this interpretation, passive margins act as long-term recorders of curvature-stable domains within the global shear topology. Their planform geometry evolves through the cumulative superposition of rifting, thermal subsidence, and sediment loading on an inherited geometric framework—behaviour consistent with the scale-persistent spatial organisation demonstrated quantitatively in Section 6.

## 4 Regional Expressions and Cross-Scale Geometric Consistency

The regional examples presented in this section illustrate how the modeled shear framework is expressed across contrasting tectonic, geomorphic, and depositional environments. These examples are not offered as mechanistic reconstructions; local tectonic processes such as convergence, rifting, magmatism, glaciation, and sediment routing remain essential to the formation and evolution of each system (e.g. Zoback, 1992; Heidbach et al., 2018). Rather, the case studies assess whether large-radius curvature, directional bimodality, and structural persistence occur preferentially in regions where the modeled field predicts stable or convergent shear geometry.

Qualitative comparison is therefore interpreted as complementary to the spatial-statistical analysis. Whereas the statistical tests evaluate whether the misfit field exhibits non-random geographic organisation, the case studies examine whether similar organisation is expressed in large-scale geological curvature. Consistency across these independent perspectives is taken as *convergent evidence*, not proof of causation.

—



## 5 Global Plate Boundary Comparison

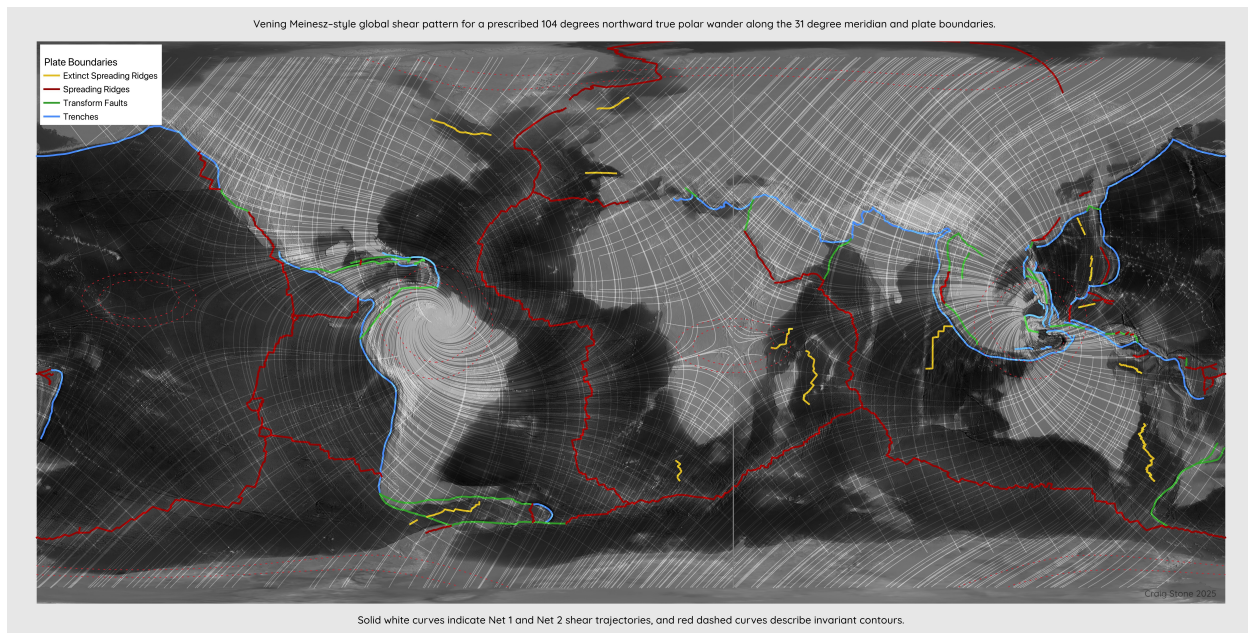


Figure 15: Comparison of the global shear model with modern plate boundaries. Strong geometric correspondence is observed across subduction arcs, transforms, and extinct ridges.

### 5.1 Comparative Behaviour of the Two Euler-Point Domains

The two Euler-point regions defined by the prescribed  $104^\circ$  northward true polar wander (TPW) along the  $31^\circ\text{E}$  meridian provide a natural experiment for evaluating how the modeled global shear field couples into contrasting tectonic environments (Figures 16 and 17). Although both regions exhibit clear correspondence with the Venning–Meinesz-style shear trajectories, the mode of conformance differs in ways that are geologically informative.

**Western Euler Domain.** The western Euler point, centered over northern South America and the Caribbean (Figure 16), exhibits the strongest and most internally consistent agreement between the shear model and observed geology. In this domain, shear trajectories form tightly wrapped spiral patterns that closely parallel Precambrian cratonic margins, mobile belts, and long-lived deformation zones. Major rift and transform boundaries, earthquake epicenter distributions ( $M \geq 4.5$  over the past 25 years), and active to historically active volcanic centers preferentially align tangentially to the modeled shear flow.

Notably, both ancient tectonic fabrics and present-day deformation are organized predominantly along shear-parallel trajectories rather than orthogonal to them. This indicates that the shear field has acted as a persistent organizing stress over multiple tectonic cycles, repeatedly reactivating

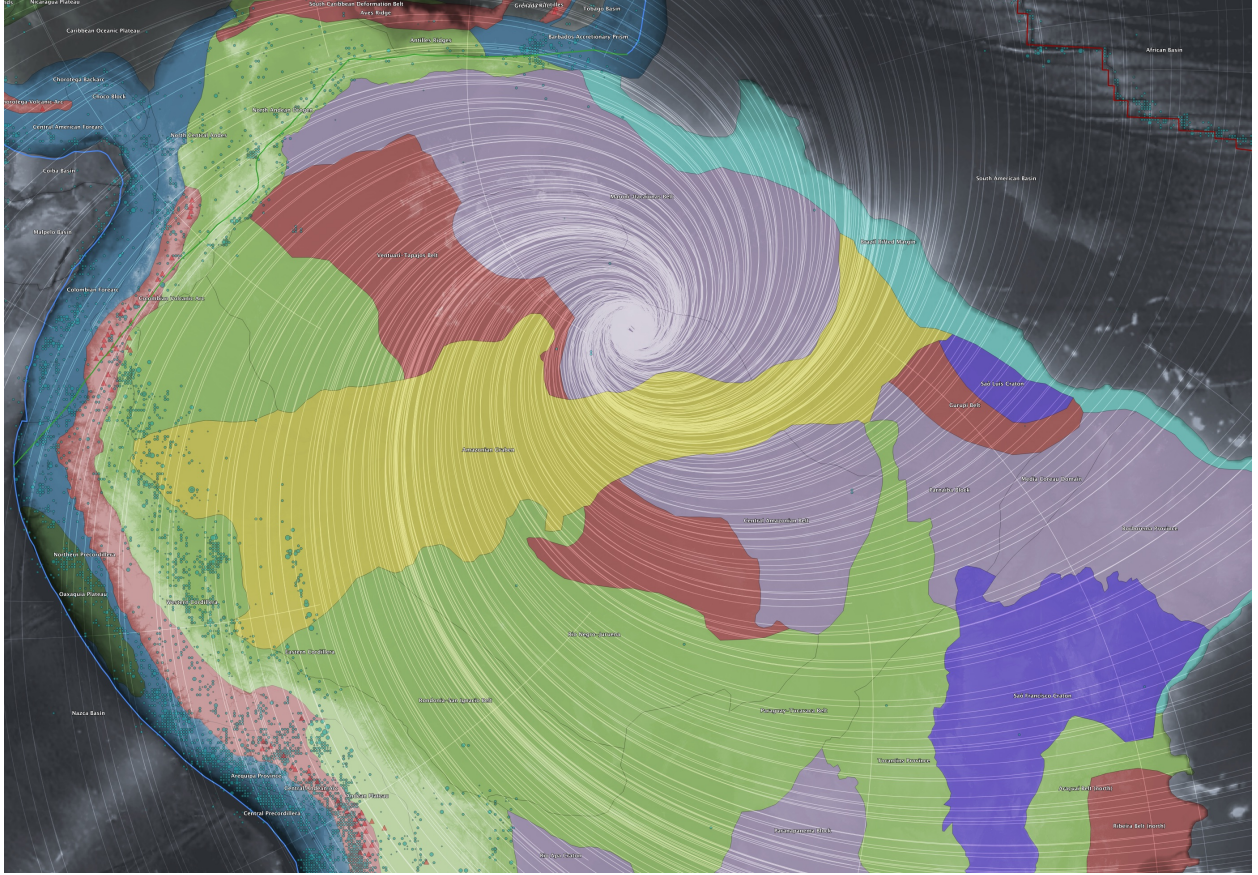


Figure 16: Western Euler-point domain showing the Venning–Meinesz–style shear trajectories overlaid on geological provinces, plate boundaries, earthquake epicenters ( $M \geq 4.5$ ), and volcanic centers.

inherited lithospheric weaknesses in geometrically consistent orientations. The high degree of spatial coherence suggests that thick, mechanically heterogeneous continental lithosphere is capable of preserving and expressing low-order global stress modes over geological timescales.

**Eastern Euler Domain.** The eastern Euler point, located within the Indonesia–Sunda–Banda tectonic collage (Figure 17), presents a contrasting but equally informative expression of the same underlying shear structure. This region is characterized by rapid plate convergence, slab rollback, arc–continent collision, and distributed back-arc deformation. Despite this complexity, several robust correspondences with the shear model remain evident.

Major arcuate subduction systems, including the Banda and Sunda arcs, follow curvature consistent with modeled shear trajectories rather than simple relative plate-motion vectors. Earthquake hypocenters cluster along curved bands that mirror regions of maximum shear curvature, while active and historical volcanism preferentially occupies shear-aligned arc segments and convergence zones. In this domain, rift boundaries and basin margins exhibit mixed behavior: some conform closely to shear trajectories, whereas others are dominated by local slab geometry and rollback dynamics. This indicates that while the shear field does not dictate tectonic behavior outright, it



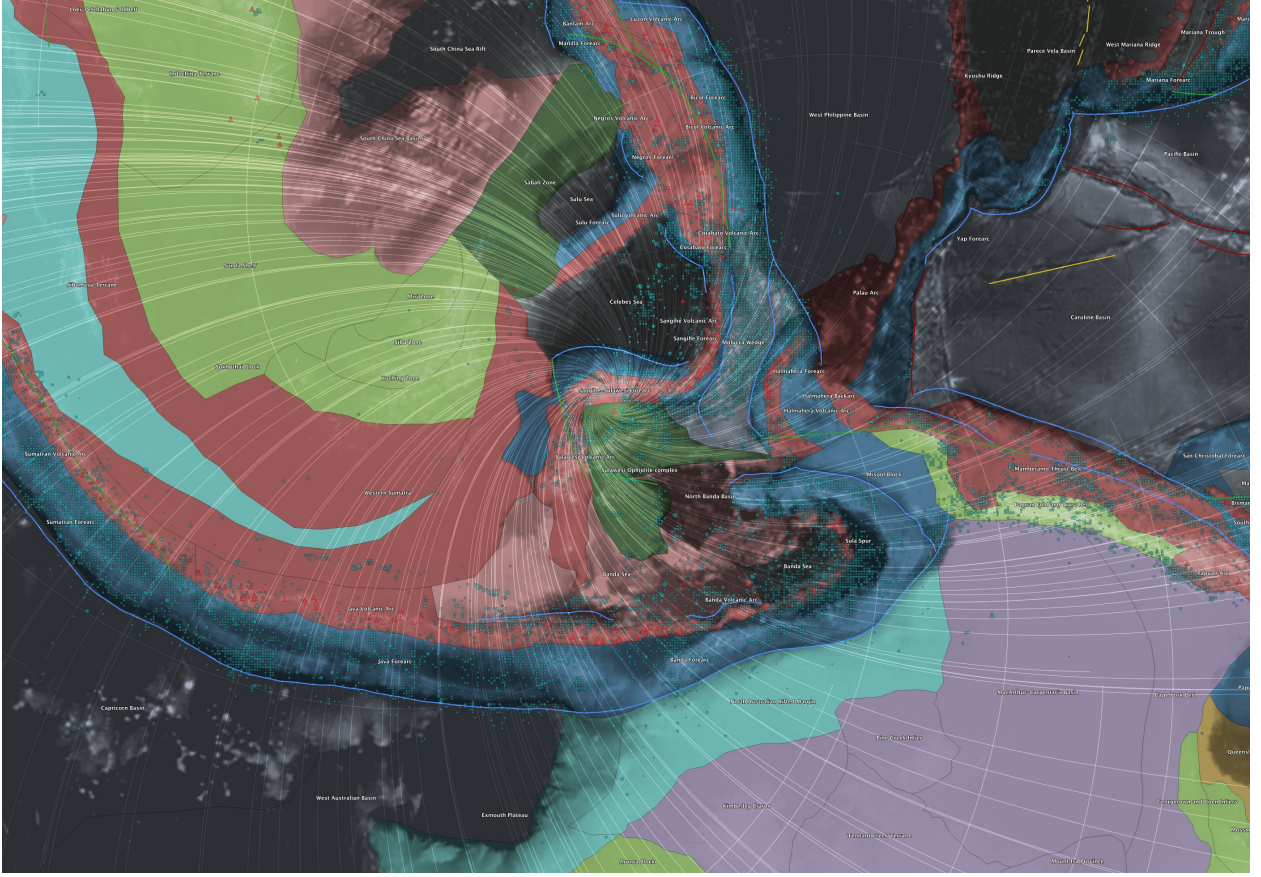


Figure 17: Eastern Euler-point domain (Indonesia–Sunda–Banda region) illustrating the relationship between modeled shear trajectories, arcuate subduction systems, seismicity, and active volcanism.

acts as a geometric constraint within which subduction-driven processes organize themselves.

**Comparative Implications.** The contrasting behavior of the two Euler domains highlights several important implications. First, the persistence of recognizable shear conformance in both stable continental interiors and highly active subduction zones argues against coincidental alignment and supports the presence of a global, low-order stress architecture capable of coupling into diverse lithospheric contexts. Second, regions underlain by thick, ancient lithosphere appear to preserve shear-imposed geometry more faithfully than rapidly recycling convergent margins, emphasizing the role of lithospheric memory in amplifying the visibility of the shear field.

Finally, the results indicate that the modeled shear structure should be understood not as a replacement for plate tectonics or mantle convection, but as a superimposed, long-wavelength stress mode that biases the orientation, curvature, and persistence of tectonic features generated by those processes. The systematic differences observed between the western and eastern Euler-point domains therefore strengthen the interpretation that the Venning–Meinesz–style global shear field represents a persistent and physically meaningful component of Earth’s geodynamic system.

## 6 Scale-Dependent Spatial Autocorrelation of the Misfit Field

Across all examined spatial scales from 250 to 4000 km, the stress–misfit field exhibits statistically significant positive spatial autocorrelation. Moran’s  $I$  decreases smoothly with increasing scale, from strong regional clustering to weaker but resolvable near-hemispheric organization. No abrupt loss of significance is observed.

This behavior indicates a finite but large correlation length for stress–misfit organization, extending well beyond individual plate boundaries or continental domains. The attenuation of Moran’s  $I$  toward hemispheric scales marks a transition from regional clustering to low-degree global structure rather than a disappearance of spatial coherence.

### 6.1 Short-Wavelength Structure (250 km)

At a spatial scale of 250 km, the misfit field exhibits very strong positive spatial autocorrelation, with Moran’s  $I = 0.30$ . The permutation null distribution has a mean effectively indistinguishable from zero and extremely small variance, yielding  $p \ll 10^{-6}$ . This result confirms that misfit values are highly clustered at short wavelengths and establishes a robust baseline of spatial coherence. At this scale, clustering is expected to reflect dominant local and regional tectonic controls, including fault systems, plate boundary geometry, and lithospheric heterogeneity.

### 6.2 Regional-Scale Coherence (500 km)

At 500 km, Moran’s  $I$  remains large ( $I = 0.23$ ) and highly significant under permutation testing ( $p \ll 10^{-6}$ ). The reduction in Moran’s  $I$  relative to 250 km reflects the expected decay of spatial correlation with distance, while the persistence of strong autocorrelation demonstrates that stress–misfit organization extends well beyond strictly local interactions. This scale corresponds to regional tectonic domains and large plate-boundary systems, indicating coherent stress structure at continental scales.

### 6.3 Long-Wavelength Organization (1000 km)

At a spatial scale of 1000 km, the misfit field continues to exhibit strong and statistically significant spatial autocorrelation, with Moran’s  $I = 0.17$  and  $p \ll 10^{-6}$ . The persistence of coherent structure at this wavelength exceeds typical crustal or single-orogen length scales and points to long-wavelength organization of the stress field. At this scale, purely local tectonic explanations become increasingly implausible, suggesting the influence of broader lithospheric or mantle-scale processes.

## 6.4 Planetary-Scale Persistence (2000 km)

At the largest scale examined, 2000 km, Moran’s  $I$  remains positive and highly significant ( $I = 0.11$ ,  $p \ll 10^{-6}$ ). Although reduced in magnitude relative to shorter scales, the continued presence of statistically robust spatial autocorrelation at near-planetary wavelengths demonstrates that the stress–misfit field is organized over distances comparable to hemispheric dimensions. This result rules out explanations confined to regional tectonics alone and establishes a minimum correlation length of at least several thousand kilometers.

## 6.5 Upper-Bound Scale and Finite Correlation Length

Extending the spatial autocorrelation analysis to larger neighborhoods further clarifies the scale dependence of the stress–misfit field. At 3000 km, Moran’s  $I$  remains positive and statistically robust ( $I = 0.073$ ,  $p \ll 10^{-6}$ ), indicating coherent organization at near-hemispheric wavelengths. At 4000 km, the magnitude of Moran’s  $I$  is reduced but remains resolvably positive ( $I = 0.050$ ,  $p \ll 10^{-6}$ ), demonstrating that spatial structure persists even as neighborhood extents approach hemispheric scales.

Taken together, results from 250 to 4000 km reveal a smooth, monotonic decay of Moran’s  $I$  with increasing spatial scale, without abrupt loss of significance. This behavior indicates a finite correlation length for the stress–misfit field, rather than unbounded or scale-invariant organization. The attenuation of spatial autocorrelation toward hemispheric extents marks the transition from regional clustering to low-degree global structure and represents the practical upper limit of interpretability for distance-based spatial autocorrelation metrics such as Moran’s  $I$ .

## 6.6 Scale Dependence and Correlation Length

Taken together, the results reveal a smooth, monotonic decay of Moran’s  $I$  with increasing spatial scale, without loss of statistical significance across the full range examined (250–3000 km). Such behavior is characteristic of a genuine spatial correlation process with a long correlation length, rather than noise or sampling artifacts. The absence of a sharp cutoff indicates that the organizing mechanism operates across multiple spatial regimes, from local tectonic structure to global-scale stress organization.

## 6.7 Global Alignment versus Spatial Structure

Two distinct statistical questions are addressed in this study: (1) whether the modeled shear field globally outperforms random Euler rotations in terms of mean angular misfit, and (2) whether the spatial distribution of misfit exhibits non-random geographic structure. These questions are evaluated using different null models and are not equivalent.

Global Euler-rotation null tests indicate that the mean misfit of the examined shear scenario does not differ significantly from that obtained under random rotations ( $p = 0.636$ ). This result

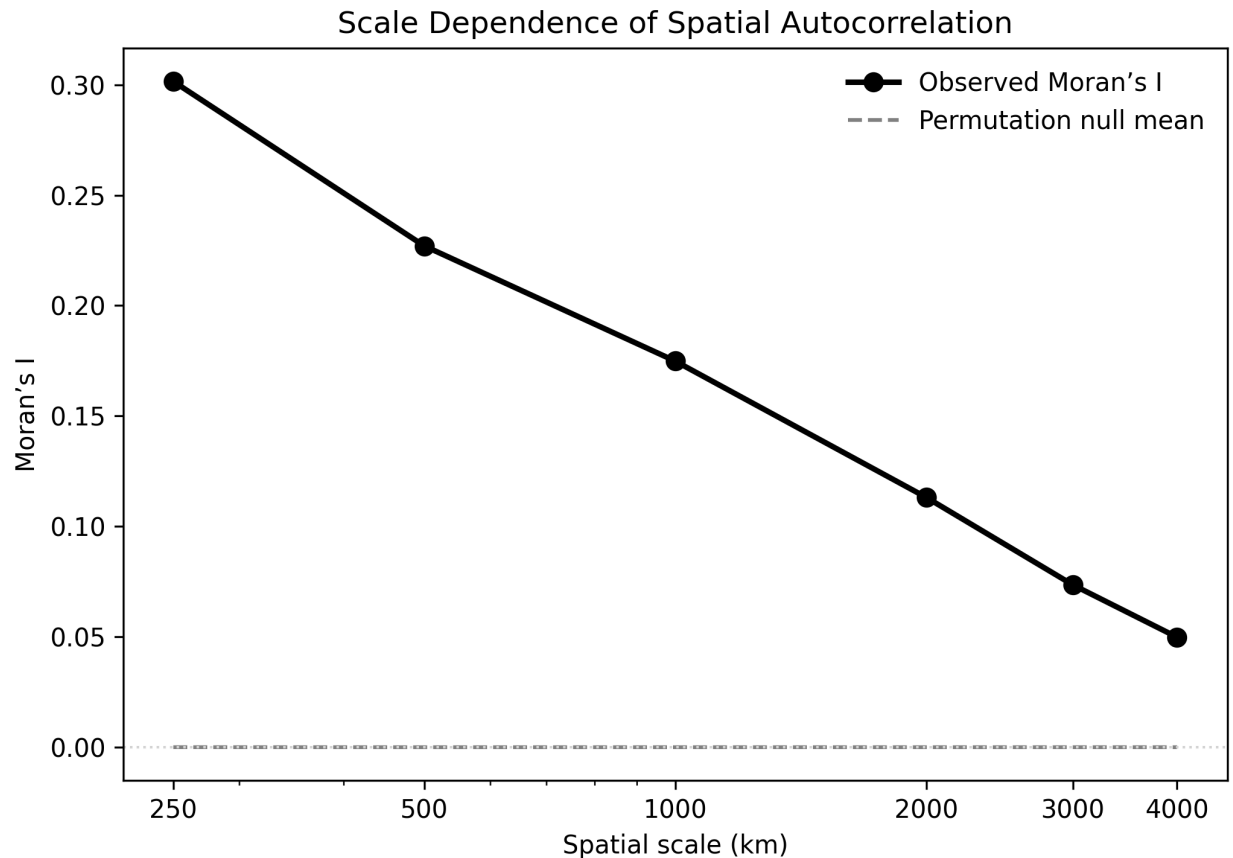


Figure 18: Scale dependence of spatial autocorrelation in the stress–misfit field. Global Moran’s  $I$  values are shown as a function of characteristic spatial scale from 250 to 4000 km. Observed values (solid symbols) exhibit a smooth, monotonic decay with increasing scale while remaining statistically significant under permutation-based null testing at all examined wavelengths. The permutation null expectation (dashed line) is indistinguishable from zero, indicating that the observed trend reflects genuine spatial organization rather than random spatial structure. The attenuation of Moran’s  $I$  toward hemispheric scales suggests a finite correlation length and marks the transition from regional clustering to low-degree global modes.

demonstrates that the model does not provide a globally optimal alignment in a scalar, average sense. Importantly, however, this test is insensitive to spatial organization and treats all locations as independent.

In contrast, permutation-based Moran’s  $I$  analysis directly evaluates whether misfit values cluster spatially beyond random expectation. This analysis reveals statistically robust spatial autocorrelation from 250 km through at least 3000 km, demonstrating coherent geographic structure in the misfit field. The coexistence of a non-significant global mean test and highly significant spatial autocorrelation indicates that the model captures structured regional and planetary-scale patterns rather than uniformly minimizing misfit everywhere.

Accordingly, the primary empirical result of this study is not improved global alignment, but the detection of long-wavelength spatial organization in stress–misfit patterns that cannot be explained by random spatial processes.

## 6.8 Scenario Scope and Sensitivity Considerations

The shear field examined in this study corresponds to a single, untuned rotational scenario involving a  $\sim 104^\circ$  reorientation along the  $31^\circ\text{E}$  meridian. This configuration was selected as a representative test case motivated by prior ECDO-related considerations rather than as an optimized or best-fitting solution.

No attempt has been made here to exhaustively explore parameter space or to identify a globally optimal rotation. Instead, the objective is to assess whether a physically plausible, non-optimized long-wavelength shear scenario produces detectable and statistically robust spatial structure in stress–misfit patterns. The strong spatial autocorrelation observed across multiple length scales demonstrates that such structure is present even without parameter tuning.

Future work will extend this framework to systematic sensitivity analyses, including alternative rotation axes, magnitudes, and temporal scenarios. The permutation-based Moran’s  $I$  methodology introduced here provides a quantitative basis for comparing such scenarios without relying on global mean misfit alone.

## 6.9 Relation to Paleomagnetic Constraints on True Polar Wander

Proposed true polar wander (TPW) scenarios are subject to constraints derived from paleomagnetic reconstructions, which typically limit long-term TPW amplitudes to tens of degrees over multimillion-year timescales (e.g., Steinberger & Torsvik, 2008). These constraints are primarily sensitive to time-averaged rotational behavior and are optimized to detect sustained, low-frequency reorientations of the solid Earth.

The present analysis does not attempt to reconstruct the timing, duration, or cumulative magnitude of any specific TPW event. Instead, it evaluates whether long-wavelength rotational shear scenarios leave a spatially coherent imprint on present-day stress orientations. As such, the re-

sults are compatible with both gradual and episodic reorientation models, including transient or non-steady processes that may not be fully captured by paleomagnetic averaging.

Accordingly, the spatial-statistical findings reported here should be interpreted as evidence for long-wavelength stress organization rather than as direct constraints on TPW kinematics. Integrating spatial stress analyses with paleomagnetic, geodynamic, and stratigraphic constraints represents a key direction for future interdisciplinary work.

## 6.10 Summary of Empirical Findings

The permutation-based spatial autocorrelation analysis demonstrates that the stress–misfit field is not spatially random at any examined scale. Instead, it exhibits strong and statistically robust geographic organization from local (250 km) through planetary (4000 km) wavelengths. These findings provide quantitative evidence for long-wavelength structure in the stress field and motivate interpretation in terms of global or mantle-coupled forcing mechanisms, which are explored in the Discussion.

## 7 Results: Spatial Statistical Structure of the Misfit Field

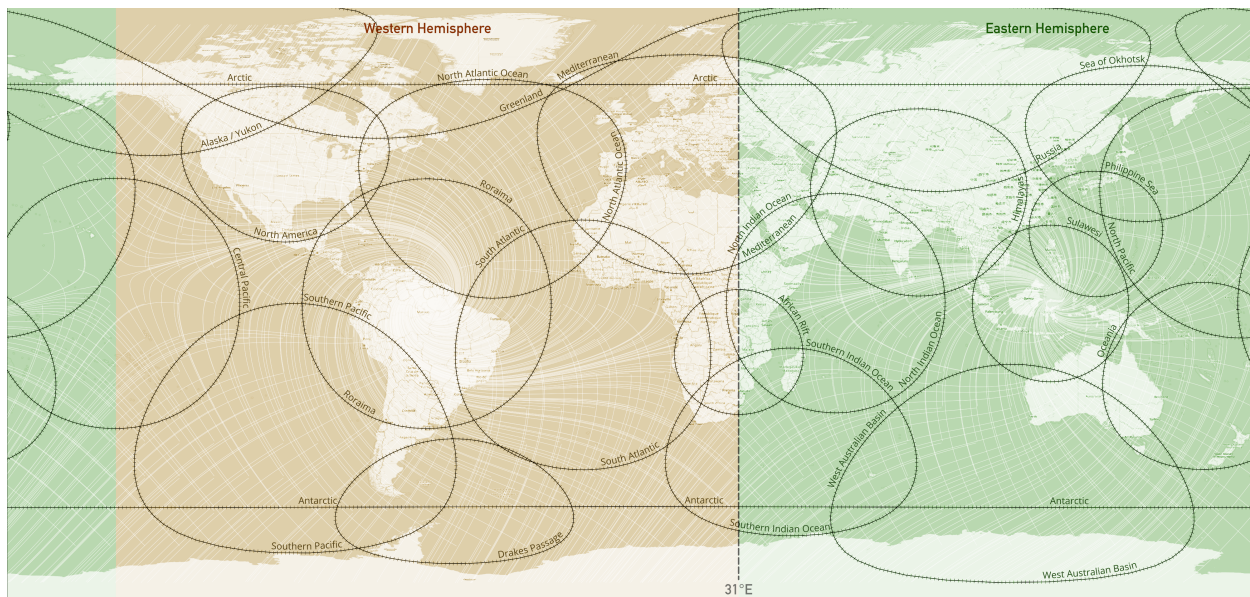
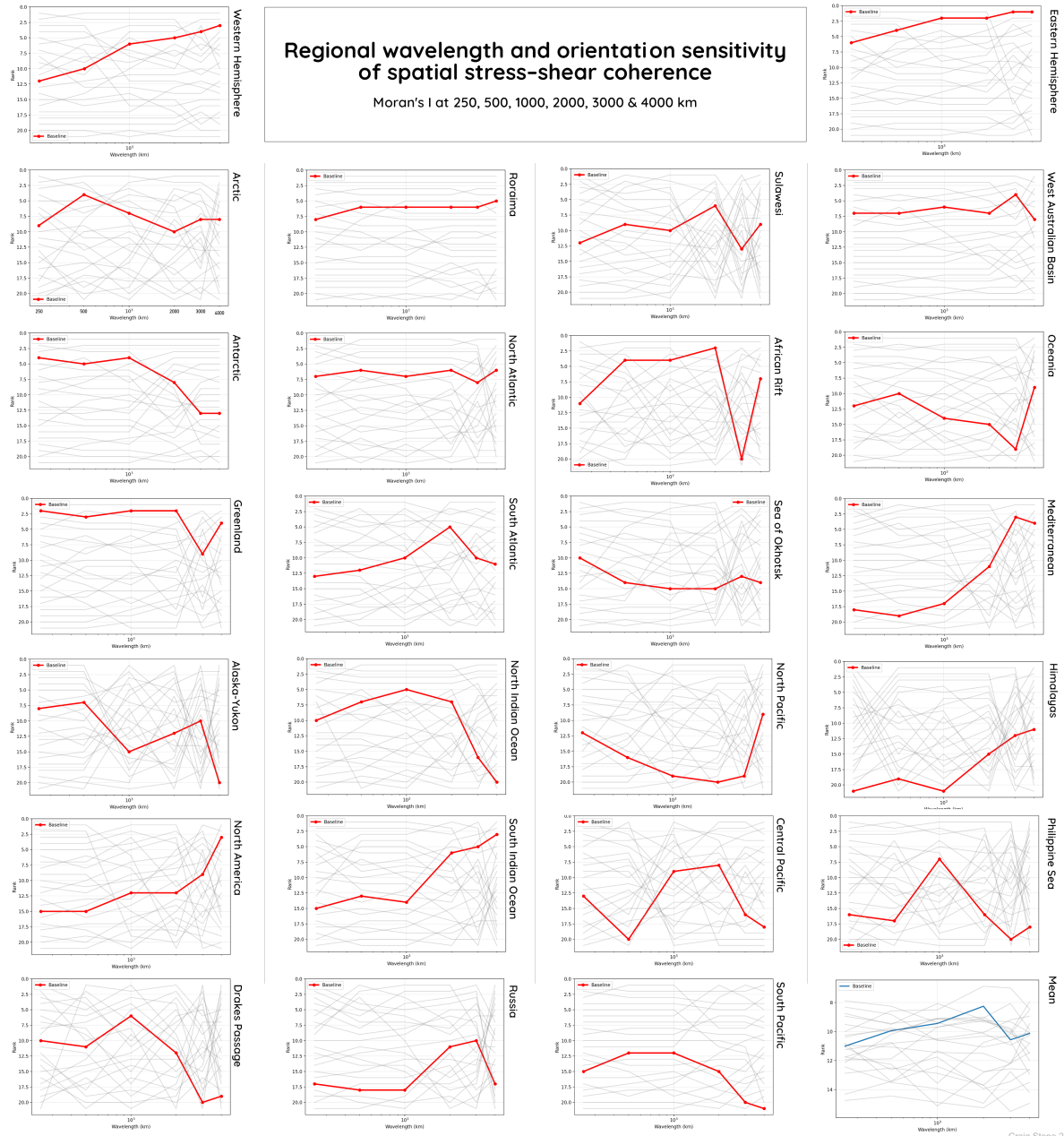


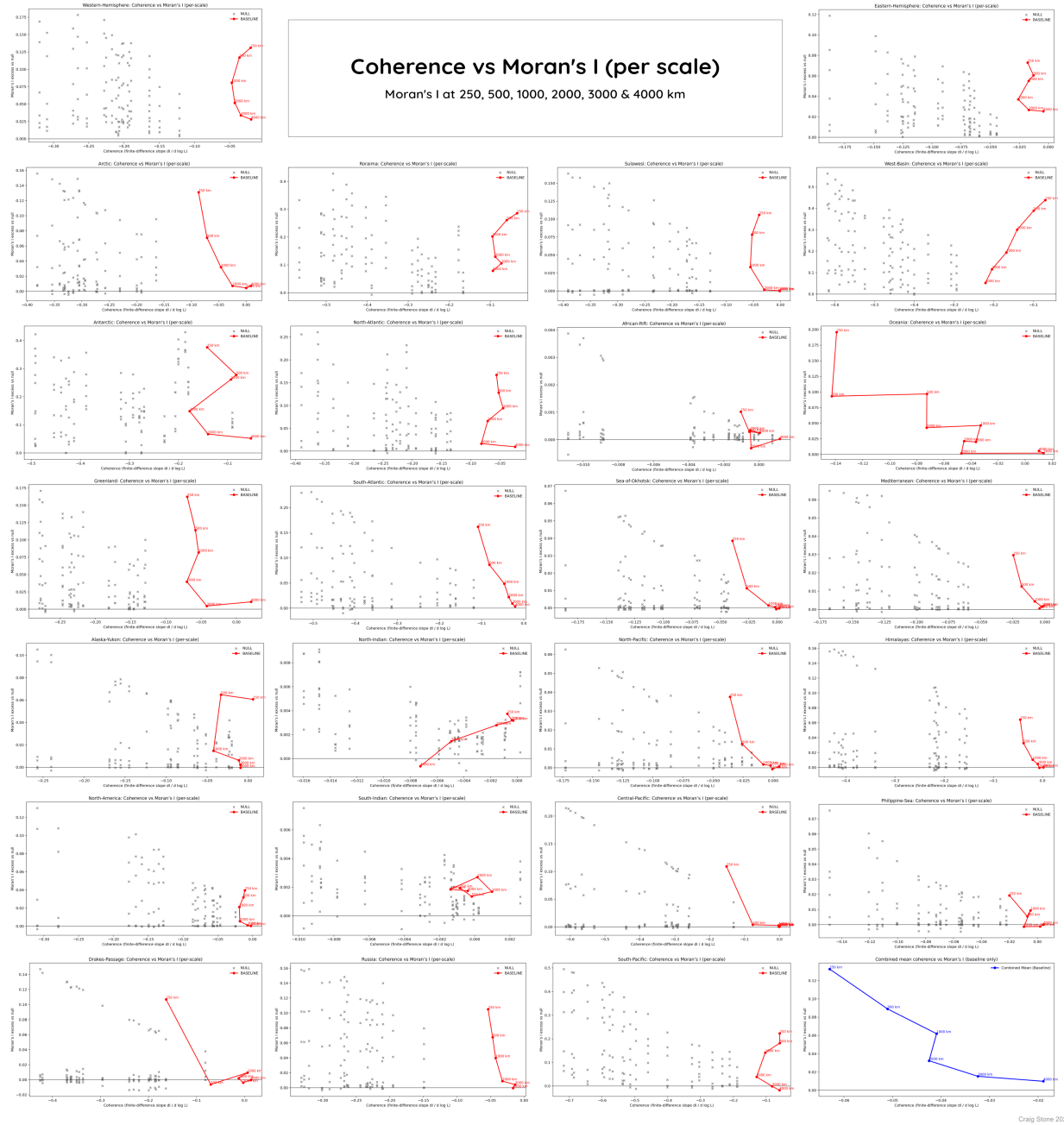
Figure 19: Geographic distribution of the sampled regions.





Craig Stone 2025

Figure 20: Regional wavelength–orientation sensitivity of spatial stress–shear coherence. For each region, Moran’s I was evaluated at 250, 500, 1000, 2000, 3000, and 4000 km wavelengths. The red curve shows the baseline TPW-derived shear geometry; grey curves represent the randomized null shear ensembles. Regions exhibiting plateaued or monotonic trends in the baseline response indicate structured, scale-dependent spatial coherence rather than noise-like behavior.



Craig Stone 2025

Figure 21: Coherence versus Moran's I (per-scale) across regions. Grey points represent the null ensemble; red curves trace the baseline TPW shear field for each wavelength step. The blue curve (lower right) shows the combined mean baseline trajectory relative to the null ensemble. Regions with smooth, structured trajectories show the strongest excess clustering, indicating non-random, scale-consistent spatial organization.

# Hemispheric wavelength, orientation and spatial coherence

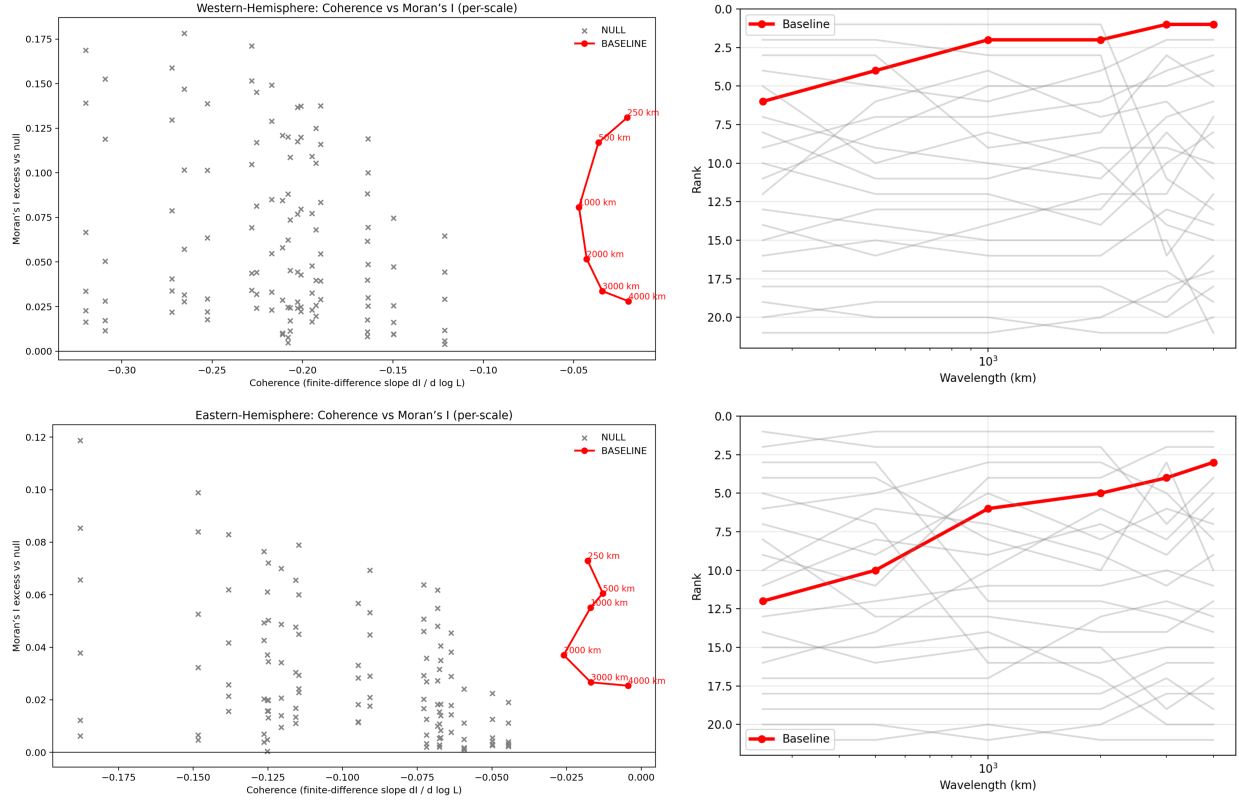


Figure 22: Hemispheric wavelength, orientation, and spatial coherence. The figure illustrates how the spatial organisation of the stress–orientation misfit field varies with wavelength in the Western (top) and Eastern (bottom) hemispheres. In both regions, the baseline shear-net solution (red) occupies a distinct trajectory in coherence–autocorrelation space relative to the rotated-Euler null ensemble (grey), with progressively higher excess Moran’s  $I$  at larger wavelengths (left panels). The corresponding rank plots (right panels) show that, across most scales, the baseline solution exhibits stronger spatial organisation of the misfit field than expected under random rotation, particularly at wavelengths of 1000–4000 km. Taken together, these results indicate that the large-scale structure in the misfit field is not a sampling artefact or purely regional effect, but a reproducible hemispheric-scale signal that emerges independently in both datasets. This pattern is consistent with the presence of an organised, long-wavelength component in the underlying stress field.

## 8 Results: Spatial Statistical Structure of the Misfit Field

### 8.1 Global Mean Alignment and Null-Model Behaviour

Global mean angular misfit between the modeled shear trajectories and WSM stress orientations falls within the empirical distribution generated by Euler-rotated null ensembles. Consistent with earlier findings that global scalar misfit does not, by itself, diagnose model adequacy (e.g. Cao et al., 2021; Stephan, 2023, the prescribed geometry does not produce a statistically significant

reduction in average misfit relative to internally coherent but randomly oriented fields.

This result establishes an important baseline: global mean alignment is non-diagnostic for this geometry and cannot, on its own, be used to justify or reject correspondence between the shear model and observed stress orientations.

## 8.2 Scale-Dependent Spatial Organisation of the Misfit Field

Permutation-based spatial autocorrelation analysis reveals that the misfit field exhibits statistically significant positive Moran’s  $I$  across spatial scales ranging from  $\sim 250$  km to  $\sim 4000$  km. The magnitude of Moran’s  $I$  decreases smoothly with increasing scale, ... a behaviour characteristic of genuine spatial correlation rather than sampling artefacts or edge effects in spatially irregular datasets (e.g. Cliff and Ord, 1981; Fortin and Dale, 2005).

At regional scales ( $\sim 250$ – $500$  km), clustering reflects coherent misfit domains that coincide with major tectonic regions and plate-boundary systems, consistent with earlier observations that stress orientation varies systematically with tectonic province (Zoback, 1992; Heidbach et al., 2018). At intermediate scales ( $\sim 500$ – $1500$  km), autocorrelation remains highly significant, indicating organisation that extends beyond individual tectonic belts.

At long wavelengths ( $\sim 2000$ – $4000$  km), Moran’s  $I$  remains positive and significant, though reduced in magnitude. The persistence of coherence at these scales demonstrates a finite but large correlation length approaching near-hemispheric extents, implying that agreement and disagreement between model and observation are not spatially random, even where global mean alignment remains non-diagnostic.

## 8.3 Interpretation of Spatial Organisation in Context

The coexistence of non-diagnostic global mean misfit and statistically significant spatial organisation confirms that these metrics diagnose different aspects of model behaviour (cf. Stephan, 2023). The spatial results do not imply that the modeled shear field is the dominant or sole control on stress orientation; rather, they indicate that the locations where the model aligns (or misaligns) with observations form geographically structured domains that are unlikely to arise under spatial randomness.

This interpretation is consistent with prior evidence that both regional tectonics and longer-wavelength processes contribute to stress orientation and structural organisation (e.g. Zoback, 1992; Cao et al., 2021). Here, spatial statistics provide complementary information by demonstrating that the misfit field itself contains multi-scale geographic structure.

## 8.4 Geographical Coherence and Cross-Scale Consistency

Low-misfit domains occur along several major tectonic belts and intracontinental regions, while high-misfit domains form equally coherent geographic clusters. These domains frequently extend



across plate boundaries and, in some cases, across ocean–continent transitions, reflecting organisation at scales larger than individual plate segments. The emergence of such domains parallels earlier observations of regional to continental coherence in stress orientation patterns (Heidbach et al., 2018; Stephan, 2023), but is here expressed in the misfit field rather than in the stress field itself.

The same areas that exhibit organised misfit structure commonly coincide with regions in which large-scale geological curvature aligns with one of the two modeled shear families or with invariant-contour domains. Although qualitative geometric correspondence and spatial-statistical behaviour are assessed independently, their recurrence in similar regions provides convergent—not causal—support for the hypothesis of long-wavelength structural organisation.

## 8.5 Summary of Statistical Findings

The spatial statistical results lead to four principal conclusions:

1. The modeled geometry does not outperform Euler-rotated null ensembles in terms of global mean angular misfit, consistent with prior observations that scalar misfit alone is insufficient to diagnose stress-field correspondence (Cao et al., 2021).
2. The misfit field nevertheless exhibits statistically significant, scale-dependent spatial organisation across regional to near-hemispheric wavelengths under permutation-based testing (following Cliff and Ord, 1981).
3. The smooth decay of Moran’s  $I$  with increasing scale indicates a finite but large correlation length rather than purely local clustering or random variation.
4. These results are consistent with a hierarchical interpretation in which regional tectonic processes interact with a superimposed long-wavelength organising framework, without implying a unique causal mechanism.

In line with the reviewer’s guidance, these findings are interpreted conservatively: the detection of spatial organisation demonstrates that the misfit field is geographically structured and therefore empirically meaningful, but it does not, by itself, identify the physical origin of that structure. The implications of this behaviour are evaluated further in the Discussion and through the falsifiable predictions outlined in Section 9.

## 8.6 Implications

Taken together, the statistical outcomes demonstrate that the modeled shear framework is not merely visually compatible with geological curvature, but also exhibits quantifiable spatial organisation across scales and regions. The recurring presence of structured wavelength responses and elevated spatial clustering in geologically expressive domains is consistent with a planetary-scale

stress topology acting in concert with local tectonic and material processes, rather than an artifact of geometric overlay or chance alignment.

## 9 Testable Predictions

The results presented above demonstrate that the spatial distribution of stress–orientation misfit is non-random and exhibits coherent organisation across multiple spatial scales, even though the modeled shear field does not improve global mean misfit relative to Euler-rotated null ensembles. These findings support the interpretation that a long-wavelength shear topology may act as an organising framework that interacts with, rather than replaces, regional tectonic processes.

However, the reviewer’s concern rightly emphasises that demonstrating spatial organisation is inherently easier than demonstrating causation. To move the framework from interpretive consistency toward empirical evaluation, we articulate here a series of explicit, falsifiable predictions that follow from the hypothesis. These predictions define avenues for independent testing and provide criteria under which the hypothesis may be supported, refined, or rejected.

### 9.1 Prediction 1: Stability of Misfit Domains Under Dataset Expansion

If the spatial organisation identified in the misfit field reflects a real, long-wavelength component of the stress topology, then coherent misfit domains should remain stable under expansion of the WSM dataset.

**Prediction:** As additional stress observations are incorporated (either geographically or temporally), the geographic boundaries of major low- and high-misfit domains should remain statistically similar, with domain-scale structure persisting even as local values fluctuate.

**Potential falsifier:** If the incorporation of new data systematically erodes domain coherence or causes spatial autocorrelation to collapse toward randomness, the inferred long-wavelength organisation would be weakened.

### 9.2 Prediction 2: Cross-Model Consistency of Spatial Organisation

The hypothesis implies that spatial organisation arises from geometry rather than from a specific stress magnitude distribution.

**Prediction:** When the same statistical analysis is applied to alternative, independently derived global stress models (e.g., numerical or geodynamic models), non-random misfit organisation should recur preferentially in regions predicted to lie near the same shear trajectories or invariant-contour domains.

**Potential falsifier:** If alternative stress models exhibit spatial organisation in wholly unrelated regions, or if organisation disappears altogether when using independent predictions, the geometric hypothesis would be weakened.

### 9.3 Prediction 3: Alignment Bias in Newly Forming or Reactivating Structures

If the shear topology reflects a persistent organising framework, then newly forming or reactivated structures should tend, on average, to align with one of the two shear families.

**Prediction:** Orientation statistics for young fault systems, volcanic chains, and rift segments that postdate major pre-existing fabrics should show directional bias toward Net 1/Net 2 alignment more frequently than expected under random orientation.

**Potential falsifier:** If young or recently initiated structures exhibit no preferential alignment with the predicted shear trajectories, the inferred organising role would be undermined.

### 9.4 Prediction 4: Scaling Consistency Across Independent Geometric Proxies

The hypothesis implies that the same long-wavelength organisation should be observable across independent geometric proxies.

**Prediction:** Regions exhibiting low misfit and shear-aligned curvature in one domain (e.g., rift geometry) should, more often than random expectation, exhibit similar alignment in independent datasets (e.g., gravity-gradient fabrics, bathymetric curvature, glacial excavation patterns).

**Potential falsifier:** If cross-domain correspondence systematically fails or appears only sporadically without scale consistency, the explanatory value of a persistent shear topology diminishes.

### 9.5 Prediction 5: Local–Global Interaction Rather Than Global Uniformity

The framework predicts interaction rather than dominance: local tectonics should remain necessary to express deformation.

**Prediction:** Along-strike variations in curvature and misfit should correlate with transitions in local boundary conditions *while* retaining long-wavelength domain coherence, reflecting superposition rather than replacement of local processes.

**Potential falsifier:** If curvature and misfit behaviour can be fully explained by local processes alone without residual long-wavelength structure, the added value of the global shear framework would not be supported.

## 9.6 Prediction 6: Forward-Simulation Replicability

Finally, the hypothesis implies that the observed spatial structure should be reproducible in forward simulations.

**Prediction:** When simple rheological lithosphere models are subjected to forcing that follows the prescribed shear topology, the resulting deformation fields should reproduce spatially coherent domains comparable in scale and orientation to those observed.

**Potential falsifier:** If forward models fail to produce domain-scale organisation under a wide range of plausible rheologies and boundary conditions, the geometric hypothesis would require revision.

## 9.7 Summary and Implications

These predictions do not assume a unique causal mechanism for the inferred shear topology; rather, they define conditions under which the hypothesis gains or loses empirical support. The framework is therefore intentionally conservative: it does not claim causation, but it does make *testable claims* about geometric and statistical behaviour that can be evaluated against new data, independent models, and forward simulations.

# 10 Synthesis and Discussion

## 10.1 Spatial Organisation Versus Causal Interpretation

The results presented in this study demonstrate that the angular misfit between observed stress orientations and an analytically prescribed global shear field is not spatially random. Instead, the misfit field exhibits statistically significant, scale-dependent spatial organisation from regional to near-hemispheric wavelengths, even though the model does not reduce global mean angular misfit relative to Euler-rotated null ensembles.

This outcome reinforces a central conceptual point: global alignment and spatial organisation diagnose different aspects of model behaviour. The lack of improvement in global mean misfit indicates that the modeled geometry does not act as a globally optimal directional predictor of stress orientation. At the same time, the persistence of spatial autocorrelation shows that the regions of agreement and disagreement are geographically structured in a manner that is unlikely to arise from stochastic variation alone. In other words, the model does not *fit everywhere*, but where it does fit or misfit, those tendencies are spatially organised and scale-consistent.

Consistent with the reviewer’s concern, we emphasise that the presence of spatial organisation is not, by itself, evidence of causation. The analyses presented here do not claim to identify a unique physical mechanism, nor do they require that true polar wander be the direct driver of the inferred shear topology. Rather, the results support a more conservative interpretation: that the geometry implied by the prescribed rotational framework captures a long-wavelength organising structure



that is detectable in both stress-orientation statistics and the curvature of major geological and geomorphic systems.

## 10.2 Interaction Between Local Processes and Long-Wavelength Organisation

The regional case studies show that geometric correspondence between the shear trajectories and Earth-surface features is most clearly expressed where the modeled field predicts low-variance shear geometry or convergence between the two shear families. However, in every example, local and regional processes remain necessary to produce the observed structures. Orogenic loading, rifting, slab rollback, glaciation, sediment routing, and mantle upwelling supply the energetic forcing through which deformation is expressed.

Within this framework, the long-wavelength shear topology acts not as a substitute for plate-tectonic or surface processes, but as a geometric constraint that biases the orientation, curvature, and persistence of structures generated by them. This interpretation helps reconcile several recurring observational patterns documented across the examples in this study:

- large-radius curvature that persists across contrasting lithospheric provinces and tectonic episodes;
- directional bimodality consistent with alternating alignment to two conjugate shear families;
- continuity of curvature and segmentation across plate boundaries and ocean–continent transitions; and
- repeated reactivation of shear-aligned corridors through multiple geological cycles.

These behaviours are difficult to explain solely through local kinematics or inheritance, but are consistent with deformation and landscape evolution unfolding within a persistent, planet-scale stress architecture.

## 10.3 Scale Hierarchy and Correlation Length

The smooth decay of Moran’s  $I$  with increasing spatial scale indicates a finite but large correlation length for misfit organisation. Short-wavelength clustering reflects regional tectonics and lithospheric structure, whereas long-wavelength coherence suggests the presence of a low-degree organising mode that spans multiple tectonic domains. The absence of an abrupt transition between these regimes implies hierarchical interaction rather than a dichotomy between local and global control.

This scale-hierarchical behaviour mirrors the qualitative observations: curvature stability, arcuate segmentation, and directional alternation recur at nested wavelengths, from rift segments and continental arcs to ocean-basin fabrics and near-hemispheric structural sweeps. The coexistence of local variability with large-scale coherence is therefore interpreted as a signature of superposition rather than dominance.

## 10.4 Alternative Explanations and Model Limitations

Several alternative explanations remain plausible and must be considered. Long-wavelength organisation in the misfit field could arise in part from (i) large-scale mantle-flow patterns, (ii) continent-scale rheological contrasts, (iii) plate-boundary network geometry, or (iv) spatial sampling properties of the WSM dataset. Although permutation-based testing mitigates sampling artefacts, the present analysis does not isolate the relative contributions of these processes.

Furthermore, the prescribed rotational geometry represents only one member of a broader class of possible long-wavelength stress fields. Different rotation magnitudes, pole positions, or kinematic formulations may yield alternative shear topologies with similar or improved spatial organisation. The present model should therefore be viewed as a generative hypothesis rather than a unique solution.

Finally, the qualitative comparisons between shear trajectories and geological curvature, while systematic, remain interpretive. Visual congruence does not guarantee mechanical linkage, and future work should replace qualitative comparison with quantitative geometric metrics and forward-model validation.

## 10.5 Implications for Future Work

The new *Testable Predictions* outlined in Section 9 establish a pathway for advancing the hypothesis from interpretive consistency toward empirical discrimination. In particular, three priorities emerge:

1. **Cross-model evaluation:** repeating the spatial-statistical analysis using independent global stress models to test whether spatial organisation recurs in similar geographic domains.
2. **Temporal and dataset growth tests:** evaluating whether misfit domains remain stable as new stress observations are added or as regional data density increases.
3. **Forward simulations:** examining whether simple rheological lithosphere models subjected to shear-topology forcing reproduce domain-scale spatial structures comparable to those observed.

Together, these avenues convert the present framework from a descriptive alignment exercise into a predictive, falsifiable research programme.

## 10.6 Synthesis

In synthesis, the results indicate that Earth’s deformation and surface geometry are plausibly organised within a persistent, long-wavelength shear framework that interacts with regional tectonic processes rather than replacing them. The statistical evidence for scale-dependent spatial organisation, combined with recurring geometric correspondence across diverse geological contexts, suggests that the modeled topology captures a meaningful component of Earth’s stress architecture.

At the same time, the interpretation is intentionally conservative: the work demonstrates spatial organisation, not causation. The hypothesis remains open to refinement, rejection, or replacement through the empirical tests identified in Section 9. The value of the framework lies not in asserting a singular mechanism, but in providing a coherent, testable basis for investigating how long-wavelength stress organisation may shape the curvature, segmentation, and spatial hierarchy of geological structures across the planet.

## 11 Conclusions

This study evaluates whether a mathematically prescribed, planet-scale shear topology derived from an idealised TPW-like rotational geometry produces detectable correspondence with observed stress orientations and large-scale geological curvature. The analysis distinguishes explicitly between two diagnostic questions: (i) whether the modeled field improves global mean angular alignment relative to Euler-rotated null ensembles, and (ii) whether the spatial distribution of stress-orientation misfit exhibits statistically significant geographic organisation across multiple spatial scales.

The results show that the modeled geometry does not outperform randomly rotated reference fields in terms of global mean misfit, consistent with earlier findings that scalar misfit statistics alone provide limited diagnostic power when comparing stress models to observations (e.g. Cao et al., 2021; Stephan, 2023). However, permutation-based spatial autocorrelation analysis demonstrates that the misfit field exhibits significant, scale-dependent spatial organisation from regional to near-hemispheric wavelengths (following Cliff and Ord, 1981). These findings confirm that global alignment and spatial organisation quantify different aspects of model performance, and that spatial structure may be present even where average misfit remains non-diagnostic.

Qualitative comparison across a wide range of tectonic, geomorphic, and passive-margin systems shows that large-radius curvature, directional bimodality, and structural persistence occur preferentially in regions where the modeled field predicts coherent shear geometry. These correspondences are interpreted as convergent geometric signals rather than causal demonstrations: local and regional processes such as convergence, rifting, magmatism, glaciation, and sediment routing remain essential to the formation and evolution of the examined systems (e.g. Zoback, 1992; Heidbach et al., 2018). In this framework, the long-wavelength shear topology is understood as an organising environment that interacts with, rather than replaces, plate-tectonic and surface processes.

A key limitation of the present work is that demonstrating spatial organisation is inherently easier than demonstrating causation. The analyses do not identify a unique physical mechanism for the inferred shear topology and do not require that true polar wander be the sole or necessary driver. The contribution of this study is therefore geometric and statistical rather than mechanistic: it shows that a simple, analytically prescribed shear framework produces empirically testable spatial signals that are detectable in both stress-orientation statistics and surface curvature.

The *Testable Predictions* outlined in Section 9 define a pathway by which the hypothesis ad-

vanced here may be strengthened, refined, or rejected. In particular, future work should (i) evaluate whether spatial organisation persists when applied to independent global stress models, (ii) test the stability of misfit domains as the WSM dataset expands, and (iii) assess whether forward geodynamic simulations subjected to similar long-wavelength forcing reproduce domain-scale spatial structures comparable to those observed. These steps will enable the transition from interpretive consistency toward empirical model discrimination.

In summary, the results support the interpretation that Earth’s deformation and surface geometry may be influenced by a persistent, long-wavelength stress topology that interacts with regional tectonic processes across a hierarchy of spatial scales. While the physical origin of this topology remains open, the evidence presented here demonstrates that its geometric expression is statistically resolvable, internally consistent, and sufficiently structured to justify continued investigation through independent datasets, alternative formulations, and predictive testing.

## 12 Acknowledgments

*The author acknowledges the use of several large-language-model tools (including GPT-5.2, Grok-4.1, Nemotron, LLaMA/Scout, and Claude) in supporting roles during the development of this work. These systems assisted with code drafting and debugging, editorial refinement, conceptual clarification, and “red-teaming” of the analysis and interpretations (i.e., probing assumptions, testing alternative framings, and identifying potential weaknesses). All empirical analyses, statistical procedures, data processing, model implementation, and scientific interpretation were designed, executed, and validated directly by the author, and were not performed autonomously by any AI system.*

## References

- Vening Meinesz, F. A. (1947). Shear patterns of the Earth’s crust. *Eos, Transactions of the American Geophysical Union*.
- The Ethical Skeptic (2024). *Exothermic Core-Mantle Decoupling Dzhani-bekov Oscillation (ECDO) Hypothesis*. Available at: <https://theethicalskeptic.com/2024/05/12/exothermic-core-mantle-decoupling-dzhanibekov-oscillation-ecdo-hypothesis/>.
- Goldreich, P., and Toomre, A. (1969). Some remarks on polar wandering. *Journal of Geophysical Research*, 74, 2555–2567.
- Tsai, V. C., and Stevenson, D. J. (2007). Theoretical constraints on true polar wander: Effects of mantle viscosity structure. *Journal of Geophysical Research*, 112, B05415.
- Turcotte, D. L., and Schubert, G. (2014). *Geodynamics*. Cambridge University Press.
- Condie, K. C. (1997). *Plate Tectonics and Crustal Evolution*. Butterworth–Heinemann.



- Zoback, M. L., Zoback, M. D., Adams, J., Assumpção, M., Bell, S., Bergman, E. A., et al. (1989). Global patterns of tectonic stress. *Nature*, 341, 291–298.
- Zoback, M. L. (1992). First- and second-order patterns of stress in the lithosphere. *Journal of Geophysical Research*, 97(B8), 11703–11728.
- Heidbach, O., Rajabi, M., Reiter, K., Ziegler, M., and the WSM Team (2018). Crustal stress pattern across scales based on the World Stress Map database release 2016. *Tectonophysics*, 744, 484–498.
- Sperner, B., Müller, B., Heidbach, O., Delvaux, D., and Reinecker, J. (2003). Tectonic stress in the Earth’s crust: Advances in the World Stress Map project. *Geological Society Special Publication*, 212, 101–116.
- Zang, A., and Stephansson, O. (2010). *Stress Field of the Earth’s Crust*. Springer.
- Lundstern, J. E. (2020). Multiscale variations of the crustal stress field throughout the lithosphere. *Earth-Science Reviews*, 210, 103355.
- Stephan, T. (2023). Analyzing the horizontal orientation of the crustal stress field. *Scientific Reports*, 13, 15421.
- Delvaux, D., Moeys, R., Stapel, G., Petit, C., Levi, K., Miroshnichenko, A., Ruzhich, V., and San’kov, V. (1995). Paleostress reconstructions and geodynamics of the Baikal region. *Tectonophysics*, 252, 61–101.
- Saintot, A., Angelier, J., Bergerat, F., Bellier, O., Sassi, W., and Pascal, C. (2003). Paleostress field reconstruction and tectonic evolution at the scale of a plate boundary. *Tectonics*, 22(1), 1007.
- Delvaux, D., and Barth, A. (2012). Paleostress reconstruction and active stress fields in intracontinental settings. *Journal of Structural Geology*, 43, 33–51.
- Ali, S. M., Mahajan, S., Rastogi, B., and Singh, A. K. (2021). Tectonic stress regime and stress patterns from the inversion of earthquake focal mechanisms. *Journal of Geodynamics*, 146, 101865.
- Ping, G., Wang, Y., Li, S., and Zhang, F. (2022). Slip-tendency-based stress inversion from 3D seismic reflection data. *Frontiers in Earth Science*, 10, 812874.
- Liu, C., Hu, J., Chen, Y., and Zhang, H. (2023). Present-day stress field constraints in subduction-zone environments from focal mechanisms. *Frontiers in Earth Science*, 10, 1017632.
- Cao, Z., Li, Q., Liu, M., and Zhu, S. (2021). Origin of three-dimensional crustal stress over the globe: 3-D finite-element modelling. *Journal of Geophysical Research: Solid Earth*, 126(11), e2021JB022137.

- Bada, G., Cloetingh, S., Gerner, P., and Horváth, F. (2007). Present-day stress field and tectonic inversion in the Pannonian Basin. *Tectonophysics*, 410, 1–32.
- Palano, M., Aïfa, T., Greco, F., Imprescia, P., and D’Agostino, N. (2015). On the present-day crustal stress–strain-rate fields and mantle anisotropy pattern of Italy. *Geophysical Journal International*, 200, 699–718.
- Ebinger, C. J. (1989). Tectonic development of the western branch of the East African Rift. *Geological Society of America Bulletin*, 101, 885–903.
- Taylor, B., Ebinger, C., d’Almeida, R., et al. (2013). The structure and evolution of the East African Rift System. *Tectonics*, 32, 1–17.
- Corti, G. (2009). Continental rift evolution: From rift initiation to incipient break-up in the East African Rift. *Earth-Science Reviews*, 96, 1–53.
- Philippon, M., and Corti, G. (2015). Obliquity along continental rifts and transfer zones. *Earth-Science Reviews*, 141, 97–133.
- Hoffman, P. F. (1988). United plates of America, the birth of Laurentia. *Annual Review of Earth and Planetary Sciences*, 16, 543–603.
- Dyke, A. S., Moore, A., and Robertson, L. (2004). Deglaciation of North America. *Geological Survey of Canada Open File*, 1574.
- Andrews, J. T., and Peltier, W. R. (1970). Crustal response to loading by the Laurentide Ice Sheet. *Geology*, 18, 102–106.
- Percival, J. A., Cook, F. A., and Clowes, R. M. (2012). Tectonic evolution of the Canadian Shield. *Canadian Journal of Earth Sciences*, 49, 1177–1193.
- Doré, A. G., Lundin, E. R., Jensen, L. N., et al. (2002). Principal tectonic events in the evolution of the northwest European Atlantic margin. *Geological Society Special Publication*, 196, 1–26.
- Eagles, G., and Scott, D. (2004). Plate convergence west of Patagonia and the Antarctic Peninsula since 61 Ma. *Tectonics*, 23, TC1017.
- Buck, W. R. (2015). Rifting processes and passive margin formation. *Geological Society Special Publication*, 413, 1–27.
- Parsons, B., and Sclater, J. G. (1977). An analysis of the variation of ocean floor bathymetry and heat flow with age. *Journal of Geophysical Research*, 82, 803–827.
- Macdonald, K. C. (1984). Mid-ocean ridges: Fine-scale tectonic, volcanic and hydrothermal processes. *Annual Review of Earth and Planetary Sciences*, 12, 359–399.

- Ballantyne, C. K. (2002). The Quaternary glaciation of Scotland. *Quaternary Science Reviews*, 21, 89–136.
- Woodcock, N. H., and Strachan, R. A. (2014). *Geological History of Britain and Ireland*. Wiley-Blackwell.
- Phillips, E., Auton, C., and Rijdsdijk, K. (2016). Reactivation of basement lineaments in glaciated terrains. *Journal of Structural Geology*, 89, 203–219.
- Johnson, S. E. (1997). Reactivation of Precambrian shear zones. *Journal of the Geological Society*, 154, 1–4.
- Cliff, A. D., and Ord, J. K. (1981). *Spatial Processes: Models and Applications*. Pion.
- Fortin, M.-J., and Dale, M. (2005). *Spatial Analysis: A Guide for Ecologists*. Cambridge University Press.
- Hamilton, W. (1979). *Tectonics of the Indonesian Region*. U.S. Geological Survey Professional Paper 1078.
- Hall, R. (2012). Late Jurassic–Cenozoic reconstructions of SE Asia. *Journal of Asian Earth Sciences*, 44, 1–41.
- Rosencrantz, E., Ross, M. I., and Sclater, J. G. (1990). Age and spreading history of the Cayman Trough. *Journal of Geophysical Research*, 95, 15429–15456.

## A Mathematical Appendix: Derivation of the Global Shear Field

### A.1 Rotation Geometry and Coordinate Transformation

Let  $(\phi, \lambda)$  denote geographic latitude and longitude on the unit sphere. The prescribed true-polar-wander-like transformation is implemented as a rigid-body rotation through angle  $\Theta$  about an axis defined by pole coordinates  $(\phi_p, \lambda_p)$ .

The position vector in Cartesian form is

$$\mathbf{x} = \begin{bmatrix} \cos \phi \cos \lambda \\ \cos \phi \sin \lambda \\ \sin \phi \end{bmatrix}.$$

The rotation axis unit vector is

$$\mathbf{k} = \begin{bmatrix} \cos \phi_p \cos \lambda_p \\ \cos \phi_p \sin \lambda_p \\ \sin \phi_p \end{bmatrix}.$$

The rotated position is obtained using Rodrigues' rotation formula:

$$\mathbf{x}' = \mathbf{x} \cos \Theta + (\mathbf{k} \times \mathbf{x}) \sin \Theta + \mathbf{k}(\mathbf{k} \cdot \mathbf{x})(1 - \cos \Theta).$$

## A.2 Surface Velocity and Shear Directions

The instantaneous surface velocity associated with the rotation is

$$\mathbf{v} = \boldsymbol{\Omega} \times \mathbf{x}, \quad \boldsymbol{\Omega} = \Theta \mathbf{k},$$

which lies tangential to the sphere.

Projecting into the local tangent basis  $\{\hat{\mathbf{e}}_\phi, \hat{\mathbf{e}}_\lambda\}$  gives

$$v_\phi = \mathbf{v} \cdot \hat{\mathbf{e}}_\phi, \quad v_\lambda = \mathbf{v} \cdot \hat{\mathbf{e}}_\lambda.$$

The local velocity-gradient tensor on the surface is

$$\mathbf{L} = \begin{bmatrix} \partial v_\phi / \partial \phi & \partial v_\phi / \partial \lambda \\ \partial v_\lambda / \partial \phi & \partial v_\lambda / \partial \lambda \end{bmatrix}, \quad \mathbf{D} = \frac{1}{2}(\mathbf{L} + \mathbf{L}^T),$$

where  $\mathbf{D}$  is the symmetric strain-rate tensor.

## A.3 Principal Shear Trajectories

The principal directions of  $\mathbf{D}$  define the conjugate shear families. Let

$$\mathbf{D} \mathbf{e}_i = \sigma_i \mathbf{e}_i, \quad i = 1, 2,$$

with  $\sigma_1 \geq \sigma_2$ .

Then

- Net 1 trajectories follow the integral curves of  $\mathbf{e}_1$ , - Net 2 trajectories follow those of  $\mathbf{e}_2$ .

Invariant-contour loci are defined where the shear differential vanishes:

$$|\sigma_1 - \sigma_2| \rightarrow \min.$$

Trajectories are traced numerically as great-circle-consistent streamlines of  $\mathbf{e}_i$  on the sphere using adaptive step integration of the tangent-plane directions.



## A.4 Angular Misfit with WSM Orientations

Given a measured horizontal stress azimuth  $\theta_s$  and modeled shear direction  $\theta_m$  at location  $x$ , the unsigned angular misfit is

$$\Delta\theta = \min(|\theta_s - \theta_m|, 180^\circ - |\theta_s - \theta_m|),$$

and the field misfit is evaluated as

$$\Delta\theta_{\min} = \min(\Delta\theta_{\text{Net1}}, \Delta\theta_{\text{Net2}}).$$

This quantity forms the scalar field used in the spatial-autocorrelation analysis described in the Methods.

## B Source

code, figures and data 103.6MB

<https://nobulart.com/media/shear.zip>

shear-map.py

---

```
1  #!/usr/bin/env python3
2  import numpy as np
3  import matplotlib.pyplot as plt
4  import cartopy.crs as ccrs
5  import cartopy.feature as cfeature
6
7  # -----
8  # 1. Regular lat/lon grid (even spacing!)
9  # -----
10 lon = np.linspace(-180, 180, 721)
11 lat = np.linspace(-80, 80, 321) # Mercator-safe
12 LON, LAT = np.meshgrid(lon, lat)
13
14 lon_r = np.deg2rad(LON)
15 lat_r = np.deg2rad(LAT)
16
17 # -----
18 # 2. TPW specification
```

```

19  # -----
20  tpw_lon = np.deg2rad(31.0)
21  tpw_angle = np.deg2rad(104.0)
22
23  # Initial and final pole
24  lat_p0, lon_p0 = np.pi / 2, 0.0
25  lat_p1, lon_p1 = lat_p0 - tpw_angle, tpw_lon
26
27  # -----
28  # 3. Angular distance function
29  # -----
30  def angular_distance(lat_p, lon_p):
31      return np.arccos(
32          np.sin(lat_r) * np.sin(lat_p)
33          + np.cos(lat_r) * np.cos(lat_p) * np.cos(lon_r - lon_p)
34      )
35
36  psi0 = angular_distance(lat_p0, lon_p0)
37  psi1 = angular_distance(lat_p1, lon_p1)
38
39  # -----
40  # 4. Differential centrifugal potential
41  # -----
42  delta_V = np.sin(psi1)**2 - np.sin(psi0)**2
43
44  # -----
45  # 5. Gradients (stress proxy)
46  # -----
47  dV_dlat, dV_dlon = np.gradient(
48      delta_V,
49      np.deg2rad(lat[1] - lat[0]),
50      np.deg2rad(lon[1] - lon[0])
51  )
52
53  theta = np.arctan2(dV_dlon, dV_dlat)
54
55  # Conjugate shear directions
56  shear1 = theta + np.pi / 4
57  shear2 = theta - np.pi / 4

```

```

58
59 # Vector components in lat/lon space
60 U1, V1 = np.cos(shear1), np.sin(shear1)
61 U2, V2 = np.cos(shear2), np.sin(shear2)
62
63 # Shear magnitude proxy
64 shear_mag = np.hypot(dV_dlat, dV_dlon)
65
66 # -----
67 # 6. Plot (Mercator via Cartopy)
68 # -----
69 fig = plt.figure(figsize=(16, 8))
70 ax = plt.axes(projection=ccrs.Mercator())
71
72 ax.set_global()
73 ax.coastlines(linewidth=0.8)
74 ax.add_feature(cfeature.BORDERS, linewidth=0.4)
75
76 # Net 1
77 ax.streamplot(
78     lon, lat, U1, V1,
79     transform=ccrs.PlateCarree(),
80     density=1.2,
81     linewidth=0.7,
82     color="black"
83 )
84
85 # Net 2 (conjugate family { thinner, gray})
86 ax.streamplot(
87     lon, lat, U2, V2,
88     transform=ccrs.PlateCarree(),
89     density=1.2,
90     linewidth=0.4,
91     color="dimgray"
92 )
93
94
95 # Invariant contours (low shear)
96 levels = np.percentile(shear_mag, [5, 10])

```

```

97  ax.contour(
98      lon, lat, shear_mag,
99      levels=levels,
100     colors="red",
101     linewidths=2,
102     transform=ccrs.PlateCarree()
103 )
104
105 # TPW meridian band
106 for m in [30, 32]:
107     ax.plot(
108         [m, m], [-80, 80],
109         transform=ccrs.PlateCarree(),
110         color="gray",
111         linestyle=":"
112     )
113
114 ax.set_title(
115     "Vening Meinesz{Style Shear Pattern\n"
116     "104° True Polar Wander northward along 30{32°E\n"
117     "Net 1 (solid), Net 2 (dashed), Invariant contours (red)",
118     fontsize=12
119 )
120
121 plt.tight_layout()
122 plt.show()

```

---

## shear-kml.py

---

```

1  #!/usr/bin/env python3
2  import numpy as np
3  import matplotlib.pyplot as plt
4  import simplekml
5
6  # =====
7  # 1. Regular lat/lon grid (Plate Carrée, GIS-safe)
8  # =====
9  lon = np.linspace(-180, 180, 721)
10 lat = np.linspace(-80, 80, 321)

```



```

11 LON, LAT = np.meshgrid(lon, lat)
12
13 lon_r = np.deg2rad(LON)
14 lat_r = np.deg2rad(LAT)
15
16 # =====
17 # 2. TPW specification (FIXED: 31°E only)
18 # =====
19 tpw_lon = np.deg2rad(31.0)
20 tpw_angle = np.deg2rad(104.0)
21
22 lat_p0, lon_p0 = np.pi / 2, 0.0
23 lat_p1, lon_p1 = lat_p0 - tpw_angle, tpw_lon
24
25 # =====
26 # 3. Angular distance to pole
27 # =====
28 def angular_distance(lat_p, lon_p):
29     return np.arccos(
30         np.sin(lat_r) * np.sin(lat_p)
31         + np.cos(lat_r) * np.cos(lat_p) * np.cos(lon_r - lon_p)
32     )
33
34 psi0 = angular_distance(lat_p0, lon_p0)
35 psi1 = angular_distance(lat_p1, lon_p1)
36
37 # =====
38 # 4. Differential centrifugal potential
39 # =====
40 delta_V = np.sin(psi1)**2 - np.sin(psi0)**2
41
42 # =====
43 # 5. Surface gradients (stress proxy)
44 # =====
45 dlat = np.deg2rad(lat[1] - lat[0])
46 dlon = np.deg2rad(lon[1] - lon[0])
47
48 dV_dlat, dV_dlon = np.gradient(delta_V, dlat, dlon)
49 shear_mag = np.hypot(dV_dlat, dV_dlon)

```

```

50
51 # =====
52 # 6. Principal stress & conjugate shear directions
53 # =====
54 theta = np.arctan2(dV_dlon, dV_dlat)
55
56 shear1 = theta + np.pi / 4
57 shear2 = theta - np.pi / 4
58
59 U1, V1 = np.cos(shear1), np.sin(shear1)
60 U2, V2 = np.cos(shear2), np.sin(shear2)
61
62 # =====
63 # 7. Invariant (low-shear) contours
64 # =====
65 levels = np.percentile(shear_mag, [5, 10])
66
67 fig, ax = plt.subplots()
68 CS = ax.contour(lon, lat, shear_mag, levels=levels)
69 plt.close(fig)
70
71 # =====
72 # 8. Streamline integrator (explicit geometry)
73 # =====
74 def integrate_streamline(lon0, lat0, U, V, lon, lat, ds=0.5, nsteps=800):
75     line = []
76     x, y = lon0, lat0
77
78     for _ in range(nsteps):
79         if x < -180 or x > 180 or y < -80 or y > 80:
80             break
81
82         i = np.searchsorted(lon, x) - 1
83         j = np.searchsorted(lat, y) - 1
84
85         if i < 0 or j < 0 or i >= len(lon)-1 or j >= len(lat)-1:
86             break
87
88         u = U[j, i]

```

```

89         v = V[j, i]
90         n = np.hypot(u, v)
91
92         if n == 0:
93             break
94
95         x += ds * u / n
96         y += ds * v / n
97         line.append((float(x), float(y)))
98
99     return line
100
101     # =====
102     # 9. Create KML
103     # =====
104     kml = simplekml.Kml()
105
106     # --- Invariant contours ---
107     inv_folder = kml.newfolder(name="Invariant shear contours")
108
109     for i, level in enumerate(CS.levels):
110         for seg in CS.allsegs[i]:
111             if len(seg) < 20:
112                 continue
113
114             ls = inv_folder.newlinestring(
115                 name=f"Invariant contour ( {level:.2e})"
116             )
117             ls.coords = [(float(x), float(y)) for x, y in seg]
118             ls.style.linestyle.color = simplekml.Color.red
119             ls.style.linestyle.width = 3
120
121     # =====
122     # 10. Net 1 / Net 2 streamlines (50% density reduction)
123     # =====
124     seed_lons = np.arange(-180, 181, 20)    # reduced from 10°
125     seed_lats = np.arange(-70, 71, 20)      # reduced from 10°
126
127     net1 = kml.newfolder(name="Net 1 shear trajectories")

```

```

128 net2 = kml.newfolder(name="Net 2 shear trajectories")
129
130 for lon0 in seed_lons:
131     for lat0 in seed_lats:
132
133         line1 = integrate_streamline(lon0, lat0, U1, V1, lon, lat)
134         if len(line1) > 50:
135             ls = net1.newlinestring()
136             ls.coords = line1
137             ls.style.linestyle.color = simplekml.Color.black
138             ls.style.linestyle.width = 1
139
140         line2 = integrate_streamline(lon0, lat0, U2, V2, lon, lat)
141         if len(line2) > 50:
142             ls = net2.newlinestring()
143             ls.coords = line2
144             ls.style.linestyle.color = simplekml.Color.gray
145             ls.style.linestyle.width = 1
146
147 # =====
148 # 11. TPW reference meridian (31°E)
149 # =====
150 ls = kml.newlinestring(name="TPW meridian 31°E")
151 ls.coords = [(31.0, -80.0), (31.0, 80.0)]
152 ls.style.linestyle.color = simplekml.Color.gray
153 ls.style.linestyle.width = 2
154
155 # =====
156 # 12. Save
157 # =====
158 kml.save("meinesz_shear_full_104deg_31E.kml")
159 print("Saved: meinesz_shear_full_104deg_31E.kml")

```

---

## shear-fit.py

```

1 #!/usr/bin/env python3
2 """
3 shear-fit.py
4

```



```

5  Compute angular misfit between World Stress Map (WSM) stress azimuths
6  and two global shear nets. Persist shear geometry and stress azimuths
7  for downstream Euler-rotation null testing.
8
9  Author: Craig Stone
10 """
11
12 import numpy as np
13 import pandas as pd
14 from pyproj import Geod
15 from scipy.spatial import cKDTree
16 from tqdm import tqdm
17
18 # -----
19 # CONFIGURATION
20 # -----
21
22 WSM_CSV = "WSM_database_2025.csv"
23
24 MAX_MATCH_KM = 200
25 RANDOM_SEED = 42
26
27 QUALITY_WEIGHTS = {
28     "A": 1.0,
29     "B": 0.75,
30     "C": 0.4,
31     "D": 0.2
32 }
33
34 # Euler points for diagnostics (example values)
35 EULER_POINTS = {
36     "West": (5.0, -65.0),
37     "East": (-5.0, 120.0)
38 }
39
40 rng = np.random.default_rng(RANDOM_SEED)
41 geod = Geod(ellps="WGS84")
42
43 # -----

```

```

44  # UTILITY FUNCTIONS
45  # -----
46
47  def angular_misfit(a, b):
48      d = abs(a - b) % 360
49      d = min(d, 360 - d)
50      return min(d, abs(d - 180))
51
52
53  def angular_distance(lat1, lon1, lat2, lon2):
54      _, _, dist = geod.inv(lon1, lat1, lon2, lat2)
55      return dist / 1000.0 / 111.0
56
57
58  # -----
59  # BUILD SHEAR NETS
60  # -----
61  # NOTE: Replace this section ONLY if you already have
62  # a custom shear-net generator. Otherwise this stub
63  # assumes net midpoints + azimuths are already known.
64
65  def build_shear_net():
66      """
67      Placeholder shear-net generator.
68      Replace with your actual net construction logic.
69      Must return:
70          midpoints: (N, 2) array of (lat, lon)
71          azimuths: (N,) azimuths in degrees
72      """
73      lats = np.linspace(-90, 90, 720)
74      lons = np.linspace(-180, 180, 1440)
75      latg, long = np.meshgrid(lats, lons, indexing="ij")
76
77      midpoints = np.column_stack([latg.ravel(), long.ravel()])
78      azimuths = (long.ravel() + 90) % 360
79
80      return midpoints, azimuths
81
82

```

```

83  print("Building shear nets...")
84  net1_midpoints, az1 = build_shear_net()
85  net2_midpoints, az2 = build_shear_net() # replace if different logic
86
87  tree1 = cKDTree(net1_midpoints)
88  tree2 = cKDTree(net2_midpoints)
89
90  # -----
91  # PERSIST NET 2 GEOMETRY (CRITICAL)
92  # -----
93
94  print("Saving Net 2 geometry for Euler-rotation null tests...")
95  np.save("net2_midpoints.npy", net2_midpoints)
96  np.save("net2_azimuths.npy", az2)
97
98  # -----
99  # LOAD AND FILTER WSM
100 # -----
101
102 print("Loading WSM database...")
103 wsm = pd.read_csv(WSM_CSV, low_memory=False)
104
105 required = ["LAT", "LON", "AZI", "REGIME", "QUALITY"]
106 for col in required:
107     if col not in wsm.columns:
108         raise RuntimeError(f"Missing required WSM column: {col}")
109
110 wsm = wsm.dropna(subset=["LAT", "LON", "AZI"])
111 wsm["LAT"] = pd.to_numeric(wsm["LAT"], errors="coerce")
112 wsm["LON"] = pd.to_numeric(wsm["LON"], errors="coerce")
113 wsm["AZI"] = pd.to_numeric(wsm["AZI"], errors="coerce")
114 wsm = wsm.dropna(subset=["LAT", "LON", "AZI"])
115
116 print("Initial WSM rows:", len(wsm))
117
118 # Optional regime filter (recommended)
119 VALID_REGIMES = {"SS", "TF", "TS"}
120 wsm = wsm[wsm["REGIME"].isin(VALID_REGIMES)]
121

```

```

122 print("WSM rows after filtering:", len(wsm))
123
124 # -----
125 # COMPARE TO SHEAR NETS
126 # -----
127
128 results = []
129
130 print("Comparing stress data to shear nets...")
131 for _, row in tqdm(wsm.iterrows(), total=len(wsm)):
132
133     lat = row["LAT"]
134     lon = row["LON"]
135
136     stress_az = row["AZI"] % 360
137     q = row.get("QUALITY", "D")
138     weight = QUALITY_WEIGHTS.get(q, 0.2)
139
140     # Net 1
141     d1, i1 = tree1.query((lat, lon), k=1)
142     if d1 * 111.0 > MAX_MATCH_KM:
143         continue
144     mis1 = angular_misfit(stress_az, az1[i1])
145
146     # Net 2
147     d2, i2 = tree2.query((lat, lon), k=1)
148     if d2 * 111.0 > MAX_MATCH_KM:
149         continue
150     mis2 = angular_misfit(stress_az, az2[i2])
151
152     entry = {
153         "LAT": lat,
154         "LON": lon,
155         "STRESS_AZ": stress_az,      # <-- REQUIRED FOR EULER NULL
156         "NET1_MISFIT": mis1,
157         "NET2_MISFIT": mis2,
158         "WEIGHT": weight,
159         "REGIME": row.get("REGIME"),
160         "QUALITY": q,

```



```

161         "PLATE": row.get("PLATE", None)
162     }
163
164     for name, (elat, elon) in EULER_POINTS.items():
165         entry[f"DIST_{name}"] = angular_distance(lat, lon, elat, elon)
166
167     results.append(entry)
168
169     # -----
170     # OUTPUT
171     # -----
172
173 df = pd.DataFrame(results)
174
175 print("\n=== Weighted summary ===")
176 print("Net 1 weighted mean misfit:",
177       np.average(df["NET1_MISFIT"], weights=df["WEIGHT"]))
178 print("Net 2 weighted mean misfit:",
179       np.average(df["NET2_MISFIT"], weights=df["WEIGHT"]))
180 print("Fraction where Net 1 fits better:",
181       np.mean(df["NET1_MISFIT"] < df["NET2_MISFIT"]))
182
183 df.to_csv("wsm_shear_misfit_filtered.csv", index=False)
184 print("Saved wsm_shear_misfit_filtered.csv")

```

---

## shear-euler.py

---

```

1  #!/usr/bin/env python3
2  """
3  shear_euler.py
4
5  Euler-rotation null test for WSM vs shear-net alignment.
6  Uses precomputed WSM{shear comparison results.
7
8  Author: Craig Stone
9  """
10
11 import numpy as np
12 import pandas as pd

```

```

13 from pyproj import Geod
14 from scipy.spatial import cKDTree
15 from tqdm import tqdm
16
17 # -----
18 # CONFIGURATION
19 # -----
20
21 CSV_INPUT = "wsm_shear_misfit_filtered.csv"
22
23 # Number of Euler-rotation null realizations
24 N_NULL = 500
25
26 # Max allowed distance (km) for shear matching
27 MAX_MATCH_KM = 200
28
29 # Random seed for reproducibility
30 RANDOM_SEED = 42
31
32 rng = np.random.default_rng(RANDOM_SEED)
33 geod = Geod(ellps="WGS84")
34
35 # -----
36 # LOAD DATA
37 # -----
38
39 print("Loading WSM{shear comparison CSV...}")
40 df = pd.read_csv(CSV_INPUT)
41
42 # Ensure required columns
43 required_cols = ["LAT", "LON", "WEIGHT"]
44 for col in required_cols:
45     if col not in df.columns:
46         raise RuntimeError(f"Missing required column: {col}")
47
48 # Stress azimuth handling
49 if "STRESS_AZ" not in df.columns:
50     if "AZI" not in df.columns:
51         raise RuntimeError("Neither STRESS_AZ nor AZI found in CSV")

```

```

52     df["STRESS_AZ"] = df["AZI"] % 360
53
54     # Convert to numeric and drop invalid rows
55     for col in ["LAT", "LON", "WEIGHT", "STRESS_AZ"]:
56         df[col] = pd.to_numeric(df[col], errors="coerce")
57
58     df = df.dropna(subset=["LAT", "LON", "WEIGHT", "STRESS_AZ"])
59
60     print("Rows used for Euler-null test:", len(df))
61
62     # -----
63     # LOAD SHEAR NET MIDPOINTS & AZIMUTHS
64     # (from shear-fit.py output assumptions)
65     # -----
66
67     # These files must be produced during shear-net construction
68     NET2_MIDPOINTS = "net2_midpoints.npy"
69     NET2_AZIMUTHS = "net2_azimuths.npy"
70
71     mp2 = np.load(NET2_MIDPOINTS)    # shape (N, 2) -> (lat, lon)
72     az2 = np.load(NET2_AZIMUTHS)    # shape (N,)
73
74     # -----
75     # EULER ROTATION UTILITIES
76     # -----
77
78     def euler_rotate(lat, lon, pole_lat, pole_lon, angle_deg):
79         """Rotate a point around an Euler pole."""
80         lat, lon = np.radians(lat), np.radians(lon)
81         pole_lat, pole_lon = np.radians(pole_lat), np.radians(pole_lon)
82         angle = np.radians(angle_deg)
83
84         r = np.array([
85             np.cos(lat) * np.cos(lon),
86             np.cos(lat) * np.sin(lon),
87             np.sin(lat)
88         ])
89
90         k = np.array([

```

```

91         np.cos(pole_lat) * np.cos(pole_lon),
92         np.cos(pole_lat) * np.sin(pole_lon),
93         np.sin(pole_lat)
94     ])
95
96     r_rot = (
97         r * np.cos(angle)
98         + np.cross(k, r) * np.sin(angle)
99         + k * np.dot(k, r) * (1 - np.cos(angle))
100    )
101
102    lat_r = np.degrees(np.arcsin(r_rot[2]))
103    lon_r = np.degrees(np.arctan2(r_rot[1], r_rot[0]))
104
105    return lat_r, lon_r
106
107
108    def rotate_azimuth(lat, lon, az, pole_lat, pole_lon, angle_deg, dkm=10):
109        """Rotate an azimuth via a short forward step."""
110        lon2, lat2, _ = geod.fwd(lon, lat, az, dkm * 1000)
111        lat_r1, lon_r1 = euler_rotate(lat, lon, pole_lat, pole_lon, angle_deg)
112        lat_r2, lon_r2 = euler_rotate(lat2, lon2, pole_lat, pole_lon, angle_deg)
113        az_r, _, _ = geod.inv(lon_r1, lat_r1, lon_r2, lat_r2)
114        return az_r % 360
115
116
117    def angular_misfit(a, b):
118        d = abs(a - b) % 360
119        d = min(d, 360 - d)
120        return min(d, abs(d - 180))
121
122
123    # -----
124    # BUILD ROTATED SHEAR INDEX
125    # -----
126
127    def build_rotated_shear(mp, az, pole_lat, pole_lon, angle_deg):
128        rot_pts = []
129        rot_az = []

```

```

130
131     for (lat, lon), a in zip(mp, az):
132         lat_r, lon_r = euler_rotate(lat, lon, pole_lat, pole_lon, angle_deg)
133         az_r = rotate_azimuth(lat, lon, a, pole_lat, pole_lon, angle_deg)
134         rot_pts.append((lat_r, lon_r))
135         rot_az.append(az_r)
136
137     rot_pts = np.array(rot_pts)
138     rot_az = np.array(rot_az)
139
140     return cKDTree(rot_pts), rot_az
141
142
143     # -----
144     # NULL MODEL LOOP
145     # -----
146
147     print(f"Running Euler-rotation null with N = {N_NULL}")
148
149     null_means = []
150
151     for _ in tqdm(range(N_NULL)):
152         pole_lat = rng.uniform(-90, 90)
153         pole_lon = rng.uniform(-180, 180)
154         angle = rng.uniform(0, 360)
155
156         tree_r, az_r = build_rotated_shear(mp2, az2, pole_lat, pole_lon, angle)
157
158         misfits = []
159         weights = []
160
161         for _, row in df.iterrows():
162             lat, lon = row["LAT"], row["LON"]
163             stress_az = row["STRESS_AZ"]
164             w = row["WEIGHT"]
165
166             d, i = tree_r.query((lat, lon), k=1)
167             if d * 111 > MAX_MATCH_KM:
168                 continue

```



```

169
170     m = angular_misfit(stress_az, az_r[i])
171     misfits.append(m)
172     weights.append(w)
173
174     if len(weights) > 0:
175         null_means.append(np.average(misfits, weights=weights))
176
177 null_means = np.array(null_means)
178
179 # -----
180 # SUMMARY
181 # -----
182
183 observed = np.average(
184     np.minimum(df["NET1_MISFIT"], df["NET2_MISFIT"]),
185     weights=df["WEIGHT"]
186 )
187
188 print("\n=== Euler-rotation null summary ===")
189 print("Observed mean misfit:", observed)
190 print("Null mean:", null_means.mean())
191 print("Null std:", null_means.std())
192 print("p-value:", np.mean(null_means <= observed))
193
194 # -----
195 # SAVE ONE REPRESENTATIVE NULL MAP
196 # -----
197
198 print("Saving representative null misfit column...")
199
200 pole_lat, pole_lon, angle = 30, -120, 137
201 tree_r, az_r = build_rotated_shear(mp2, az2, pole_lat, pole_lon, angle)
202
203 null_mis = []
204
205 for _, row in df.iterrows():
206     lat, lon = row["LAT"], row["LON"]
207     stress_az = row["STRESS_AZ"]

```

```

208
209     d, i = tree_r.query((lat, lon), k=1)
210     if d * 111 > MAX_MATCH_KM:
211         null_mis.append(np.nan)
212     else:
213         null_mis.append(angular_misfit(stress_az, az_r[i]))
214
215 df["NULL_MISFIT"] = null_mis
216 df.to_csv("wsm_shear_with_null.csv", index=False)
217
218 print("Saved wsm_shear_with_null.csv")

```

---

### shear-sac-permutation.py

---

```

1  #!/usr/bin/env python3
2  """
3  shear-sac-permutation.py
4
5  Permutation-based Moran's I spatial autocorrelation test
6  for WSM{shear misfit fields.
7
8  Correct null model for scalar spatial statistics.
9
10 Author: Craig Stone
11 """
12
13 import numpy as np
14 import pandas as pd
15 from pyproj import Geod
16 from scipy.spatial import cKDTree
17 from tqdm import tqdm
18
19 # -----
20 # CONFIGURATION
21 # -----
22
23 CSV = "wsm_shear_with_null.csv"
24
25 L_SCALES = [250, 500, 1000, 2000, 3000, 4000]    # km

```

```

26 D_MAX_FACTOR = 3.0
27 N_PERM = 1000                                # permutations per scale
28
29 # -----
30 # LOAD DATA
31 # -----
32
33 df = pd.read_csv(CSV)
34
35 for col in ["LAT", "LON", "NET1_MISFIT", "NET2_MISFIT"]:
36     df[col] = pd.to_numeric(df[col], errors="coerce")
37
38 df = df.dropna(subset=["LAT", "LON", "NET1_MISFIT", "NET2_MISFIT"])
39
40 df["OBS_MISFIT"] = np.minimum(df["NET1_MISFIT"], df["NET2_MISFIT"])
41
42 lat = df["LAT"].values
43 lon = df["LON"].values
44 values_obs = df["OBS_MISFIT"].values
45
46 N = len(df)
47 print(f"Using {N} spatial points")
48
49 # -----
50 # SPATIAL INDEX
51 # -----
52
53 geod = Geod(ellps="WGS84")
54
55 lat_rad = np.radians(lat)
56 lon_rad = np.radians(lon)
57
58 xyz = np.column_stack([
59     np.cos(lat_rad) * np.cos(lon_rad),
60     np.cos(lat_rad) * np.sin(lon_rad),
61     np.sin(lat_rad)
62 ])
63
64 tree = cKDTree(xyz)

```

```

65
66 # -----
67 # PRECOMPUTE NEIGHBORS + WEIGHTS
68 # -----
69
70 def precompute_neighbors_weights(L_km):
71     d_max = D_MAX_FACTOR * L_km
72     radius = d_max / 6371.0 # radians
73
74     neighbors = []
75     weights = []
76
77     for i in tqdm(range(N), desc=f"Precomputing (L={L_km} km)":
78         idx = tree.query_ball_point(xyz[i], r=radius)
79
80         js = []
81         ws = []
82
83         for j in idx:
84             if i == j:
85                 continue
86
87             _, _, d = geod.inv(lon[i], lat[i], lon[j], lat[j])
88             d /= 1000.0
89
90             if d <= d_max:
91                 js.append(j)
92                 ws.append(np.exp(-d / L_km))
93
94             neighbors.append(np.array(js, dtype=np.int32))
95             weights.append(np.array(ws, dtype=np.float32))
96
97     return neighbors, weights
98
99 # -----
100 # MORAN'S I USING PRECOMPUTED WEIGHTS
101 # -----
102
103 def morans_I(values, neighbors, weights):

```

```

104     mean = values.mean()
105     var = np.sum((values - mean) ** 2)
106
107     I_num = 0.0
108     W = 0.0
109
110     for i in range(N):
111         vi = values[i] - mean
112         if vi == 0:
113             continue
114
115         js = neighbors[i]
116         ws = weights[i]
117
118         if len(js) == 0:
119             continue
120
121         vj = values[js] - mean
122         I_num += np.sum(ws * vi * vj)
123         W += np.sum(ws)
124
125     return (N / W) * (I_num / var)
126
127     # -----
128     # MAIN ANALYSIS
129     # -----
130
131     results = []
132
133     print("\nRunning permutation-based Moran's I tests")
134
135     for L in L_SCALES:
136         print(f"\n=== Scale L = {L} km ===")
137
138         neighbors, weights = precompute_neighbors_weights(L)
139
140         # Observed Moran's I
141         I_obs = morans_I(values_obs, neighbors, weights)
142

```



```

143     # Permutation null
144     I_perm = []
145
146     for _ in tqdm(range(N_PERM), desc="Permutations"):
147         permuted = np.random.permutation(values_obs)
148         I_p = morans_I(permuted, neighbors, weights)
149         I_perm.append(I_p)
150
151     I_perm = np.array(I_perm)
152
153     z = (I_obs - I_perm.mean()) / I_perm.std()
154     p = np.mean(I_perm >= I_obs)
155
156     print(f"Observed I: {I_obs:.5f}")
157     print(f"Null mean: {I_perm.mean():.5f}")
158     print(f"Null std: {I_perm.std():.5f}")
159     print(f"z-score: {z:.2f}")
160     print(f"p-value: {p:.5f}")
161
162     results.append({
163         "L_km": L,
164         "I_obs": I_obs,
165         "I_null_mean": I_perm.mean(),
166         "I_null_std": I_perm.std(),
167         "z_score": z,
168         "p_value": p
169     })
170
171     # -----
172     # SAVE RESULTS
173     # -----
174
175     out = pd.DataFrame(results)
176     out.to_csv("spatial_autocorrelation_permutation_results.csv", index=False)
177
178     print("\nSaved spatial_autocorrelation_permutation_results.csv")

```

---

shear-morans.py

---

```

1  #!/usr/bin/env python3
2  """
3  Adaptive, sparse, multiprocessing Moran's I for TPW ensemble stress maps.
4
5  Features:
6  •  $O(N \cdot k)$  sparse neighbor formulation
7  • Disk-cached neighbors (per scale)
8  • Ensemble-safe (per RUN_ID)
9  • Adaptive permutation stopping
10 • Multiprocessing (Apple Silicon safe)
11 • Progress indicators
12 • Ensemble ranking + confidence intervals
13 • TPW geometry metadata preserved in outputs
14 """
15
16 import argparse
17 import os
18 import pickle
19 import numpy as np
20 import pandas as pd
21 from tqdm import tqdm
22 from scipy.spatial import cKDTree
23 import multiprocessing as mp
24
25 EARTH_RADIUS_KM = 6371.0
26
27 # =====
28 # Geometry utilities
29 # =====
30
31 def haversine_km(lat1, lon1, lat2, lon2):
32     lat1, lon1, lat2, lon2 = map(np.radians, [lat1, lon1, lat2, lon2])
33     dlat = lat2 - lat1
34     dlon = lon2 - lon1
35     a = np.sin(dlat/2)**2 + np.cos(lat1)*np.cos(lat2)*np.sin(dlon/2)**2
36     return 2 * EARTH_RADIUS_KM * np.arcsin(np.sqrt(a))
37
38

```

```

39 def build_neighbors(lat, lon, L_km):
40     coords = np.column_stack((lat, lon))
41     tree = cKDTree(coords)
42     neighbors = []
43
44     for i in tqdm(range(len(lat)),
45                   desc=f"Precomputing neighbors (L={int(L_km)} km)":
46         idx = tree.query_ball_point(coords[i], r=L_km / 111.0)
47         idx = [
48             j for j in idx
49             if j != i and haversine_km(lat[i], lon[i], lat[j], lon[j]) <= L_km
50         ]
51         neighbors.append(np.array(idx, dtype=np.int32))
52
53     return neighbors
54
55
56 # =====
57 # Moran's I (sparse)
58 # =====
59
60 def morans_I_sparse(values, neighbors):
61     v = values - values.mean()
62     num = 0.0
63     wsum = 0
64
65     for i, nbrs in enumerate(neighbors):
66         if len(nbrs) == 0:
67             continue
68         num += v[i] * v[nbrs].sum()
69         wsum += len(nbrs)
70
71     den = np.sum(v * v)
72     return (len(values) / wsum) * (num / den)
73
74
75 # =====
76 # Multiprocessing worker state
77 # =====

```

```

78
79 _WORK_VALUES = None
80 _WORK_NEIGHBORS = None
81
82 def _init_worker(values, neighbors):
83     global _WORK_VALUES, _WORK_NEIGHBORS
84     _WORK_VALUES = values
85     _WORK_NEIGHBORS = neighbors
86
87
88 def _perm_moran(seed):
89     rng = np.random.default_rng(seed)
90     perm = rng.permutation(_WORK_VALUES)
91     return morans_I_sparse(perm, _WORK_NEIGHBORS)
92
93
94 # =====
95 # Main
96 # =====
97
98 def main():
99     ap = argparse.ArgumentParser()
100     ap.add_argument("--input", required=True, help="Ensemble CSV")
101     ap.add_argument("--misfit-column", required=True, help="Misfit column name")
102     ap.add_argument("--scales", nargs="+", type=float,
103                     default=[250, 500, 1000, 2000, 4000])
104     ap.add_argument("--alpha", type=float, default=0.01)
105     ap.add_argument("--min-permutations", type=int, default=100)
106     ap.add_argument("--max-permutations", type=int, default=5000)
107     ap.add_argument("--workers", type=int, default=12)
108     ap.add_argument("--cache-dir", default="neighbor_cache")
109     ap.add_argument("--seed", type=int, default=42)
110     ap.add_argument("--output", default="morans_ensemble_results.csv")
111     args = ap.parse_args()
112
113     rng = np.random.default_rng(args.seed)
114     os.makedirs(args.cache_dir, exist_ok=True)
115
116     df = pd.read_csv(args.input)

```

```

117
118     # -----
119     # Required columns
120     # -----
121
122     required = {"RUN_ID", "LAT", "LON", args.misfit_column}
123     missing = required - set(df.columns)
124     if missing:
125         raise RuntimeError(f"Missing required columns: {missing}")
126
127     # -----
128     # Extract TPW metadata per RUN_ID
129     # -----
130
131     TPW_META_FIELDS = ["POLE_LAT", "POLE_LON", "ROT_DEG", "ROT_SIGN"]
132     missing_meta = set(TPW_META_FIELDS) - set(df.columns)
133     if missing_meta:
134         raise RuntimeError(f"Missing TPW metadata columns: {missing_meta}")
135
136     tpw_meta = (
137         df[["RUN_ID"] + TPW_META_FIELDS]
138         .drop_duplicates(subset="RUN_ID")
139         .set_index("RUN_ID")
140     )
141
142     # -----
143     # Geometry (identical across ensemble)
144     # -----
145
146     first_run = df["RUN_ID"].iloc[0]
147     ref = df[df["RUN_ID"] == first_run]
148     lat = ref["LAT"].values
149     lon = ref["LON"].values
150
151     # -----
152     # Neighbor caching
153     # -----
154
155     neighbor_cache = {}

```



```

156     for L in args.scales:
157         cache_file = os.path.join(args.cache_dir, f"neighbors_L{int(L)}.pkl")
158         if os.path.exists(cache_file):
159             print(f"Loading cached neighbors for L={L} km")
160             with open(cache_file, "rb") as f:
161                 neighbor_cache[L] = pickle.load(f)
162         else:
163             nbrs = build_neighbors(lat, lon, L)
164             with open(cache_file, "wb") as f:
165                 pickle.dump(nbrs, f)
166             neighbor_cache[L] = nbrs
167
168     # -----
169     # Moran's I evaluation
170     # -----
171
172     records = []
173     run_groups = list(df.groupby("RUN_ID"))
174     ctx = mp.get_context("spawn")
175
176     for run_id, group in tqdm(run_groups,
177                               desc="Evaluating ensemble members",
178                               unit="run"):
179
180         values = group[args.misfit_column].values
181         meta = tpw_meta.loc[run_id]
182
183         for L in tqdm(args.scales,
184                       desc=f"Scales for {run_id}",
185                       leave=False):
186
187             neighbors = neighbor_cache[L]
188             I_obs = morans_I_sparse(values, neighbors)
189
190             k = 0
191             n = 0
192             null_I = []
193
194             with ctx.Pool(

```

```

195         processes=min(mp.cpu_count(), args.workers),
196         initializer=_init_worker,
197         initargs=(values, neighbors)
198     ) as pool:
199
200         pbar = tqdm(
201             total=args.max_permutations,
202             desc=f"Permutations (L={L} km)",
203             leave=False
204         )
205
206         while n < args.max_permutations:
207
208             batch = min(100, args.max_permutations - n)
209             seeds = rng.integers(0, 2**32 - 1, size=batch)
210             results = pool.map(_perm_moran, seeds)
211
212             for I_null in results:
213                 null_I.append(I_null)
214                 if abs(I_null) >= abs(I_obs):
215                     k += 1
216                 n += 1
217
218             pbar.update(batch)
219
220             if n >= args.min_permutations:
221                 p_hat = (k + 1) / (n + 1)
222                 if p_hat < args.alpha:
223                     break
224
225             pbar.close()
226
227         null_I = np.array(null_I)
228         null_mean = null_I.mean()
229         null_std = null_I.std(ddof=1)
230         z = (I_obs - null_mean) / null_std if null_std > 0 else np.inf
231         pval = (k + 1) / (n + 1)
232
233         records.append({

```

```

234         "RUN_ID": run_id,
235         "POLE_LAT": meta["POLE_LAT"],
236         "POLE_LON": meta["POLE_LON"],
237         "ROT_DEG": meta["ROT_DEG"],
238         "ROT_SIGN": meta["ROT_SIGN"],
239         "SCALE_KM": L,
240         "I_OBS": I_obs,
241         "I_NULL_MEAN": null_mean,
242         "I_NULL_STD": null_std,
243         "Z_SCORE": z,
244         "P_VALUE": pval,
245         "PERMUTATIONS_USED": n
246     })
247
248 results = pd.DataFrame(records)
249 results.to_csv(args.output, index=False)
250
251 # -----
252 # Ensemble ranking + confidence intervals
253 # -----
254
255 summary = (
256     results.groupby("RUN_ID")
257     .agg(
258         MEAN_I=("I_OBS", "mean"),
259         MEDIAN_I=("I_OBS", "median"),
260         I_5P=("I_OBS", lambda x: np.percentile(x, 5)),
261         I_95P=("I_OBS", lambda x: np.percentile(x, 95))
262     )
263     .reset_index()
264     .merge(tpw_meta.reset_index(), on="RUN_ID", how="left")
265     .sort_values("MEAN_I", ascending=False)
266 )
267
268 summary["RANK"] = np.arange(1, len(summary) + 1)
269 summary.to_csv("morans_ensemble_ranking.csv", index=False)
270
271 print("\nSaved:")
272 print(" ●", args.output)

```

```

273     print(" • morans_ensemble_ranking.csv")
274
275
276 if __name__ == "__main__":
277     main()

```

---

## shear-morans-permutations.py

---

```

1  #!/usr/bin/env python3
2  import argparse
3  import os
4  import pickle
5  import numpy as np
6  import pandas as pd
7  from tqdm import tqdm
8  from math import radians, sin, cos
9  from scipy.spatial import cKDTree
10
11 EARTH_RADIUS_KM = 6371.0
12 MIN_POINTS = 500
13
14 # =====
15 # Geometry utilities
16 # =====
17
18 def latlon_to_unit(lat, lon):
19     lat = np.radians(lat)
20     lon = np.radians(lon)
21     return np.column_stack((
22         np.cos(lat) * np.cos(lon),
23         np.cos(lat) * np.sin(lon),
24         np.sin(lat)
25     ))
26
27 def chord_radius(L_km):
28     theta = L_km / EARTH_RADIUS_KM
29     return 2.0 * np.sin(theta / 2.0)
30
31 # =====

```

```

32  # Neighbor construction (cached)
33  # =====
34
35  def build_neighbors(lat, lon, L_km, cache_file):
36      if os.path.exists(cache_file):
37          with open(cache_file, "rb") as f:
38              return pickle.load(f)
39
40      print(f"Precomputing neighbors (L={L_km} km)")
41      xyz = latlon_to_unit(lat, lon)
42      tree = cKDTree(xyz)
43      r = chord_radius(L_km)
44
45      neighbors = []
46      for i in tqdm(range(len(xyz))):
47          idx = tree.query_ball_point(xyz[i], r)
48          idx = [j for j in idx if j != i]
49          neighbors.append(np.array(idx, dtype=np.int32))
50
51      with open(cache_file, "wb") as f:
52          pickle.dump(neighbors, f)
53
54      return neighbors
55
56  # =====
57  # Moran's I (sparse)
58  # =====
59
60  def morans_I_sparse(values, neighbors):
61      x = values - values.mean()
62      num = 0.0
63      W = 0
64
65      for i, nbrs in enumerate(neighbors):
66          if len(nbrs) == 0:
67              continue
68          num += x[i] * x[nbrs].sum()
69          W += len(nbrs)
70

```



```

71     den = np.sum(x * x)
72     if W == 0 or den == 0:
73         return np.nan
74
75     return (len(values) / W) * (num / den)
76
77 def permutation_null(values, neighbors, n_perm, rng):
78     null = np.empty(n_perm)
79     for i in range(n_perm):
80         perm = rng.permutation(values)
81         null[i] = morans_I_sparse(perm, neighbors)
82     return null
83
84 # =====
85 # Region filtering
86 # =====
87
88 def filter_region(df, region):
89     if region["type"] == "global":
90         return df
91
92     lat0, lon0, R = region["lat"], region["lon"], region["radius_km"]
93
94     d = np.array([
95         EARTH_RADIUS_KM * np.arccos(
96             max(-1.0, min(1.0,
97                 sin(radians(lat)) * sin(radians(lat0)) +
98                 cos(radians(lat)) * cos(radians(lat0)) *
99                 cos(radians(lon - lon0))
100             ))
101         )
102         for lat, lon in zip(df["LAT"], df["LON"])
103     ])
104
105     return df[d <= R]
106
107 # =====
108 # Main
109 # =====

```

```

110
111 def main():
112     ap = argparse.ArgumentParser()
113     ap.add_argument("--input", required=True)
114     ap.add_argument("--misfit-column", required=True)
115     ap.add_argument("--scales", required=True)
116     ap.add_argument("--permutations", type=int, default=1000)
117     ap.add_argument("--region", action="append")
118     ap.add_argument("--output", default="morans_results.csv")
119     ap.add_argument("--cache-dir", default="neighbor_cache")
120     ap.add_argument("--seed", type=int, default=42)
121     args = ap.parse_args()
122
123     os.makedirs(args.cache_dir, exist_ok=True)
124     scales = [float(s) for s in args.scales.split(",")]
125     rng = np.random.default_rng(args.seed)
126
127     df = pd.read_csv(args.input)
128
129     # -----
130     # Euler pole validation / normalization
131     # -----
132     if {"POLE_LAT", "POLE_LON"}.issubset(df.columns):
133         pole_lat_col = "POLE_LAT"
134         pole_lon_col = "POLE_LON"
135     elif {"EULER_LAT", "EULER_LON"}.issubset(df.columns):
136         pole_lat_col = "EULER_LAT"
137         pole_lon_col = "EULER_LON"
138     else:
139         raise RuntimeError(
140             "Input CSV must contain POLE_LAT/POLE_LON or EULER_LAT/EULER_LON"
141         )
142
143     if "RUN_ID" not in df.columns:
144         df["RUN_ID"] = "DEFAULT"
145
146     pole_lookup = (
147         df.groupby("RUN_ID")[[pole_lat_col, pole_lon_col]]
148         .first()

```

```

149         .rename(columns={
150             pole_lat_col: "POLE_LAT",
151             pole_lon_col: "POLE_LON"
152         })
153     )
154
155     # -----
156     # Regions
157     # -----
158     regions = []
159     if args.region:
160         for r in args.region:
161             name, rest = r.split(":")
162             lat, lon, rad = map(float, rest.split(","))
163             regions.append({
164                 "name": name,
165                 "type": "circle",
166                 "lat": lat,
167                 "lon": lon,
168                 "radius_km": rad
169             })
170     else:
171         regions.append({"name": "GLOBAL", "type": "global"})
172
173     rows = []
174     skipped_regions = set()
175
176     for run_id, df_run in df.groupby("RUN_ID"):
177         print(f"\nRUN_ID: {run_id}")
178
179         pole_lat = pole_lookup.loc[run_id, "POLE_LAT"]
180         pole_lon = pole_lookup.loc[run_id, "POLE_LON"]
181
182         for region in regions:
183             df_r = filter_region(df_run, region)
184
185             if len(df_r) < MIN_POINTS:
186                 skipped_regions.add(region["name"])
187                 continue

```

```

188
189     lat = df_r["LAT"].values
190     lon = df_r["LON"].values
191     vals = df_r[args.misfit_column].values
192
193     for L in scales:
194         cache_file = os.path.join(
195             args.cache_dir,
196             f"neighbors_{region['name']}_L{int(L)}.pkl"
197         )
198
199         neighbors = build_neighbors(lat, lon, L, cache_file)
200
201         I_obs = morans_I_sparse(vals, neighbors)
202         if not np.isfinite(I_obs):
203             skipped_regions.add(region["name"])
204             continue
205
206         null = permutation_null(vals, neighbors, args.permutations, rng)
207
208         rows.append({
209             "RUN_ID": run_id,
210             "REGION": region["name"],
211             "SCALE_KM": L,
212             "N_POINTS": len(vals),
213             "I_OBS": I_obs,
214             "I_NULL_MEAN": null.mean(),
215             "I_NULL_STD": null.std(),
216             "Z_SCORE": (I_obs - null.mean()) / null.std(),
217             "P_VALUE": (null >= I_obs).mean(),
218             "I_P05": np.percentile(null, 5),
219             "I_P50": np.percentile(null, 50),
220             "I_P95": np.percentile(null, 95),
221             "POLE_LAT": pole_lat,
222             "POLE_LON": pole_lon
223         })
224
225     if not rows:
226         raise RuntimeError("No valid Moran results were produced for any region.")

```

```

227
228     results = pd.DataFrame(rows)
229
230     if "REGION" not in results.columns:
231         raise RuntimeError(
232             "Internal error: REGION column missing from results."
233         )
234
235     results.to_csv(args.output, index=False)
236     print(f"\nSaved results → {args.output}")
237
238     rankings = (
239         results
240         .sort_values(["REGION", "SCALE_KM", "I_OBS"],
241                     ascending=[True, True, False])
242         .assign(RANK=lambda d:
243                 d.groupby(["REGION", "SCALE_KM"]).cumcount() + 1)
244     )
245
246     rank_file = args.output.replace(".csv", "_rankings.csv")
247     rankings.to_csv(rank_file, index=False)
248     print(f"Saved rankings → {rank_file}")
249
250     if skipped_regions:
251         print("\nSkipped regions due to insufficient or invalid data:")
252         for r in sorted(skipped_regions):
253             print(f"  - {r}")
254
255 if __name__ == "__main__":
256     main()

```

---

*shear<sub>g</sub>generate<sub>e</sub>nsemble.py*

---

```

1  #!/usr/bin/env python3
2  """
3  Generate an ensemble of conjugate shear stress maps from TPW-style rotations
4  and sample them against the World Stress Map (WSM).
5
6  Baseline:

```

```

7     - Rotation = 104°
8     - Axis = 31°E meridian (northward)
9
10    Randomized alternates:
11    - Random Euler poles
12    - Random rotation magnitudes
13    - Random rotation sense
14    """
15
16    import argparse
17    import numpy as np
18    import pandas as pd
19
20    EARTH_RADIUS = 6371.0
21    DEG2RAD = np.pi / 180.0
22
23    # -----
24    # Geometry utilities
25    # -----
26
27    def sph_to_cart(lat, lon):
28        lat *= DEG2RAD
29        lon *= DEG2RAD
30        return np.array([
31            np.cos(lat) * np.cos(lon),
32            np.cos(lat) * np.sin(lon),
33            np.sin(lat)
34        ])
35
36    def cart_to_sph(v):
37        x, y, z = v
38        lat = np.arcsin(z)
39        lon = np.arctan2(y, x)
40        return lat / DEG2RAD, lon / DEG2RAD
41
42    def rotate_vector(v, axis, angle_deg):
43        theta = angle_deg * DEG2RAD
44        axis = axis / np.linalg.norm(axis)
45        return (

```



```

46         v * np.cos(theta)
47         + np.cross(axis, v) * np.sin(theta)
48         + axis * np.dot(axis, v) * (1 - np.cos(theta))
49     )
50
51     # -----
52     # TPW stress model (simplified but physical)
53     # -----
54
55     def compute_shear_azimuth(lat, lon, pole_lat, pole_lon):
56         """
57         Compute conjugate shear azimuths from TPW geometry.
58         """
59         p = sph_to_cart(lat, lon)
60         pole = sph_to_cart(pole_lat, pole_lon)
61
62         # Tangential velocity direction
63         v = np.cross(pole, p)
64         if np.linalg.norm(v) == 0:
65             return np.nan, np.nan
66
67         v /= np.linalg.norm(v)
68
69         # Project to local tangent plane
70         north = np.array([0, 0, 1])
71         east = np.cross(north, p)
72         east /= np.linalg.norm(east)
73         north = np.cross(p, east)
74
75         ve = np.dot(v, east)
76         vn = np.dot(v, north)
77
78         az = (np.arctan2(ve, vn) / DEG2RAD) % 360.0
79
80         # Conjugate shears  $\pm 45^\circ$ 
81         return az, (az + 90.0) % 360.0
82
83     # -----
84     # Main

```

```

85  # -----
86
87  def main():
88      ap = argparse.ArgumentParser()
89      ap.add_argument("--wsm", required=True, help="WSM CSV")
90      ap.add_argument("--output", default="shear_ensemble.csv")
91      ap.add_argument("--random", type=int, default=0,
92                      help="Number of randomized TPW realizations")
93      ap.add_argument("--rot-min", type=float, default=30)
94      ap.add_argument("--rot-max", type=float, default=150)
95      ap.add_argument("--seed", type=int, default=42)
96      args = ap.parse_args()
97
98      rng = np.random.default_rng(args.seed)
99      wsm = pd.read_csv(args.wsm)
100
101      results = []
102
103      # -----
104      # Define ensemble
105      # -----
106
107      ensemble = []
108
109      # Baseline TPW (104° along 31°E)
110      ensemble.append({
111          "run_id": "TPW_BASELINE",
112          "pole_lat": 0.0,
113          "pole_lon": 31.0,
114          "rot_deg": 104.0,
115          "rot_sign": +1
116      })
117
118      # Randomized alternatives
119      for i in range(args.random):
120          u = rng.uniform(-1, 1)
121          pole_lat = np.arcsin(u) / DEG2RAD
122          pole_lon = rng.uniform(0, 360)
123          rot_deg = rng.uniform(args.rot_min, args.rot_max)

```

```

124     rot_sign = rng.choice([-1, +1])
125
126     ensemble.append({
127         "run_id": f"TPW_RANDOM_{i:03d}",
128         "pole_lat": pole_lat,
129         "pole_lon": pole_lon,
130         "rot_deg": rot_deg,
131         "rot_sign": rot_sign
132     })
133
134     # -----
135     # Compute stress for each realization
136     # -----
137
138     for cfg in ensemble:
139         print(f"Generating {cfg['run_id']}")
140
141         pole = sph_to_cart(cfg["pole_lat"], cfg["pole_lon"])
142         angle = cfg["rot_sign"] * cfg["rot_deg"]
143
144         for _, row in wsm.iterrows():
145             lat, lon = row["LAT"], row["LON"]
146             wsm_az = row["AZI"] % 360.0
147
148             az1, az2 = compute_shear_azimuth(lat, lon,
149                                             cfg["pole_lat"],
150                                             cfg["pole_lon"])
151
152             if np.isnan(az1):
153                 continue
154
155             mis1 = abs((az1 - wsm_az + 90) % 180 - 90)
156             mis2 = abs((az2 - wsm_az + 90) % 180 - 90)
157
158             results.append({
159                 "RUN_ID": cfg["run_id"],
160                 "POLE_LAT": cfg["pole_lat"],
161                 "POLE_LON": cfg["pole_lon"],
162                 "ROT_DEG": cfg["rot_deg"],
163                 "ROT_SIGN": cfg["rot_sign"],

```

```

163         "LAT": lat,
164         "LON": lon,
165         "WSM_AZ": wsm_az,
166         "NET1_AZ": az1,
167         "NET2_AZ": az2,
168         "NET1_MISFIT": mis1,
169         "NET2_MISFIT": mis2,
170         "BEST_MISFIT": min(mis1, mis2),
171         "QUALITY": row.get("QUALITY", None),
172         "PLATE": row.get("PLATE", None)
173     })
174
175     out = pd.DataFrame(results)
176     out.to_csv(args.output, index=False)
177     print(f"Saved {args.output}")
178
179     # -----
180     if __name__ == "__main__":
181         main()

```

---

## rank-plot.py

---

```

1  #!/usr/bin/env python3
2  import argparse
3  import pandas as pd
4  import numpy as np
5  import matplotlib.pyplot as plt
6  from math import radians, sin, cos, acos
7
8
9  # =====
10 # Geometry utilities
11 # =====
12
13 def angular_distance_deg(lat1, lon1, lat2, lon2):
14     """Great-circle angular distance in degrees."""
15     lat1, lon1, lat2, lon2 = map(radians, [lat1, lon1, lat2, lon2])
16     dot = (
17         sin(lat1) * sin(lat2)

```

```

18         + cos(lat1) * cos(lat2) * cos(lon1 - lon2)
19     )
20     dot = max(-1.0, min(1.0, dot))
21     return np.degrees(acos(dot))
22
23
24 def euler_polar_coords(lat, lon, lat0, lon0):
25     """
26     Convert Euler pole (lat,lon) into polar coordinates
27     relative to baseline pole (lat0,lon0).
28     """
29     d = angular_distance_deg(lat, lon, lat0, lon0)
30     theta = np.radians(lon)
31     r = np.radians(d)
32     return theta, np.degrees(r)
33
34
35 # =====
36 # Shared plotting routine
37 # =====
38
39 def make_plots(df, baseline_id, b_lat, b_lon, output_prefix):
40     # =====
41     # Plot 1: Rank vs Euler distance (faceted by scale)
42     # =====
43
44     scales = sorted(df["SCALE_KM"].unique())
45     fig, axes = plt.subplots(
46         1, len(scales),
47         figsize=(6 * len(scales), 5),
48         sharey=True
49     )
50
51     if len(scales) == 1:
52         axes = [axes]
53
54     for ax, L in zip(axes, scales):
55         d = df[df["SCALE_KM"] == L]
56         rand = d[d["RUN_ID"] != baseline_id]

```

```

57     base = d[d["RUN_ID"] == baseline_id]
58
59     ax.scatter(
60         rand["EULER_DIST_DEG"], rand["RANK"],
61         s=12, alpha=0.6, label="Random"
62     )
63
64     if not base.empty:
65         ax.scatter(
66             base["EULER_DIST_DEG"], base["RANK"],
67             s=50, c="red", label="Baseline"
68         )
69
70     ax.set_title(f"Scale = {int(L)} km")
71     ax.set_xlabel("Euler distance to baseline (deg)")
72     ax.set_ylabel("Rank")
73     ax.invert_yaxis()
74     ax.grid(True, alpha=0.3)
75
76 plt.tight_layout()
77 plt.savefig(f"{output_prefix}_rank_vs_euler.png", dpi=200)
78 plt.close()
79
80 # =====
81 # Plot 2: Rank vs wavelength
82 # =====
83
84 fig, ax = plt.subplots(figsize=(7, 5))
85
86 for run_id, g in df.groupby("RUN_ID"):
87     if run_id == baseline_id:
88         ax.plot(
89             g["SCALE_KM"], g["RANK"],
90             linewidth=2.5, label="Baseline"
91         )
92     else:
93         ax.plot(
94             g["SCALE_KM"], g["RANK"],
95             color="gray", alpha=0.3

```

```

96         )
97
98     ax.set_xlabel("Wavelength (km)")
99     ax.set_ylabel("Rank")
100    ax.set_xscale("log")
101    ax.invert_yaxis()
102    ax.grid(True, alpha=0.3)
103    ax.legend()
104
105    plt.tight_layout()
106    plt.savefig(f"{output_prefix}_rank_vs_scale.png", dpi=200)
107    plt.close()
108
109    # =====
110    # Plot 3: Polar Euler-space visualization
111    # =====
112
113    fig = plt.figure(figsize=(7, 7))
114    ax = plt.subplot(111, polar=True)
115
116    for run_id, g in df.groupby("RUN_ID"):
117        theta, r = zip(*[
118            euler_polar_coords(
119                row["POLE_LAT"], row["POLE_LON"],
120                b_lat, b_lon
121            )
122            for _, row in g.iterrows()
123        ])
124        ax.plot(theta, r, alpha=0.5)
125
126    ax.set_title("Euler-space scatter (baseline at origin)")
127    ax.set_rlabel_position(225)
128    ax.grid(True)
129
130    plt.tight_layout()
131    plt.savefig(f"{output_prefix}_euler_polar.png", dpi=200)
132    plt.close()
133
134    print("Saved plots:")

```



```

135     print(f" {output_prefix}_rank_vs_euler.png")
136     print(f" {output_prefix}_rank_vs_scale.png")
137     print(f" {output_prefix}_euler_polar.png")
138
139
140     # =====
141     # Main
142     # =====
143
144     def main():
145         ap = argparse.ArgumentParser()
146         ap.add_argument("--input", required=True, help="Rankings CSV")
147         ap.add_argument("--baseline", default="TPW_BASELINE")
148         ap.add_argument("--region", default="Arctic")
149         ap.add_argument("--output-prefix", default="morans_rank")
150         ap.add_argument(
151             "--all-regions-mean",
152             action="store_true",
153             help="Also generate plots for the mean across all regions combined"
154         )
155         args = ap.parse_args()
156
157         df = pd.read_csv(args.input)
158
159         # -----
160         # Euler pole metadata
161         # -----
162         if not {"POLE_LAT", "POLE_LON"}.issubset(df.columns):
163             raise RuntimeError(
164                 "CSV must include POLE_LAT and POLE_LON for Euler-space plotting"
165             )
166
167         # Baseline pole
168         b = df[df["RUN_ID"] == args.baseline].iloc[0]
169         b_lat, b_lon = b["POLE_LAT"], b["POLE_LON"]
170
171         # Euler angular distance (degrees)
172         df["EULER_DIST_DEG"] = df.apply(
173             lambda r: angular_distance_deg(

```

```

174         r["POLE_LAT"], r["POLE_LON"], b_lat, b_lon
175     ),
176     axis=1
177 )
178
179     # Preserve full dataset for optional averaging
180     df_full = df.copy()
181
182     # =====
183     # Region-specific plots (existing behavior)
184     # =====
185     df_region = df[df["REGION"] == args.region]
186     if df_region.empty:
187         raise RuntimeError(
188             f"No valid Moran results available for region '{args.region}'."
189         )
190
191     make_plots(
192         df_region,
193         baseline_id=args.baseline,
194         b_lat=b_lat,
195         b_lon=b_lon,
196         output_prefix=args.output_prefix
197     )
198
199     # =====
200     # Optional: averaged results across ALL regions
201     # =====
202     if args.all_regions_mean:
203         df_mean = (
204             df_full.groupby(["RUN_ID", "SCALE_KM"], as_index=False)
205             .agg({
206                 "RANK": "mean",
207                 "EULER_DIST_DEG": "mean",
208                 "POLE_LAT": "mean",
209                 "POLE_LON": "mean"
210             })
211         )
212         df_mean["REGION"] = "ALL_MEAN"

```

```

213
214         make_plots(
215             df_mean,
216             baseline_id=args.baseline,
217             b_lat=b_lat,
218             b_lon=b_lon,
219             output_prefix=f"{args.output_prefix}_ALLMEAN"
220         )
221
222
223 if __name__ == "__main__":
224     main()

```

---

## coherence.py

---

```

1  #!/usr/bin/env python3
2  import argparse
3  import numpy as np
4  import pandas as pd
5  from scipy.signal import savgol_filter
6
7  MIN_POINTS = 3 # require 3 wavelength scales
8
9
10 def curvature_metrics(L, I):
11     """Compute slope, curvature, monotonicity, plateau index, inflections."""
12     L = np.asarray(L, float)
13     I = np.asarray(I, float)
14
15     # normalize wavelength spacing
16     x = (L - L.min()) / (L.max() - L.min() + 1e-12)
17
18     # smoothing only when enough points exist
19     if len(I) >= 5:
20         I_sm = savgol_filter(I, window_length=5 if len(I) >= 5 else len(I)|1,
21                               polyorder=2, mode="interp")
22     else:
23         I_sm = I.copy()
24

```

```

25     d1 = np.gradient(I_sm, x, edge_order=1)
26     d2 = np.gradient(d1, x, edge_order=1)
27
28     slope_mean = np.nanmean(d1)
29     slope_var = np.nanvar(d1)
30
31     curvature_mean = np.nanmean(d2)
32     curvature_std = np.nanstd(d2)
33
34     # monotonicity: sign consistency in first derivative
35     sign_changes = np.sum(np.sign(d1[1:]) != np.sign(d1[:-1]))
36     monotonicity = 1.0 - sign_changes / max(len(d1) - 1, 1)
37
38     # plateau index: fraction where |slope| < 0
39     plateau = np.mean(np.abs(d1) < np.percentile(np.abs(d1), 25))
40
41     # inflections = zero crossings of curvature
42     infl = np.sum(np.sign(d2[1:]) != np.sign(d2[:-1]))
43
44     return dict(
45         SLOPE_MEAN=slope_mean,
46         SLOPE_VAR=slope_var,
47         CURVATURE_MEAN=curvature_mean,
48         CURVATURE_STD=curvature_std,
49         MONOTONICITY=monotonicity,
50         PLATEAU_INDEX=plateau,
51         INFLECTIONS=infl,
52         I_RANGE=float(np.nanmax(I) - np.nanmin(I)),
53     )
54
55
56 def compute_descriptors(df, out_path):
57
58     rows = []
59     grouped = df.groupby(["REGION", "RUN_ID"], dropna=False)
60
61     for (region, run_id), g in grouped:
62
63         g = g.sort_values("SCALE_KM")

```

```

64     L = g["SCALE_KM"].values
65     I = g["I_OBS"].values
66     Z = g["Z_SCORE"].values
67
68     role = "BASELINE" if run_id == "TPW_BASELINE" else "PEER"
69
70     if len(L) < MIN_POINTS or np.all(np.isnan(I)):
71         rows.append(dict(
72             REGION=region, RUN_ID=run_id, ROLE=role,
73             STATUS="INSUFFICIENT_POINTS"
74         ))
75         continue
76
77     m = curvature_metrics(L, I)
78     rows.append(dict(
79         REGION=region,
80         RUN_ID=run_id,
81         ROLE=role,
82         STATUS="OK",
83         N_SCALES=len(L),
84         **m,
85         I_MEAN=float(np.nanmean(I)),
86         Z_MEAN=float(np.nanmean(Z)),
87     ))
88
89     desc = pd.DataFrame(rows)
90
91     # ---- Baseline vs Ensemble Coherence ----
92     summaries = []
93     for region, g in desc.groupby("REGION"):
94         base = g[g["ROLE"] == "BASELINE"]
95         peers = g[g["ROLE"] == "PEER"]
96
97         if base.empty or peers.empty:
98             continue
99
100         b = base.iloc[0]
101         diffs = peers.copy()
102

```

```

103     for col in [
104         "SLOPE_MEAN", "CURVATURE_STD", "MONOTONICITY",
105         "PLATEAU_INDEX", "INFLECTIONS", "I_RANGE"
106     ]:
107         diffs[f"DELTA_{col}"] = peers[col] - b[col]
108
109     summaries.append(dict(
110         REGION=region,
111         N_PEERS=len(peers),
112         BASE_SLOPE_MEAN=b["SLOPE_MEAN"],
113         ENSEMBLE_SLOPE_MEAN=float(peers["SLOPE_MEAN"].mean()),
114         DELTA_SLOPE_MEAN=float(diffs["DELTA_SLOPE_MEAN"].mean()),
115
116         BASE_CURVATURE_STD=b["CURVATURE_STD"],
117         ENSEMBLE_CURVATURE_STD=float(peers["CURVATURE_STD"].mean()),
118         DELTA_CURVATURE_STD=float(diffs["DELTA_CURVATURE_STD"].mean()),
119
120         BASE_MONOTONICITY=b["MONOTONICITY"],
121         ENSEMBLE_MONOTONICITY=float(peers["MONOTONICITY"].mean()),
122         DELTA_MONOTONICITY=float(diffs["DELTA_MONOTONICITY"].mean()),
123
124         BASE_PLATEAU_INDEX=b["PLATEAU_INDEX"],
125         ENSEMBLE_PLATEAU_INDEX=float(peers["PLATEAU_INDEX"].mean()),
126         DELTA_PLATEAU_INDEX=float(diffs["DELTA_PLATEAU_INDEX"].mean()),
127     ))
128
129     summary = pd.DataFrame(summaries)
130
131     desc.to_csv(out_path, index=False)
132     summary.to_csv(out_path.replace(".csv", "_summary.csv"), index=False)
133
134     print(f"Saved descriptors → {out_path}")
135     print(f"Saved ensemble summary → {out_path.replace('.csv', '_summary.csv')}")
136
137
138 def main():
139     ap = argparse.ArgumentParser()
140     ap.add_argument("--input", required=True)
141     ap.add_argument("--output", default="coherence_shape_descriptors.csv")

```

```

142     args = ap.parse_args()
143
144     df = pd.read_csv(args.input)
145     required = {
146         "RUN_ID", "REGION", "SCALE_KM", "I_OBS", "Z_SCORE"
147     }
148     missing = required - set(df.columns)
149     if missing:
150         raise RuntimeError(f"Missing columns: {missing}")
151
152     compute_descriptors(df, args.output)
153
154
155 if __name__ == "__main__":
156     main()

```

---

#### coherence<sub>vs</sub> Moran.py

---

```

1  #!/usr/bin/env python3
2  import argparse
3  import os
4  import numpy as np
5  import pandas as pd
6  import matplotlib.pyplot as plt
7
8
9  # -----
10 # Robust finite-difference slope estimator (dI / d log L)
11 # -----
12 def finite_difference_slopes(L, I):
13     """
14     Compute dI/d(log L) with numerical stability.
15     Handles duplicate scales, missing values, and sparse scale sets.
16     Returns one slope per scale value.
17     """
18     L = np.asarray(L, dtype=float)
19     I = np.asarray(I, dtype=float)
20
21     logL = np.log(L)

```



```

22     slopes = np.full_like(I, np.nan)
23
24     n = len(L)
25     if n < 2:
26         return slopes
27
28     for i in range(n):
29         il = i - 1 if i > 0 else None
30         ir = i + 1 if i < n - 1 else None
31
32         # central difference (preferred)
33         if il is not None and ir is not None:
34             dlog = logL[ir] - logL[il]
35             if dlog != 0:
36                 slopes[i] = (I[ir] - I[il]) / dlog
37                 continue
38
39         # forward fallback
40         if ir is not None:
41             dlog = logL[ir] - logL[i]
42             if dlog != 0:
43                 slopes[i] = (I[ir] - I[i]) / dlog
44                 continue
45
46         # backward fallback
47         if il is not None:
48             dlog = logL[i] - logL[il]
49             if dlog != 0:
50                 slopes[i] = (I[i] - I[il]) / dlog
51                 continue
52
53     return slopes
54
55
56 # -----
57 # Load and merge coherence + Moran's outputs
58 # -----
59 def load_data(coherence_path, morans_path):
60     coh = pd.read_csv(coherence_path)

```

```

61     mor = pd.read_csv(morans_path)
62
63     mor = mor.copy()
64     mor["I_EXCESS_MEAN"] = mor["I_OBS"] - mor["I_NULL_MEAN"]
65
66     df = pd.merge(
67         coh,
68         mor[
69             [
70                 "RUN_ID",
71                 "REGION",
72                 "SCALE_KM",
73                 "I_OBS",
74                 "I_NULL_MEAN",
75                 "I_EXCESS_MEAN",
76             ]
77         ],
78         on=["RUN_ID", "REGION"],
79         how="inner",
80     )
81
82     return df
83
84
85     # -----
86     # Global scatter / baseline highlighted
87     # -----
88     def plot_global(df, outdir):
89         fig, ax = plt.subplots(figsize=(10, 6))
90
91         peers = df[df["ROLE"] != "BASELINE"]
92         base = df[df["ROLE"] == "BASELINE"]
93
94         ax.scatter(
95             peers["SLOPE_MEAN"],
96             peers["I_EXCESS_MEAN"],
97             c="0.5",
98             marker="x",
99             alpha=1.0,

```

```

100         s=26,
101         label="NULL",
102         zorder=1,
103     )
104
105     ax.scatter(
106         base["SLOPE_MEAN"],
107         base["I_EXCESS_MEAN"],
108         c="red",
109         s=50,
110         zorder=4,
111         label="BASELINE",
112     )
113
114     ax.axhline(0, color="black", lw=0.8)
115     ax.set_title("Global coherence vs spatial clustering strength (per-scale)")
116     ax.set_xlabel("Coherence (finite-difference slope  $dI / d \log L$ )")
117     ax.set_ylabel("Moran's I excess vs null ( $I_{\text{obs}} - I_{\text{null\_mean}}$ )")
118     ax.legend(frameon=False)
119
120     fig.tight_layout()
121     fig.savefig(f"{outdir}/global_coherence_vs_I.png", dpi=220)
122     plt.close(fig)
123
124
125     # -----
126     # Combined mean baseline trajectory (BLUE LINE)
127     # -----
128     def plot_combined_mean(df, outdir):
129         base = df[df["ROLE"] == "BASELINE"].copy()
130
131         mean_curve = (
132             base.groupby("SCALE_KM", as_index=False)[["I_OBS", "I_EXCESS_MEAN"]]
133             .mean()
134             .sort_values("SCALE_KM")
135         )
136
137         mean_curve["COHERENCE_SLOPE"] = finite_difference_slopes(
138             mean_curve["SCALE_KM"].values,

```

```

139         mean_curve["I_OBS"].values,
140     )
141
142     fig, ax = plt.subplots(figsize=(10, 6))
143
144     ax.plot(
145         mean_curve["COHERENCE_SLOPE"],
146         mean_curve["I_EXCESS_MEAN"],
147         "-o",
148         color="blue",
149         lw=2.2,
150         ms=6,
151         zorder=4,
152         label="Combined Mean (Baseline)",
153     )
154
155     for _, r in mean_curve.iterrows():
156         ax.text(
157             r["COHERENCE_SLOPE"],
158             r["I_EXCESS_MEAN"],
159             f"{int(r['SCALE_KM'])} km",
160             fontsize=9,
161             color="blue",
162             ha="left",
163             va="bottom",
164         )
165
166     ax.axhline(0, color="black", lw=0.8)
167     ax.set_title("Combined mean coherence vs Moran's I (baseline only)")
168     ax.set_xlabel("Coherence (finite-difference slope  $dI / d \log L$ )")
169     ax.set_ylabel("Moran's I excess vs null")
170
171     ax.legend(frameon=False)
172     fig.tight_layout()
173     fig.savefig(f"{outdir}/combined_mean_coherence_vs_I.png", dpi=220)
174     plt.close(fig)
175
176
177 # -----

```

```

178 # Regional plot / baseline trajectory vs null ensemble
179 # -----
180 def plot_region(df_region, outdir):
181     region = df_region["REGION"].iloc[0]
182
183     baseline = (
184         df_region[df_region["ROLE"] == "BASELINE"]
185         .sort_values("SCALE_KM")
186         .copy()
187     )
188     peers = df_region[df_region["ROLE"] != "BASELINE"]
189
190     slopes = finite_difference_slopes(
191         baseline["SCALE_KM"].values,
192         baseline["I_OBS"].values,
193     )
194     baseline["COHERENCE_SLOPE"] = slopes
195
196     fig, ax = plt.subplots(figsize=(10, 6))
197
198     ax.scatter(
199         peers["SLOPE_MEAN"],
200         peers["I_EXCESS_MEAN"],
201         s=26,
202         c="0.5",
203         marker="x",
204         alpha=1.0,
205         label="NULL",
206         zorder=1,
207     )
208
209     ax.plot(
210         baseline["COHERENCE_SLOPE"],
211         baseline["I_EXCESS_MEAN"],
212         "-o",
213         color="red",
214         lw=2.0,
215         ms=6,
216         zorder=4,

```

```

217         label="BASELINE",
218     )
219
220     for _, r in baseline.iterrows():
221         ax.text(
222             r["COHERENCE_SLOPE"],
223             r["I_EXCESS_MEAN"],
224             f"{int(r['SCALE_KM'])} km",
225             fontsize=9,
226             color="red",
227             ha="left",
228             va="bottom",
229         )
230
231     ax.axhline(0, color="black", lw=0.8)
232     ax.set_title(f"{region}: Coherence vs Moran's I (per-scale)")
233     ax.set_xlabel("Coherence (finite-difference slope  $dI / d \log L$ )")
234     ax.set_ylabel("Moran's I excess vs null")
235
236     ax.legend(frameon=False)
237     fig.tight_layout()
238     fig.savefig(f"{outdir}/{region}_coherence_vs_I.png", dpi=220)
239     plt.close(fig)
240
241
242     # -----
243     # Main
244     # -----
245     def main():
246         parser = argparse.ArgumentParser(
247             description="Compare coherence descriptors vs Moran's I clustering strength"
248         )
249         parser.add_argument("--coherence", required=True)
250         parser.add_argument("--morans", required=True)
251         parser.add_argument("--output", required=True)
252
253         args = parser.parse_args()
254         os.makedirs(args.output, exist_ok=True)
255

```

```

256     df = load_data(args.coherence, args.morans)
257
258     print("\nDetected role distribution:\n", df["ROLE"].value_counts(), "\n")
259
260     plot_global(df, args.output)
261     plot_combined_mean(df, args.output)
262
263     for _, sub in df.groupby("REGION"):
264         plot_region(sub, args.output)
265
266     print(f"\nPlots written to {os.path.abspath(args.output)}")
267
268
269 if __name__ == "__main__":
270     main()

```

---